Fatigue Properties of Shape Memory Alloys with Regard to Their Use in Medicine

Michal Ackermann

July 2015

The dissertation is submitted to the
TECHNICAL UNIVERSITY OF LIBEREC
For the degree Doctor of Philosophy

Declaration

I hereby certify that I have been informed the Act 121/2000, the Copyright Act of the Czech Republic, namely §60-Schoolwork, applies to my Ph.D. thesis in full scope. I acknowledge that the Technical University of Liberec (TUL) does not infringe my copyrights by using my thesis for TUL's internal purposes. I am aware of my obligation to inform TUL on having used or licensed to use my thesis; in such a case TUL may require compensation of costs spent on creating the work at up to their actual amount. I have written the thesis myself using literature listed therein and consulting it with my thesis supervisor and tutor. Concurrently I confirm that the printed version of my thesis is coincident with an electronic version, inserted into the IS/STAG.

Date:

Seignature:

Fatigue Properties of Shape Memory Alloys with Regard to Their Use in Medicine

by

Michal Ackermann

Supervisor: doc. Ing. **Lukáš Čapek**, Ph.D., Technical University of Liberec, Liberec

Abstract:

This work deals with characterization of Nickel-Titanium shape memory alloy which is used for production of cardiovascular stents. Material tests such as Differential Scanning Calorimetry and tensile tests carried out under different values of temperature allowed for precise description of material's pseudoelastic effect. Moreover, fatigue tests of the alloy were done under two different values of temperature and its corresponding S-N curves were constructed.

On the basis of experimental data, full range of loads which are imposed on stent during its life are studied using finite element method. In this part, loading a stent into catheter and its subsequent deployment in blood vessel was simulated. Following simulation of pressure pulse offered data about cyclic loading to which the stent is exposed when implanted into an artery. Thanks to previous simulation and known S-N curve of the material, durability analysis of the stent was done with use of nominal stress approach.

In last part of the work, a device dedicated to cyclic testing of the whole stent-graft structure is constructed. Concept of the machine, together with corresponding calculations are shown. Outcome of this work is a fully operational machine at which eight stent-grafts can be tested at the same time. Pressure characteristics which acts inside mock arteries was experimentally verified to be similar to conditions in human body.

Keywords:

Shape memory alloys, Fatigue, Biomechanics, FEM, NiTi, Stent

Únavové vlastnosti slitin s tvarovou pamětí s ohledem na jejich využití v medicíně

napsal

Michal Ackermann

Školitel: doc. Ing. **Lukáš Čapek**, Ph.D., Technická univerzita v Liberci, Liberec

Abstrakt:

Tato práce se zabývá slitinou Nikl-Titan, která patří do skupiny materiálů s tvarovou pamětí a která se využívá k výrobě kardiovaskulárních stentů. Pro přesné určení pseudoelastického efektu dané slitiny byly provedeny různé materiálové testy, jako například diferenční scanovací kalorimetrie a tahové zkoušky materiálu, prováděné za různé teploty okolního prostředí. Dalším významným bodem této části byly únavové testy dané slitiny za dvou teplot okolního prostředí a následná konstrukce odpovídajících S-N křivek materiálu.

Na základě experimentálních dat byly poté zkoumány účinky různých zátěžných stavů, kterým je stent vystaven během implantace a jeho následné funkce. Tyto úlohy jsou řešeny za pomoci metody konečných prvků. Konkrétně je v této části řešeno zmáčknutí stentu do katetru a jeho následná expanze v tepně. Dále se simulace zabývají odvozením průběhu napětí ve stentu během systolického/diastolického tlakového pulzu. Na základě těchto dat a díky znalosti S-N křivek je poté provedena analýza životnosti stentu pomocí metody nominálních napětí.

Poslední část disertace se zabývá konstrukcí zařízení, které slouží k testování celé struktury stent-graftu. V práci je zmíněna koncepce zařízení a dále jsou uvedeny odpovídající výpočty vedoucí k odvození jeho potřebných součástí. Výsledkem je zařízení, na kterém je možné najednou testovat až osm vzorků. Po dokončení zařízení byl experimentálně ověřen průběh tlaku v modelech tepen.

Klíčová slova:

Slitiny s tvarovou pamětí, Únava materiálu, Biomechanika, MKP, NiTi, Stent

Acknowledgement

At this point, I would like express my gratitude to all the people who contributed to formation of my thesis. First of all, I would like to thank my tutor, doc. Ing. Lukáš Čapek, Ph.D. for his patient and kind supervising and for all the helpful advices he gave me throughout my doctoral study. I would also like to thank ELLA-CS company for providing material for testing purposes and for arranging valuable consultations with Tomáš Panchártek who is responsible person for stent-graft development. My thanks also belongs to the Ministry of Industry and Trade of the Czech Republic which financially supported major part of the work (grant no. FR – TI1/584). Concerning the practical part of the thesis, I would like to thank to my two good colleagues and friends, Ing. Petr Henyš for helping me with finite element method simulations and with measurements and Ing. Jan Škoda for helping me with development of stent-graft cyclic testing machine.

My thanks also go to my family - without their support and understanding, this work would never be crated.

Poděkování

Na tomto místě bych rád poděkoval všem, kteří se podíleli na vzniku mé disertační práce. V první řadě bych rád poděkoval mému vedoucímu, doc. Ing. Lukáši Čapkovi, Ph.D. za jeho trpělivé a laskavé vedení a za všechny rady, které mi během mého doktorského studia předal. Rád bych také poděkoval společnosti ELLA-CS za zajištění materiálu pro testování a za organizaci konzultací s panem Tomášem Panchártkem, který je ve společnosti zodpovědný za vývoj stent-graftů. Mé díky patří také Ministertvu průmyslu a obchodu České republiky, které financovalo převážnou část mé práce (grant č. FR – TI1/584). Ohledně praktické části mé práce bych rád poděkoval dvěma dobrým kolegům a kamarádům, Ing. Petru Henyšovi za pomoc se simulacemi metodou konečných prvků a s měřeními a Ing. Janu Škodovi za pomoc při vývoji přístroje pro cyklické testy stent-graftů.

Moje díky patří také mojí rodině - bez jejich podpory a pochopení by tato práce nemohla vzniknout.

Contents

List of Figures

Nomenclature

List of Symbols

Symbol	Description
M_s	Martensite start temperature
M_f	Martensite finish temperature
A_s	Austenite start temperature
A_f	Austenite finish temperature
σ^{Ms}	Martensite start stress level
σ^{Mf}	Martensite finish stress level
σ^{As}	Austenite start stress level
σ^{Af}	Austenite finish stress level
ξ_s	Volume fraction of martensite
$\mathbf{F}$	Deformation gradient
$\mathbf{F}^e$	Elastic part of $\mathbf{F}$
$\mathbf{F}^{tr}$	Phase transformation part of $\mathbf{F}$
F	Drucker-Prager type yielding criterion
$\boldsymbol{\tau}$	Kirchhoff stress
$\mathbf{t}$	Deviatoric part of $\boldsymbol{\tau}$
α	Auricchio model material parameter
p	Pressure
R_f^{AS}	Forward transformation parameter
R_f^{SA}	Backward transformation parameter
H^{AS}, H^{SA}	Phase transformation activation conditions
$\Delta\boldsymbol{\varepsilon}$	Overall incremental strain
$\Delta\boldsymbol{\varepsilon}^{El}$	Incremental elastic strain
$\Delta\boldsymbol{\varepsilon}^{Th}$	Incremental thermal strain
$\Delta\boldsymbol{\varepsilon}^{Pl}$	Incremental plastic strain
$\Delta\boldsymbol{\varepsilon}^{Ph}$	Incremental phase transformation strain
$\mathbf{L}$	Set of elastic moduli
$\boldsymbol{\sigma}$	Incremental Cauchy stress rate
α_V	Coefficient of thermal expansion
ΔT	Temperature change
$\mathbf{I}$	Identity tensor

Symbol	Description
$\Delta\lambda$	Plastic multiplier
$\boldsymbol{\sigma'}$	Deviatoric stress
σ_{eq}	Equivalent Von Mises Stress
$\Delta\boldsymbol{\varepsilon}^{Trip}$	Oriented martensite strain contribution
$\Delta\boldsymbol{\varepsilon}^{Twin}$	Twinned martensite strain contribution
Δf^M	Rate of martesite formation
Δf^A	Rate of austenite formation
$g(\sigma_{eq})$	Saeedvafa model g-function
ε_{eq}^T	Deviatoric transformation strain
ε_v^T	Volumetric transformation strain
σ_{eff}^g	Detwinning stress
g_0	Saeedvafa model constant
R	Stress ratio
σ_{min}	Minimum stress of a cycle
σ_{max}	Maximum stress of a cycle
σ_m	Mean stress of a cycle
σ_a	Amplitude of a cycle
σ_c	Fatigue limit of the material
R_e	Yield stress of the material
w	Basquin's power law exponent
N	Number of cycles
N_f	Number of reversals
σ'_f	Fatigue strength coefficient
b	Fatigue strength exponent
ε_a	Total strain amplitude
ε_{ap}	Plastic strain amplitude
ε_{ae}	Elastic strain amplitude
ε'_f	Fatigue ductility coefficient
E	Young's modulus of elasticity
D	Damage

List of abbreviations

Abbreviation	Description
SMA	Shape memory alloy
SME	Shape memory effect
AAA	Abdominal aortic aneurysm
EVAR	Endovascular repair
NSA	Nominal stress approach
DSC	Digital scanning calorimetry
FEM	Finite element method
SEM	Scanning electron microscope

Chapter 1

Introduction

It has always been a challenge for mankind to push forward the boundaries of structural materials. This ultimate need goes hand in hand with a higher demand on material properties in a certain application. Nowadays, we are able to manufacture such a compound which is able to mill diamonds. There are materials which are able to withstand enormous temperatures such as those used to protect spacecraft when passing through Earth's atmosphere. The list could go on and on with examples of various extreme conditions which today's materials are able to resist. But, frankly, it would exceed the purpose of this introduction. What I wanted to say is that not only does each finding in the field of material science open new possibilities but it also helps to increase our life standard.

I believe that on the top of this development is, at the present time, the group called "smart materials". This category of materials exhibits unique properties even in normal conditions. But what is more, their behaviour can be significantly influenced by various types of external fields such as thermal, stress or electric and magnetic field. According to the literature, the four most recognized groups of smart materials are [1]:

- Piezoelectric
- Magnetostrictive
- Electrostrictive
- Shape memory alloys

During my work, I dealt heavily with a metal which belongs to the latter group of smart materials, i.e. the binary NiTi alloy. This material can be, without any exaggeration, also marked as the brightest representative of shape memory alloys (SMAs). NiTi's unique behaviour lies in reversible martensitic transformation which can be induced in two ways: either by applying a mechanical stress or by heating/cooling the material. On the basis of these mechanisms, two major material properties can be observed. Firstly, superelasticity in

the case of mechanically induced martensitic transformation and shape memory effect in the other case. Nevertheless, these mechanisms will be explained more in detail in Chapter 3. Another important property of NiTi has to be also mentioned at this place: the excellent biocompatibility which predestines its use in medicine [2].

1.1 Motivation

The theme and goals of my thesis emerged from a project, supported by the Ministry of Industry and Trade of the Czech Republic, grant no. FR – TI1/584, which was dealt on our university in cooperation with the ELLA-CS Company from Hradec Králové. The company is a Czech leading producer of stent-grafts, biomedical components which serve to heal several types of arterial and digestive system diseases.

Generally, the whole project had a purpose to evolve a new type of stent-graft together with an effective deployment system. Team of ELLA-CS developers were very interested in implementing NiTi shape memory alloy into their products instead of traditionally used surgical steel. The reason for the interest was simple: stent-graft has to be deployed to a damaged place via catheter. Obviously, the smaller the diameter of catheter is, the better it is for surgeon to operate it and to navigate it through a complex system of blood vessels. This advantage is especially valuable in the case of abdominal aortic aneurysm endovascular repair which will be discussed in Chapter 2.

Thanks to its high reversible deformations, stents made of NiTi alloy are capable of squeezing into a smaller diameter of catheter in comparison with those made of surgical steel. Moreover, NiTi stents are self-expandable, i.e. they completely restore their predefined shape after the implantation. After the stent-graft is deployed into the blood vessel, it is subjected not only to a highly corrosive environment but also to fatigue due to periodical change of systolic and diastolic blood pressure. At the beginning of the project, little was known about fatigue properties of the given NiTi alloy. This obstruction of effective and reliable use of the alloy as a material for stents needed to be resolved.

1.2 Goals of the thesis

During the first year of the project and after numerous consultations with developers from ELLA-CS company, the structure and goals for my thesis were set to following seven chapters:

Chapter 2, 3 and 4: State-of-the-Art in topics:

- Anatomical background of the problem
- NiTi Alloy
- Basics of fatigue analysis

Chapter 5: Material tests of given NiTi Alloy

This chapter deals with evaluation of alloy's behaviour under various conditions. Apart from its main objective, fatigue properties, this chapter has also its significance for obtaining FEM material model constants.

Chapter 6: FEM analysis

In this part, various load cases which influence a stent during its implantation and following function are studied with aid of finite element method. This part also contains verification of a chosen material model and numerical fatigue analysis.

Chapter 7: Experimental life tests of a stent-graft

ELLA-CS had a specific demand to test their stent-grafts as a whole in similar conditions to which their stents are subjected in an artery. Design of a machine and testing methodology, especially dedicated for the purpose are depicted in this chapter.

Chapter 2

Anatomical background

Due to the fact that the field of biomechanics belongs to interdisciplinary branch of science there is a need to understand the anatomical terminology which is used in following chapters. The aim of this chapter is to provide basic information about the aorta and its parts. In order to perform durability analysis of a stent-graft in Chapter 6, the knowledge of loading history, i.e. blood pressure alteration in aorta, is also crucial. The last part of the chapter is dedicated to description of the abdominal aortic aneurysm (AAA) which is one of the most common diseases of aorta. According to the topic of my thesis, special attention is paid to reasons of AAA's formation, health risks and methods to heal this disorder with the use of a stent-graft as a bridge element.

2.1 The aorta

The aorta (Figure 2.1) is the main trunk of a series of vessels which convey the oxygenated blood to the tissues of the body for their nutrition. It commences at the upper part of the left ventricle, where it is about 3 cm in diameter, and after ascending for a short distance, arches backward and to the left side, over the root of the left lung; it then descends within the thorax on the left side of the vertebral column, passes into the abdominal cavity through the aortic hiatus in the diaphragm, and ends, considerably diminished in size (about 1.75 cm in diameter), opposite the lower border of the fourth lumbar vertebra, by dividing into the right and left common iliac arteries [3]. On the basis of the previous information, the aorta can be formally divided into three portions:

- The ascending aorta
- The arch of the aorta
- The descending aorta.

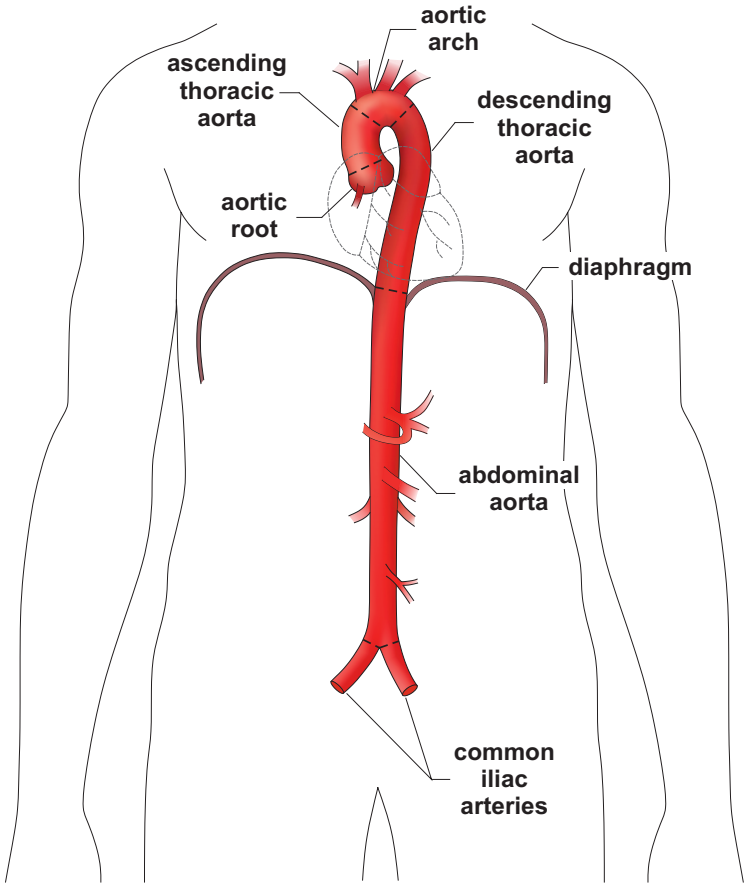

Figure 2.1: The aorta and its parts

The focus of this work is aimed especially to the lower part of descending aorta which is commonly referred to as abdominal aorta. Despite the fact that aneurysms can occur in any blood vessel, the number of aneurysms of abdominal aorta is significantly higher than other cases [4]. What is more, it carries the highest health risks when left untreated.

2.1.1 The abdominal aorta

The abdominal aorta (Figure 2.2) begins at the aortic hiatus of the diaphragm, in front of the lower border of the body of the last thoracic vertebra, and, descending in front of the vertebral column, ends on the body of the fourth lumbar vertebra, commonly a little to the left of the middle line. At this point, abdominal aorta ends with the aortic bifurcation by dividing into the two common iliac arteries. It diminishes rapidly in size, in consequence of the many large branches which it gives off [3].

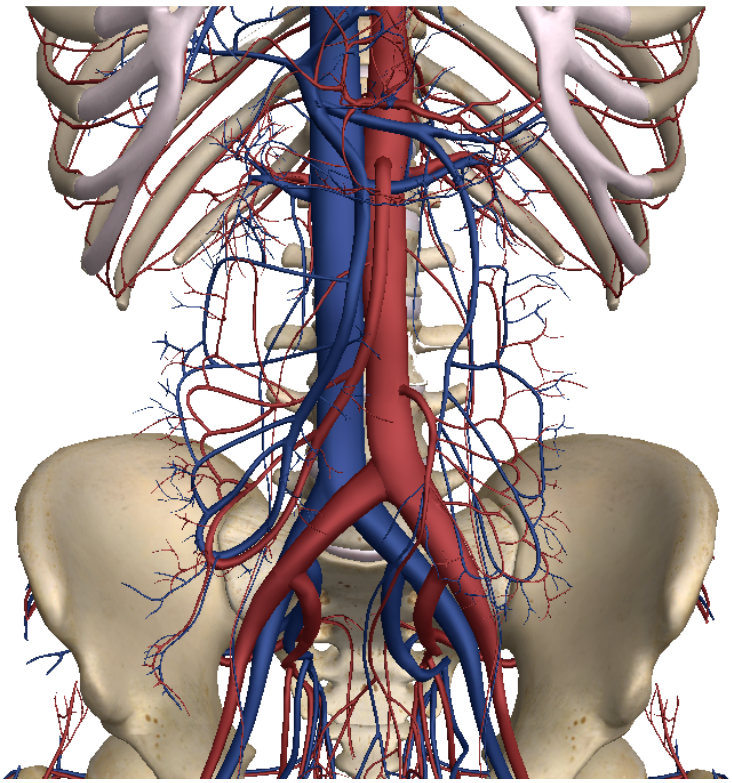

Figure 2.2: The abdominal aorta (highlighted in red) [5]

2.1.2 Structure of arteries

The arteries are composed of three coats: an internal or endothelial coat (*tunica intima*); a middle or muscular coat (*tunica media*); and an external or connective-tissue coat (*tunica adventitia*) (Figure 2.3). The two inner coats together are very easily separated from the external, as by the ordinary operation of tying a ligature around an artery. If a fine string be tied forcibly upon an artery and then taken off, the external coat will be found undivided, but the two inner coats are divided in the track of the ligature and can easily be further dissected from the outer coat [3].

The **inner coat** (*tunica intima*) can be separated from the middle by a little maceration, or it may be stripped off in small pieces; but, on account of its friability, it cannot be separated as a complete membrane. It is a fine, transparent, colourless structure which is highly elastic, and, after death, is commonly corrugated into longitudinal wrinkles [3].

The **middle coat** (*tunica media*) is distinguished from the inner by its colour and by the transverse arrangement of its fibres. In the smaller arteries it consists principally of plain muscle fibres in fine bundles, arranged in lamellæ and disposed circularly around the vessel. These lamellæ vary in number according to the size of the vessel; the smallest arteries having

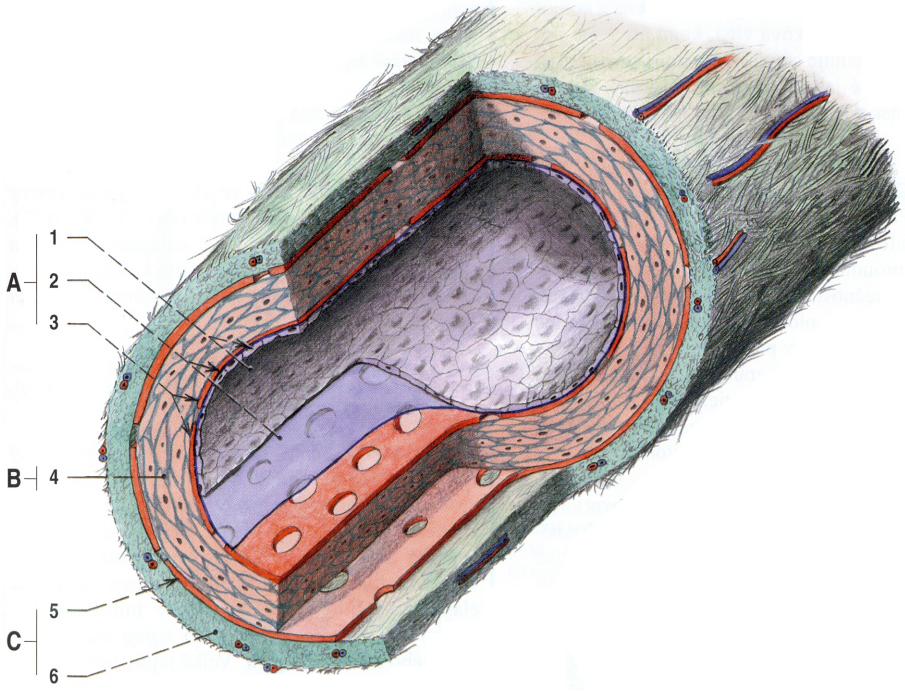

Figure 2.3: General structure of an arterial wall [6]:
A) tunica intima; B) tunica media; C) tunica adventitia

only a single layer and those slightly larger three or four layers. In the largest arteries, as the aorta and innominate, the amount of elastic tissue is very considerable [3].

The **external coat** (*tunica adventitia*) consists mainly of fine and closely felted bundles of white connective tissue, but also contains elastic fibres in all but the smallest arteries. The elastic tissue is much more abundant next the tunica media and it is some-times described as forming here, between the adventitia and media, a special layer, the tunica elastica externa of Henle [3].

2.1.3 Blood pressure in the aorta

Resting heart rate is about 70 beats per minute. The four periods of ventricular action thus take place within less than one second [7]. When the left heart ventricle ejects blood into the aorta, the aortic pressure rises. The maximal aortic pressure following ejection is termed the systolic pressure ($p_{systolic}$). As the left ventricle is relaxing and refilling, the pressure in the aorta falls. The lowest pressure in the aorta, which occurs just before the ventricle ejects blood into the aorta, is termed the diastolic pressure ($p_{diastolic}$) (Figure 2.4). Normal systolic pressure is 120 mmHg (16 kPa), and normal diastolic pressure is 80 mmHg (10.7 kPa). The difference between the systolic and diastolic pressures is the aortic pulse pressure, which typically ranges between 40 and 50 mmHg. The mean aortic pressure (p_{mean}) is the average

pressure (geometric mean) during the aortic pulse cycle [8].

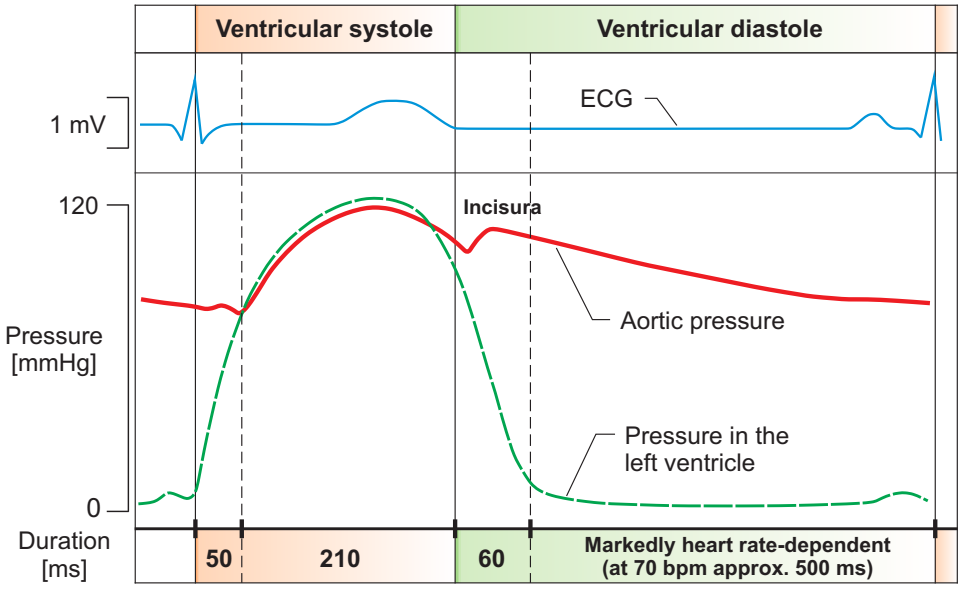

Figure 2.4: Evolution of blood pressure in aorta [7]

2.2 Abdominal aortic aneurysm

A consensus definition of aneurysm was published by the Society of Vascular Surgery and the International Society for Cardiovascular Surgery in 1991 [9]. The term refers to a permanent localised dilatation of an artery having at least a 50% increase in diameter compared with the expected normal diameter of the artery, or of the segment proximal to the dilatation [10].

True aortic aneurysms (Figure 2.5) are dilatations of the aorta that contain all layers of the artery wall. They usually balloon out from a local area but may involve the entire circumference [11]. The disorder is often defined via normal infrarenal aortic diameters in patients older than 50 years. The values of healthy aorta should be 1.5 cm in women and 1.7 cm in men. In the case the diameter of infrarenal aorta is 3.0 cm or larger it is considered aneurysmal [12, 13].

2.2.1 Causes of formation

For a long time, the AAA formation was strictly attributed to atherosclerotic degradation of the arterial wall [14]. Nevertheless, this view has been challenged in several works [9, 13] due to the fact that atherosclerosis usually causes narrowing of the arterial lumen. Thus, the historical association with atherosclerosis was expanded into multifactorial causation for the disease [9, 11, 15].

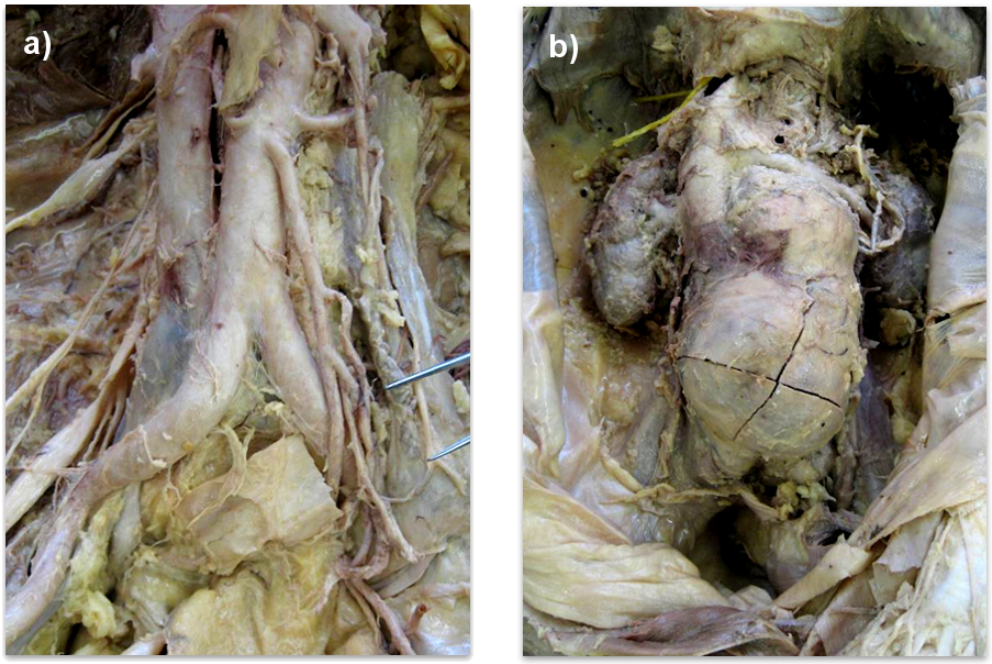

Figure 2.5: Pictures of a) healthy and b) aneurysmal abdominal aorta

Formation of an AAA is clearly connected with alterations of the connective tissue in the aortic wall [9, 13]. With vascular smooth-muscle cells, the key structural proteins elastin and collagen are arranged in concentric lamellæ to withstand the haemodynamic stresses imposed on the aortic wall [9, 16]. The architecture of these lamellæ allows for a stretching of elastin fibres with increasing load. As the vessel wall continues to stretch, collagen fibres uncoil and are progressively recruited as load-bearing elements. Under normal conditions, elastin is the principal loadbearing element, with collagen acting as a strong, almost indistensible "safety net". Destruction of the architecture results in aneurysmal dilation [9]. Elastin is not synthesised in the adult aorta. With a half-life of 70 years the amount of elastin in the aortic wall decreases with age. The age-related alterations in the vessel wall affect the mechanical properties of the aorta. This explains why AAA is primarily a disease of old age [9, 17].

Development of the disorder is strongly associated with tobacco smoking [18, 19, 20] which elicits an increased inflammatory response within the aortic wall [12, 21]. Many authors also point to the fact that AAA is one of the most common familial diseases [9, 13]. On the basis of the previous facts, Gilbert R. Upchurch defines risk group as following: age 65 years or older, male sex and smoking at least 100 cigarettes in a lifetime [12].

2.2.2 Health risks

The highest risk of an AAA lies in the fact that it remains asymptomatic in most patients. Moreover, the disorder is not detectable on physical examination and is commonly discovered

during radiologic testing for other reasons [12]. AAAs have tendency to enlarge [14] and, while not discovered or left untreated, the disorder ends by rupture of AAA which is usually fatal [22]. The overall mortality rate of patients with ruptured AAA is between 65% and 85% [13, 23] and this rate is even worse while rupture occurs outside the hospital [12]. The disorder is commonly present in more developed countries [13]. For instance, it is 13^{th} leading cause of death in USA [24].

The relationship between aneurysm size and risk of rupture is well known [14]. The annual risk of rupture is 0.5% to 2% for aneurysms less than 5 cm in diameter [14, 25], 5% for aneurysms 5 to 6 cm [26], 10% for 6.0 to 6.9 cm and 33% for AAAs of 7 cm or more [27].

2.3 Treatment of Abdominal Aortic Aneurysm

For more than 50 years aortic aneurysms have been treated with prophylactic open repair, a major surgical procedure done under general anaesthesia, usually consisting of a midline laparotomy and cross-clamping of the aorta for at least 30 min [14]. Then, in the early 1990s endovascular repair (EVAR) was introduced as a less invasive approach to treating infrarenal AAAs. In this approach, a stent-graft is placed endoluminally via bilateral groin incisions. Thus, there is no need for a major abdominal incision and aortic clamping [22].

In view of the rising chance of rupture, many surgeons have a policy of proceeding to repair when the AAA diameter has reached 5 or 5.5 cm or when growth of more than 1 cm per year is recorded [9]. On the other hand, the real controversy surrounds the management of smaller aneurysms (diameter between 4.0 cm and 5.5 cm) [13]. Various studies, in which authors compared the two means of treatment for this group of AAAs, were performed in past years [14, 22]. Conclusions of these works are similar: rigorous surveillance of infrarenal aortic aneurysms smaller than 5.5 cm in diameter is safe, whereas early surgery is not associated with improved long-term survival [13].

2.3.1 Open surgical treatment

The conventional open surgical treatment involves insertion of vascular prosthesis within the lumen of the aneurysm, firmly sutured to the non-dilated proximal and distal vascular segments (Figure 2.6). In most cases a tube graft is placed, but with extension of the aneurysm into the iliac arteries a bifurcated graft is used. The aneurysm itself is not resected and the aneurysmal sac is wrapped around the vascular prosthesis to prevent contact with the intestine [9]. The vascular graft is a knitted synthetic textile sealed with collagen or albumin [13].

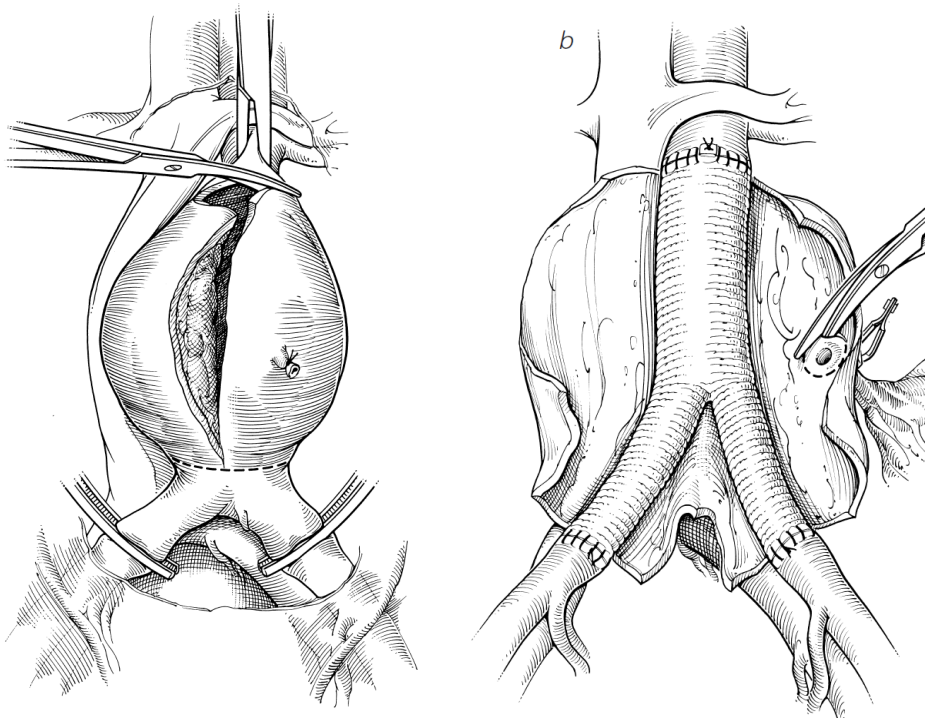

Figure 2.6: Open surgical treatment of AAA [14]
a) longitudal open of the aneurysmal sac, b) sewn bifurcated graft

2.3.2 Endovascular repair (EVAR)

This type of AAA treatment was firstly introduced by Parodi in 1991 [28]. The endograft is composed of fabric and metal stents and comes loaded in a delivery system. Under fluoroscopic guidance, this introducer system is fed through the iliac arteries by means of catheters and guidewires until the endograft is positioned correctly at the top and bottom of the aneurysmal segment. Removal of the introducer system allows the fixing devices to attach to the aortic wall and hold the graft firmly in place, excluding blood flow from the aneurysm sac and removing pressure from the aneurysm wall (Figure 2.7). Excellent results are characterised by a perfectly canalised blood flow and later by a completely retracted aneurysm wall around the endograft [13].

2.3.3 Endovascular repair vs. open surgery

According to the trials, which dealt with comparison of the two approaches for healing abdominal aortic aneurysms in recent years, the conclusion is following: Endovascular repair shows good results in 30-day operative mortality which is 0,5% to 1,6% versus 3% to 4,6% for open repair [22, 29]. On the other hand, long-term results do not reveal significant difference in mortality for the two methods (7% for EVAR vs. 9.8% for open surgery). Another

important factors that highlight the use of EVAR are reduced median procedure time (2.9 vs. 3.7 hours), blood loss (200 vs. 1000 ml) and hospital stay (3 vs. 7 days) [29].

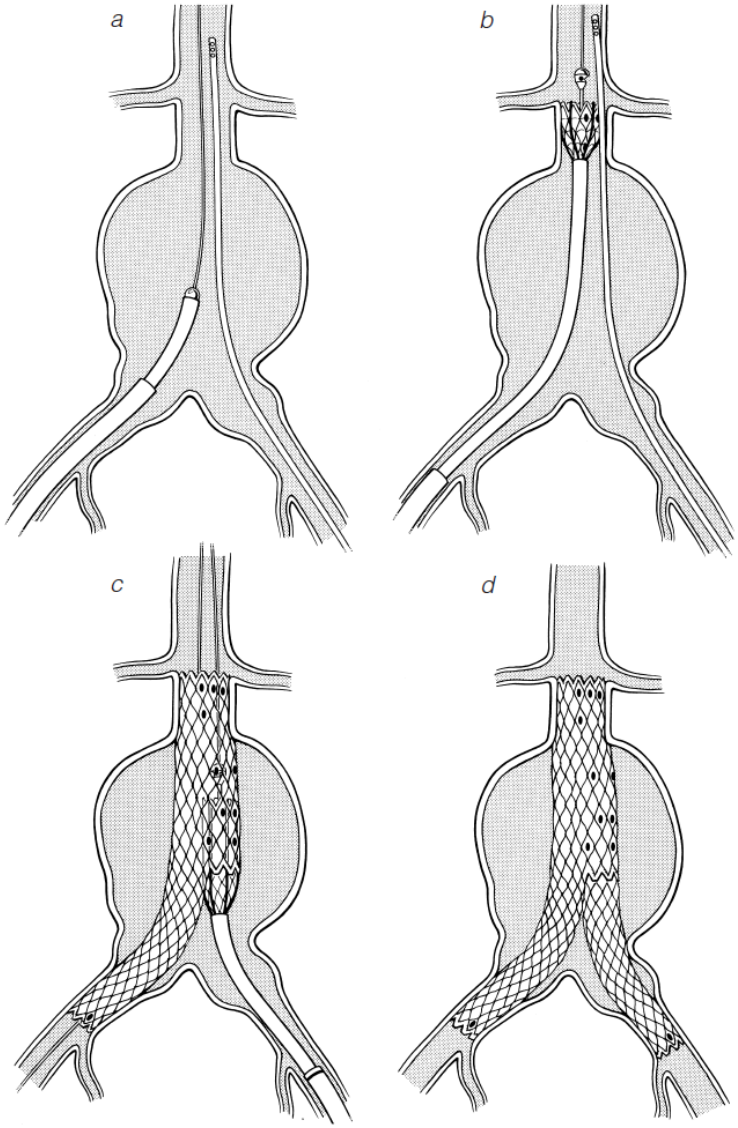

Figure 2.7: Endovascular repair of AAA (bifurctated stent-graft) [14]
a) introduction of leading wire
b) start of stent-graft deployment
c) implantation of stent-graft's second part
d) final form of bifurcated stent-graft

2.4 Types of endografts

Endovascular stent-grafts used in today's clinical practice can be divided into two major groups according to the constructional solution of their carrying part - the stent. First group, referred to as *Open Cells Design* is characterized by separate cells units which are connected together with small bridges. The other solutions is called *Closed Cells Design*. In comparison with previous type, these stents are formed of wires, coiled to the form of a helix. Several of these left and right helices are welded together which, as a whole, creates a robust construction. As usually, both designs have their pros and cons. For instance, closed cells design offers better support for graft but it is not capable to achieve such large bends as open cells design stent can. On the other hand, the small bridges that connect open cells are often a place of significant stress concentrations and ruptures. Nevertheless, clinical study performed by Martin Schillinger et al. did not reveal any major differences between the two solutions with respect to mortality risk [30].

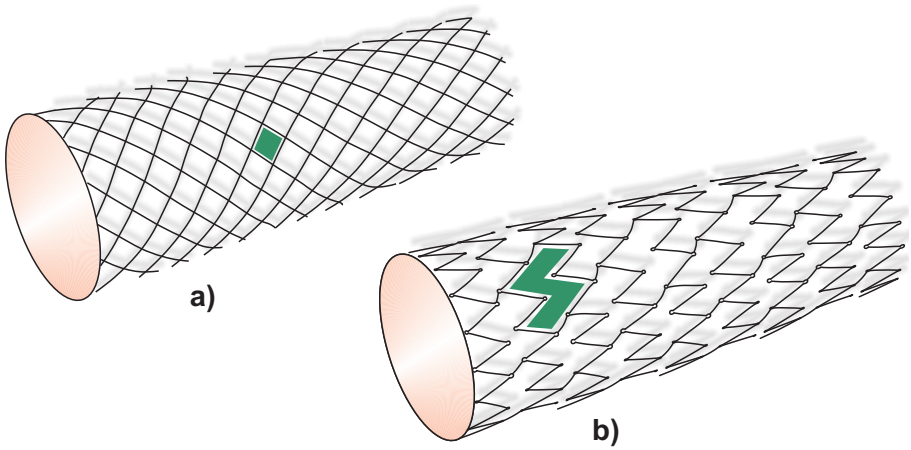

Figure 2.8: Expamples of stent designs
a) Closed cells design
b) Open cells design

Endovascular stents produced by ELLA-CS (Figure 2.9) can be assigned to open cells design group. Its special feature is that stents are not connected together by bridges but they act as standalone units. In this case, graft does not only serve to exclude blood flow from aneurysmal sac but it also forms a significant structural part of the whole device. Connection between stent and graft is realized simply by sutures tied around a graft. Advantage of such a solution lies in better performance in parts of arteries with complex shape, e.g. in common illiac arteries.

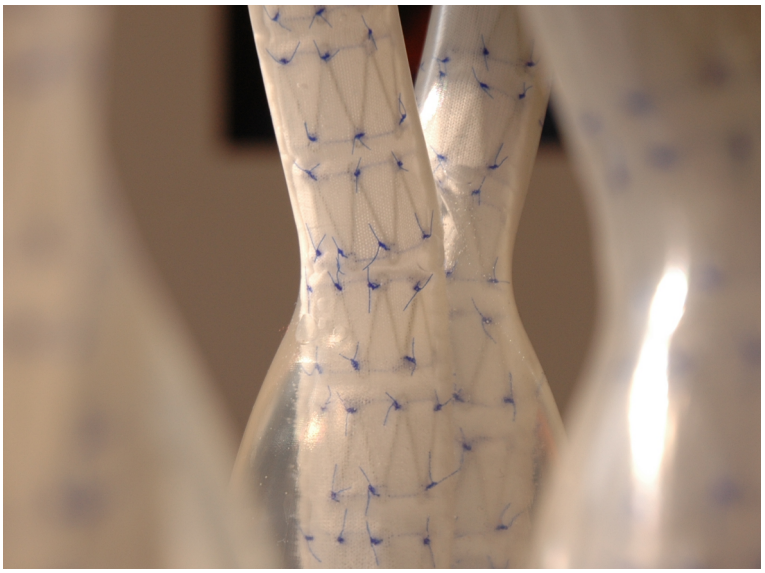

Figure 2.9: Endovascular stent-graft produced by ELLA-CS

Chapter 3

NiTi Alloy

As noted in Chapter 1, thermally and mechanically induced martensitic transformation mechanisms of SMAs are reviewed in this chapter. Then, the two most significant properties which are based on these mechanisms - shape memory effect and pseudoelasticity, respectively - are briefly introduced. With respect to the thesis objectives, the text deals with macroscopic effects of the transformations only. Metallographic properties of the transformation are thoroughly explained in publication of Otsuka and Wayman [31]. Another important issue which had to be reviewed was behaviour of NiTi under cyclic loading and its fatigue properties. The last part of this chapter is dedicated to introduction of available SMAs constitutive models, one of which is then selected for finite element method analysis in Chapter 6.

3.1 Reversible martensitic transformation

The formation of martensitic structure in conventional materials is usually an irreversible process. For instance, in the most common Fe-Fe_3C system it is induced by fast cooling (quenching) from high temperature austenite with the rate of approx. 450°C/s. The result of the procedure is highly unstable martensite with centre cubic form. As stated above, the resulting structure cannot be undone. Under certain conditions, SMAs are able to spontaneously change their inner structure forwards (A→M) and backwards (M→A). This is exactly the point that gives them their unique properties and which distinguish them from conventionally used materials.

It was not until 1949 that the researchers Kurdjumov and Khandros discovered reversible martensitic transformation in CuZn and CuAl alloys [32]. Despite its great potential, this phenomenon was not utilized in any application until 1963 [32]. This year marks discovery of NiTi alloy at the Naval Ordnance Laboratory in White Oak, Maryland, USA. In honour of the place of its finding, the alloy is often referred to as NiTiNOL [32]. Nowadays, there are numerous applications of NiTi in fields such as aeronautics, automotive and medicine.

3.1.1 Thermally induced martensitic transformation

Consider that we have NiTi specimen which inner structure is composed of parent phase only, i.e. high temperature austenite. Under constant value of stress, temperature of the specimen is slowly decreased. While achieving certain temperature (M_s), a diffusionless, shearlike [31] formation of martensite begins and the whole process is finished while reaching point M_f. Up until certain value of stress (σ_s), the resulting structure is called self-accommodated [31] or twinned [32] martensite. When the applied stress is high enough, the resulting structure is called detwinned [32] or reoriented [31] martensite. The difference between the two types of martensite lies in orientation of their variants. In the case of twinned martensite, variants are oriented in various directions, while in the other type, one direction of variants is predominating [32]. The inner structure can be restored to its initial state simply by heating up the specimen, achieving temperatures A_s and A_f thereafter.

The whole above described process is depicted in stress-temperature diagram (Figure 3.1). One can note that a different value of applied stress represents different values of transformation temperatures.

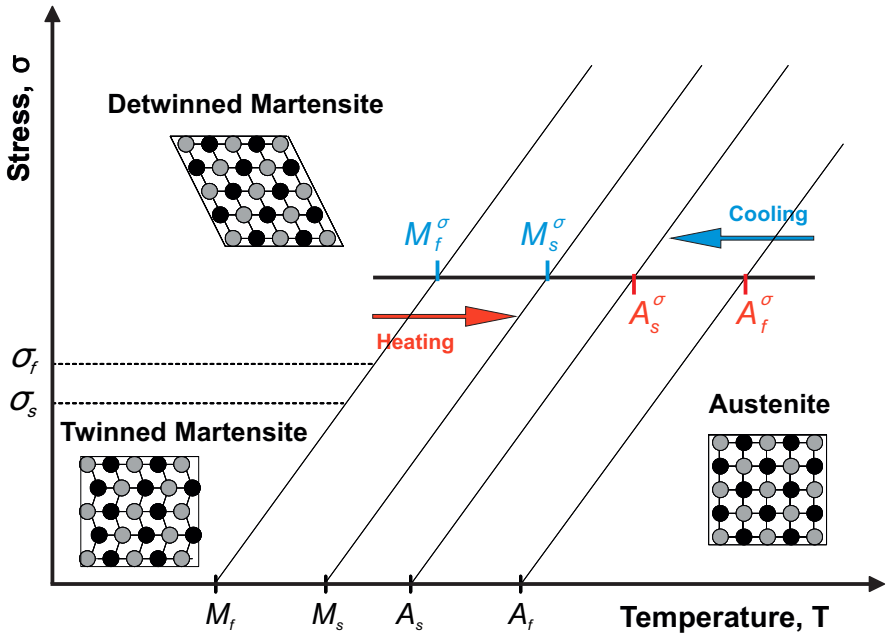

Figure 3.1: Thermally induced martensitic transformation [32]

3.1.2 Stress induced martensitic transformation

Again, consider a specimen in austenitic phase but in contrast with previous case, it is now loaded with rising value of stress at constant temperature. At certain level of stress (σ^{Ms}), martensite starts to form and while reaching σ^{Mf}, the inner structure of the specimen has fully

transformed into detwinned martensite (Figure 3.2). This process can be undone by release of the load. As a consequence, the inner structure will return back to austenitic phase.

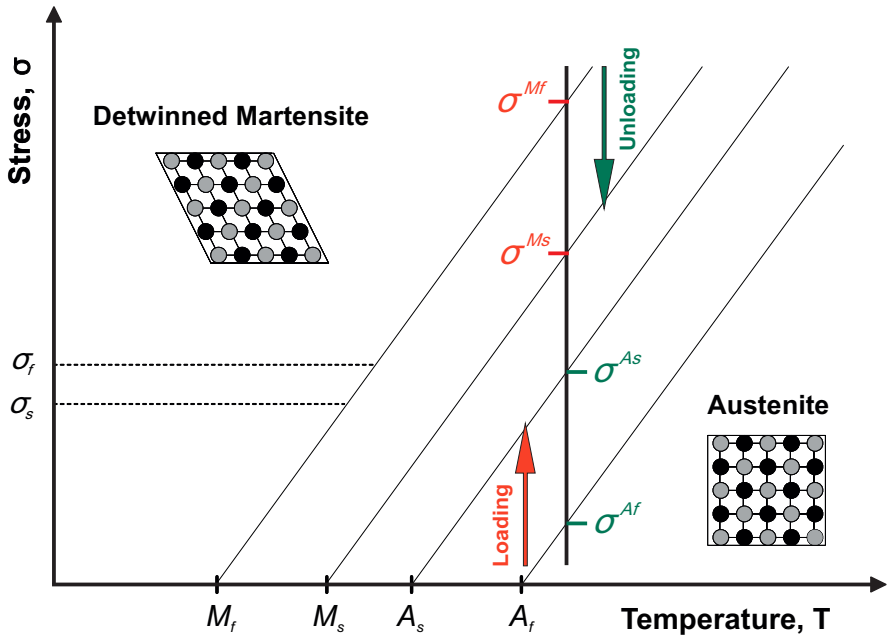

Figure 3.2: Stress induced martensitic transformation [32]

3.2 Shape Memory Effect (SME)

Shape memory effect is mainly associated with thermally induced martensitic transformation. Nevertheless, stress plays a crucial role in this process as well.

Generally, first step of inducing shape memory effect is cooling down a stress-free specimen of given shape from austenitic phase to twinned martensite (as explained in Section 3.1.1). Then, sufficiently high stress is applied to form detwinned martensite. This step results in a macroscopic change of shape and after the stress is released, the specimen remains in this new configuration. To finish SME, specimen is warmed up. After the austenitic structure is achieved again, specimen's initial shape is completely restored.

Amazing application of SME is described in publication of Otsuka and Wayman [31] - a space antenna which is formed of NiTi wires. To transport this device to Earth's orbit, it is cooled down and deformed into form of little sphere. When released to open space, solar heat warms up the material and it recovers its original, dish-like shape.

3.3 Pseudoelasticity

In contrast with SME, pseudoelasticity is almost exclusively connected with stress induced martensitic transformation. Heat changes may or may not be present. When drawing the loading path marked in Figure 3.2 to σ–ε diagram, we can observe a typical pseudoelastic behaviour of NiTi (Figure 3.3).

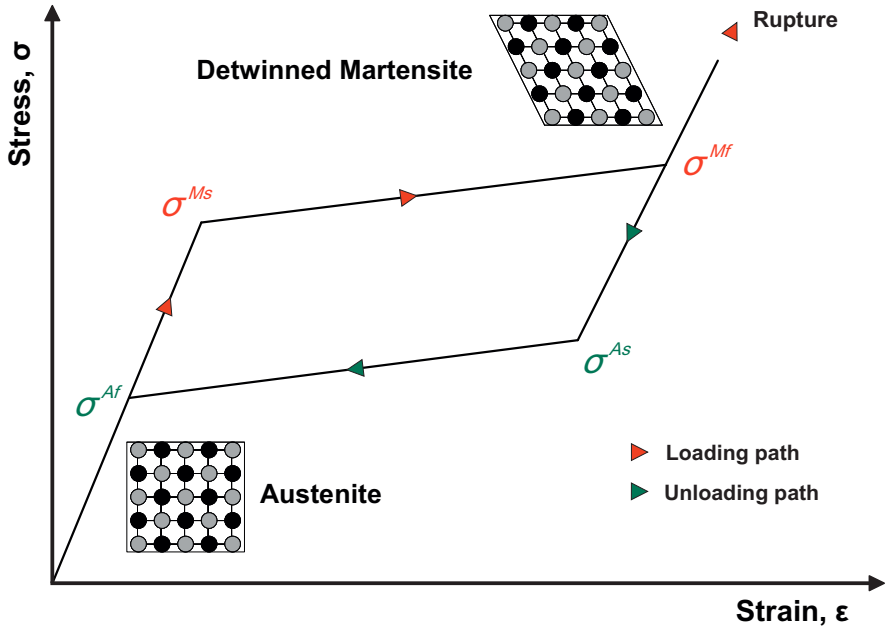

Figure 3.3: Simplified pseudoelastic behaviour of SMAs [32]

When following the pseudoelastic cycle from its initial state (at zero stress and strain), it begins with linear-elastic part of parent austenitic phase. Then, while reaching the stress level needed for inception of martensitic transformation (σ^{Ms}), the behaviour of material changes dramatically. The whole stress induced transformation is accompanied by large inelastic strains [32] and thus leap in curve slope. Above described part of pseudoelastic cycle (between σ^{Ms} and σ^{Mf}) is often referred to as superelastic plateau [33, 34].

After the transformation is finished, the curve slope changes again and following part is characterised by elastic behaviour of detwinned martensite [32]. No other transformation takes place until a potential rupture of the specimen. Nevertheless, to finish the cycle, the specimen is gradually unloaded which, at stress level σ^{As}, causes the beginning of transformation to austenite. Similarly to martensitic transformation, the austenitic transformation takes place under almost constant value of stress while large strains are present. As soon as the backward transformation is finished (at stress level σ^{Af}), the cycle ends by elastic unload to its starting point.

The complete pseudoelastic cycle forms a hysteresis loop which represents the energy

dissipated in the transformation cycle. All the transformation stress levels and form of resulting hysteresis loop is strongly dependent on type of SMA, its heat treatment and testing conditions [31, 32].

3.4 Behaviour under cyclic loading

Cycling effects on NiTi specimen along various thermomechanical loading paths are well known. These properties, among all the others, were examined by several authors and research teams since the discovery of NiTi [35, 36]. Similarly to description of NiTi's basic properties in previous sections, behaviour under cyclic loading is most often evaluated in purely thermal cycling with constant value of stress or in pseudoelastic regime only. Regardless to which of the two methods we choose, the cycling response is similar, i.e. formation of hysteresis loop which tends to stabilize its width and size with increasing number of cycles. The process of cycling the material along a specific loading path until the saturation takes place is called *training* [31, 32].

3.4.1 Thermal cyclic loading

Typical behaviour of a NiTi specimen which is subjected to thermal cyclic loading is shown in strain-temperature diagram in Figure 3.4. In this case, a specimen is a NiTi wire loaded with constant stress of 200 MPa. When we perform one complete thermal cycle, under which the material undergoes forward and backward transformation, it forms a hysteresis loop. The loop evolves with increasing number of cycles and it stabilizes after about a hundred repetitions [37, 38]. At the end of each cycle, only part of the strain is recovered, leaving a certain amount of inelastic (or irrecoverable) deformation. Value of this permanent strain is very considerable in early cycles but it cease to further accumulate as soon as the stabilisation of the hysteresis loop is achieved [31, 32].

Concerning the overall properties of NiTi exposed to thermal cycling, the changes in its microstructure cause shifting of transformation temperatures. This is especially case of M_s and M_f points which rises with increasing number of cycles (Figure 3.4). The process is in accordance with observations of most of the authors [40]. Nevertheless, some of the publications deals with opposite behaviour, i.e. transformation temperatures decrease with number of cycles even for the same material [41].

3.4.2 Cycling in pseudoelastic domain

Unlike the contradictions in data of thermal cycling effects which were discussed in previous section, the results of training a NiTi material in pseudoelastic domain are consistent in most of the publications. Resulting evolution of hysteresis loop in σ–ε diagram is shown in Figure 3.5

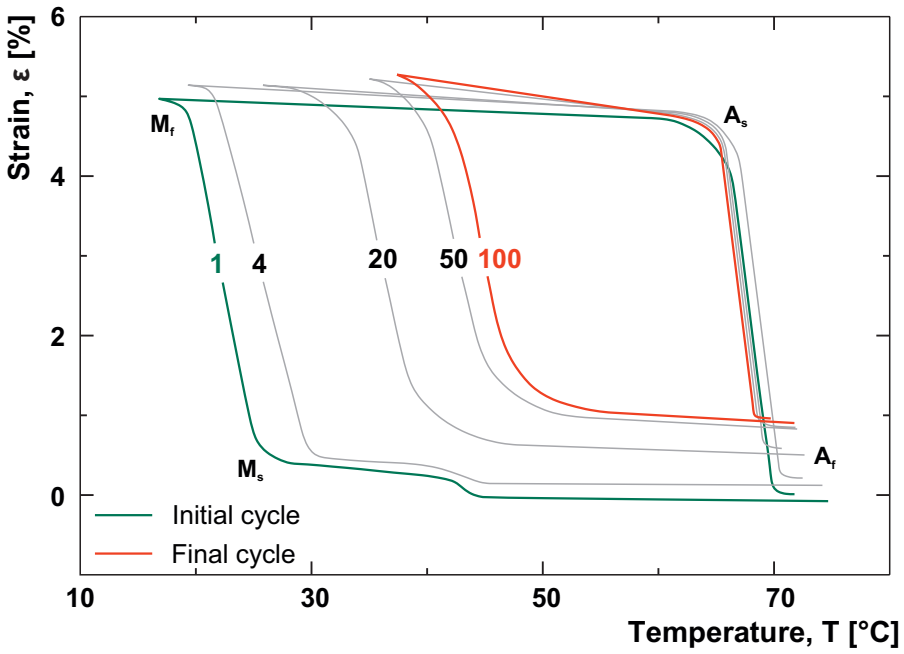

Figure 3.4: Effects of thermal cycling on NiTi specimen [39]

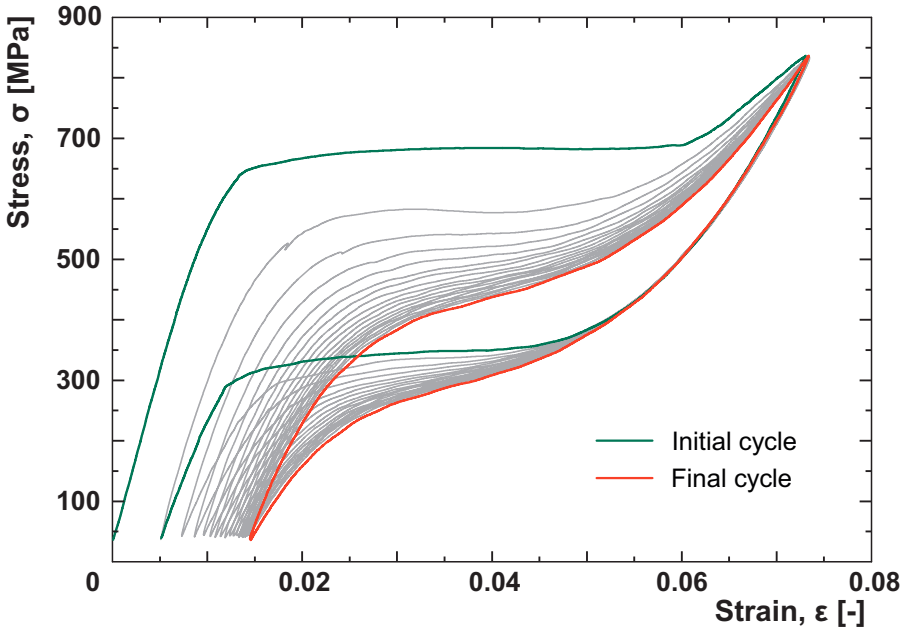

Figure 3.5: Effects of mechanical cycling on NiTi specimen in pseudoelastic domain [32]

Similarly to behaviour under thermal cyclic loading, changes of the loop are very considerable during first few cycles but then gradually decreases until a saturation takes place. Yield stress and hysteresis width of the loop decrease [31] with rise of the permanent strain during each cycle.

On the basis of the facts mentioned above, the NiTi products which are meant to function in some sort of cyclic thermomechanical loading procedure are strongly recommended to undergo a training process along this path before their actual use. Not only does this step stabilize their properties but its following reliable service is also ensured.

3.5 Fatigue properties of NiTi

With regard to behaviour of NiTi alloy which it exhibits under various conditions, it is not possible to judge its fatigue properties only in conventional way. In fact, there are three parameters which should be taken into account when evaluating fatigue of shape memory alloys, i.e. temperature, applied stress and macroscopic shape strain during deformation [31]. Usually, the influence of these parameters is evaluated separately which defines two major group of SMA fatigue:

1. Conventional failure by fracture due to stress or strain cycling at constant temperature either through the transformation region or in elastic regime of the material only.

2. Degradation of physical, mechanical and functional properties, including shift of transformation temperatures, shape of hysteresis loop and degradation of shape memory effect due to pure thermal cyclic loading through transformation region.

3.5.1 Mechanical fatigue

In spite of the fact that much work was done on the account of NiTi's mechanical fatigue properties, reliable data are still missing. Vast majority of publications deal with microscopic mechanisms of material fatigue [36, 42, 43]. These publications reveals accumulation of dislocations during mechanical cycling and describes occurrence of irreversible strain as introduced in Section 3.4.2.

Those papers which main goal was evaluation of S-N curves, i.e. stress amplitude vs. number of cycles at failure dependency, remains only qualitative due to a big scatter in resulting data [44]. In the case of NiTi as well as the whole group of shape memory alloys, the fatigue properties depends on multiple factors such as alloy composition, heat treatment, grain size and fabrication process. For instance, influence of heat treatment of the specimens before testing is shown in Figure 3.6. In his case, the specimens were made of near-equiatomic NiTi alloy (50.8 at% Ni) and submitted to annealing at different temperatures for one hour, followed by quenching in iced water. Final specimens were then subjected to cycling at room

temperature. Results shows distinct fatigue limits of these specimens. Second figure 3.7 reveals dependency of fatigue limit on grain size of the material. Although this graph is evaluated for Cu-Zn-Al SMA, similar behaviour should be expected in the case of NiTiNOL as well.

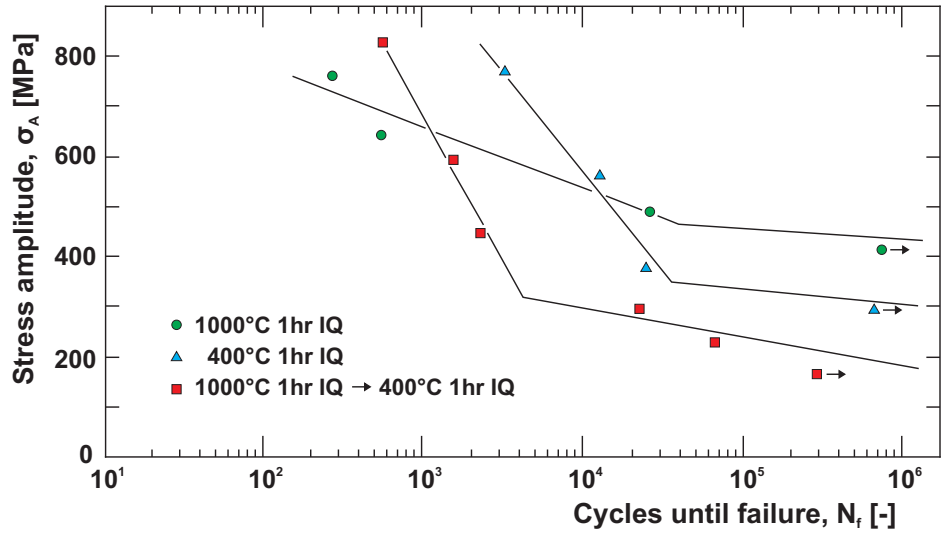

Figure 3.6: Effect of heat treatment on the fatigue life of the NiTi alloy [45]

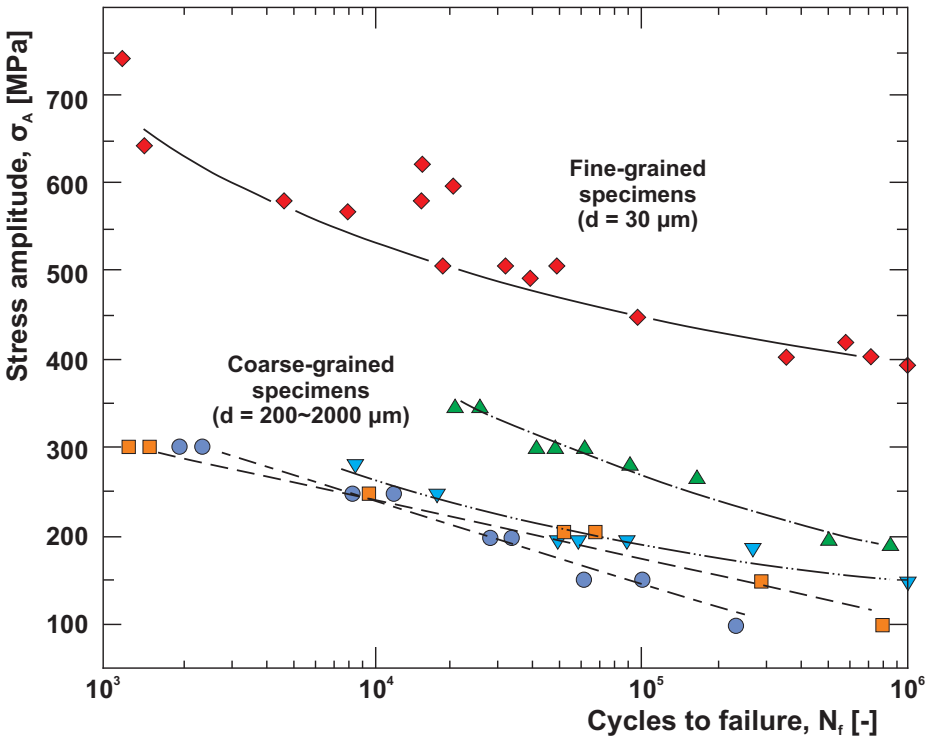

Figure 3.7: Fatigue life in fine- and coarse-grained Cu-Zn-Al specimens [46]

Despite all the drawbacks of determining fatigue life of NiTi, there are two facts which can be derived from above mentioned publications. In the case that the material is cycled in parent austenitic phase, it usually withstands more than 10^7 cycles without any problem [47]. On the other hand, as soon as the transformation levels are crossed, fatigue life rapidly decreases to the level of thousands of cycles [43, 48].

Few authors also tried to use an energy approach to create a criterion for estimation of fatigue life. For instance, Ziad Moumni et al. [49] developed a criterion based on the similarity with plastic shakedown phenomenon [50] which is observable in conventionally used materials. Author measured an evolution of dissipated energy vs. number of cycles at failure. Despite its great potential, this criterion is usable especially for low cycle fatigue.

As a consequence of above discussed facts, fatigue properties of the material must be evaluated for each case separately, while keeping the external factors consistent for all the tested specimens.

3.5.2 Thermal fatigue

This type of fatigue does not usually lead to failure due to destruction of the material. Nevertheless, when performing a complete or partial forward and backward transformation, a degradation of material's properties takes place. This can cause a problem in such applications where SMAs undergoes repetitive temperature changes. Apart from the factors which were listed in previous section, there are another two values which should be taken into consideration: a tress level under which the material is cycled and a measure of transformation strain [32].

Interesting side effect of cyclic thermal loading on NiTi specimen is occurrence of a phenomenon called *Two-way shape memory effect* (TWSME). This is due to introduction of dislocations in material's parent phase [31, 32]. As a consequence, a shape of the NiTi specimen is not only remembered in austenitic phase but also in martensitic phase. Standard behaviour of the material as described in Section 3.1.1 is therefore infringed because macroscopic changes of the specimen are present even during forward transformation.

3.6 Constitutive material models

Unique behaviour of shape memory alloys represented a huge challenge for researchers to develop a successful constitutive material model. During last three decades, many of these models arose and they are usually divided into two groups. One of these groups is characterized by covering only pseudoelasticity effect of Shape Memory Alloys. These models are often based on a common plasticity model with calibration via SMA's transformation stress levels. Second and much larger group deals with shape memory behaviour as well. In comparison with previous, models which belong to the latter group must deal with both possible states of

martensite - twinned and detwinned. The models are most often formulated with Helmholtz or Gibbs free energy.

Due to the fact, that the most successful constitutive models were thoroughly reviewed in publication of D. C. Lagoudas [32], this section will only be aimed to a description of the two models which are already implemented in MSC.Marc Software. These are Auricchio mechanical model and Saeedvafa & Assaro thermomechanical model. Following description is only a short view into functionality of the models, the whole theory can be found in articles listed in following two subsections.

3.6.1 Auricchio mechanical model

As mentioned above, Auricchio's model covers pseudoelastic effect of SMAs only. Proposed work [51] is an expanded 1-D plasticity-based model, which was published in 1997 [52, 53]. The model uses deformation gradient $\mathbf{F}$ as the control variable and the martensite fraction, ξ_s, as the only scalar internal variable. To take a stress induced martensite transformation into account, a multiplicative decomposition of $\mathbf{F}$ to elastic $\mathbf{F}^e$ and phase transformation part $\mathbf{F}^{tr}$ is used:

$$\mathbf{F} = \mathbf{F}^e \mathbf{F}^{tr} \tag{3.1}$$

This formal split of deformation gradient is then further developed and both components are linked with internal variable ξ_S and other material parameters. In order to maintain plastic-like behaviour of SMA, a Drucker-Prager-type yielding criterion as a function of Kirchhoff stress $\boldsymbol{\tau}$ is used:

$$F(\boldsymbol{\tau}) = \|\mathbf{t}\| + 3\alpha p \tag{3.2}$$

where α is a material parameter, p is pressure and $\|\mathbf{t}\|$ indicates Euclidean norm of deviatoric part of $\boldsymbol{\tau}$. Last notable part of Auricchio mechanical model are the time-discrete evolutionary equations, which defines evolution of martensite fraction:

$$\mathcal{R}^{AS} = \left(F - R_f^{AS}\right) \lambda_s + H^{AS}(1 - \xi_s)(F - F_n) = 0 \tag{3.3}$$

$$\mathcal{R}^{SA} = \left(F - R_f^{SA}\right) \lambda_s + H^{SA}\xi_s(F - F_n) = 0 \tag{3.4}$$

Equations 3.3 and 3.4 are related to forward (A→M) and backward (M→A) transformation, respectively. Constants H^{AS} and H^{SA} gain value of zero or one, according to relation of Drucker-Prager type function 3.2 to a function in which material constants σ^{Ms}, σ^{Mf}, σ^{As} and σ^{Af} (see Section 3.3) are included.

3.6.2 Saeedvafa & Assaro thermomechanical model

In contrast with previous SMA material model, Saeedvafa & Assaro thermomechanical model is capable of taking into account not only effects of pure mechanical loading but also contribution of temperature changes. In addition, the model deals with plasticity of parent and product phases. The model itself is based on kinematics of small strains and the overall incremental strain is the sum of incremental elastic, thermal, plastic strain and the strain associated with thermoelastic phase transformation:

$$\Delta\boldsymbol{\varepsilon} = \Delta\boldsymbol{\varepsilon}^{El} + \Delta\boldsymbol{\varepsilon}^{Th} + \Delta\boldsymbol{\varepsilon}^{Pl} + \Delta\boldsymbol{\varepsilon}^{Ph} \tag{3.5}$$

The incremental elastic strain is related to a set of elastic moduli and the incremental Cauchy stress rate:

$$\Delta\boldsymbol{\varepsilon}^{El} = \mathbf{L}^{-1} \colon \boldsymbol{\sigma} \tag{3.6}$$

Thermal contribution to overall strain is defined with volume average thermal expansion coefficient α of the both phases and temperature change:

$$\Delta\boldsymbol{\varepsilon}^{Th} = \alpha\Delta T\mathbf{I} \tag{3.7}$$

The plastic strain increment of the two-phased aggregate as well as that of each phase is assumed to be governed by J_2-flow theory, that is:

$$\Delta\boldsymbol{\varepsilon}^{Pl} = \Delta\lambda\frac{3}{2}\frac{\boldsymbol{\sigma'}}{\sigma_{eq}} \tag{3.8}$$

Last and maybe the most important part of this SMA material model is determination of phase transformation strain. Due to the fact that the model has to deal with both stress and thermally induced martensitic transformation, $\Delta\boldsymbol{\varepsilon}^{Ph}$ is, again, divided into two terms:

$$\Delta\boldsymbol{\varepsilon}^{Ph} = \Delta\boldsymbol{\varepsilon}^{Trip} + \Delta\boldsymbol{\varepsilon}^{Twin} \tag{3.9}$$

with the two components defined as following:

$$\Delta\boldsymbol{\varepsilon}^{Trip} = \Delta f^{M} g(\sigma_{eq})\varepsilon^{T}_{eq}\frac{3}{2}\frac{\boldsymbol{\sigma'}}{\sigma_{eq}} + \Delta f^{M}\varepsilon^{T}_{v}\mathbf{I} + \Delta f^{A}\boldsymbol{\varepsilon}^{Ph} \tag{3.10}$$

$$\Delta\boldsymbol{\varepsilon}^{Twin} = f\Delta g(\sigma_{eq})\varepsilon^{T}_{eq}\frac{3}{2}\frac{\boldsymbol{\sigma'}}{\sigma_{eq}}\{\Delta\sigma_{eq}\}\{\sigma_{eq} - \sigma^{g}_{eff}\} \tag{3.11}$$

As it can be seen, the behaviour of this model is driven according to the value of Equivalent Von Mises Stress (σ_{eq}). Apart from all the other values which appear in equations 3.10 and 3.11 the most noticeable part is so called g-function $g(\sigma_{eq})$. This function calibrates the model according to the specific shape memory alloy and it represents a measure of the extent to which the martensite transformation strains are aligned with the deviatoric stress. Mathematically, this relation is prescribed as following:

$$g(\sigma_{eq}) = 1 - \exp\left[g_a \left(\frac{\sigma_{eq}}{g_0}\right)^{g_b} + g_b \left(\frac{\sigma_{eq}}{g_0}\right)^{g_d} + g_e \left(\frac{\sigma_{eq}}{g_0}\right)^{g_f}\right] \tag{3.12}$$

In most of the cases, only the first term in bracket of equation 3.12 is sufficient to calibrate the model. Therefore, constants g_c and g_e are usually set to zero. To find precise values of g_a and g_b, it is necessary to perform a tensile test in material's fully twinned martensitic state, i.e. bellow M_f temperature.

Chapter 4

Basics of fatigue analysis

Throughout the past few decades, several definitions of fatigue as a material property were established. Nevertheless, the most recognized explanation of fatigue refers to "failure of the material under repeated or otherwise varying load which peak value never reaches a level high enough to cause rupture of the material in a single application". Fatigue is a degradation process which leads to irreversible damages of material's inner structure and, thanks to cyclic plastic deformation, to initiation and propagation of fatigue cracks. Fatigue is often confused with another two terms related to behaviour of the material under cyclic loading, i.e. *fracture* and *durability*. While the term *fracture* refers to consequence of fatigue process, durability can be defined as an ability of the final product to reliably withstand defined value of cycles, hours of work or similar time-related measures.

Determination of fatigue properties is of great importance in today's mechanical engineering practice. Seldom does the fracture occurs due to crossing the ultimate strength of the material and most of the material failures are therefore caused by fatigue. For instance, in 1982's Battelle Institution study a percentage of fatigue-related failures was estimated to range of 80% to 90% [54].

4.1 Fatigue curves

Generally, total fatigue life of a material or particular part can be decomposed to stages of initiation and propagation of fatigue crack as depicted in Figure 4.1. In many areas of mechanical engineering such as automotive industry, the prediction of total life is the only desired quantity. On the other hand, moment of crack initiation and especially speed of its grow are crucial for another fields such as aeronautics. With respect to the these two areas of interest, there are two testing approaches which define fatigue life. First and historically older approach evaluates stress amplitude vs. number of cycles to failure dependency hence the resulting relation is called the S-N curve. The data gained from the method are more suitable for evaluation of total fatigue life without considering a moment of crack initiation.

Second approach which result is ε-N curve is characterized by position driven cyclic tests. With contrast with the previous, this fatigue curve is more suitable for methods which predict crack initiation and its growth. Each of those two methods has its importance and their general areas of use are summarized in following two subsections.

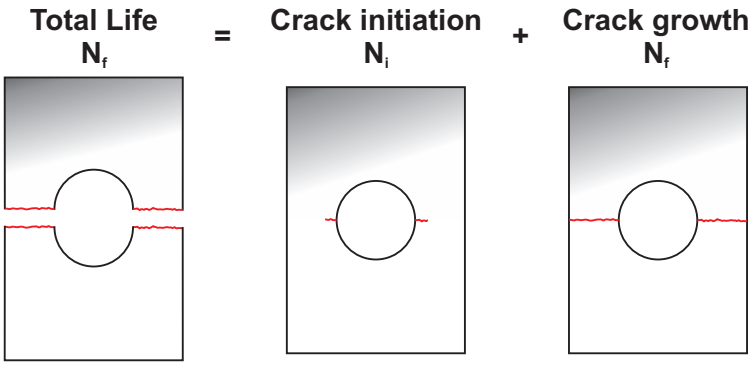

Figure 4.1: Stages of overall fatigue life

4.1.1 S-N fatigue curve

Foundation of this method can be attributed to August Wöhler who performed rotating-bending tests of railway axles in 1950's. The approach, also referred to as total life, is characterized by material tests which are carried out under force (or stress) control. As a result, we obtain the stress amplitude vs. number of cycles until failure dependency (Figure 4.2). To evaluate a material S-N curve, the specimens are ordinarily tested at three to five levels of stress amplitude. In order to obtain statistically useful data, each level is characterized by test of three to ten specimens. Tests are most often performed under fully reversed harmonic cycle with ratio $R = \frac{\sigma_{min}}{\sigma_{max}} = -1$. In the case that it is not possible to apply either tensile or compressive load (for instance for specimens in the form of wires, bricks, etc.), the test are carried out under constant value of mean stress σ_m or constant value of R ratio. To sum up, the conditions under which the S-N curve was evaluated must be clearly quantified in order to be able to apply these data to life prediction of final part.

One of the most important value gained from fatigue tests is the fatigue limit of the material σ_c. This value is recognized as a stress amplitude under which the specimen is able to withstand infinite number of cycles. As depicted in Figure 4.2, this value divides resulting diagram to areas of infinite and limited life. In the case that a material does not show distinct fatigue limit, the value is represented by so called endurance limit at 10^7 cycles. Apart from that, there are three significant areas which are distinguished by mechanism of crack growth and following fatigue failure:

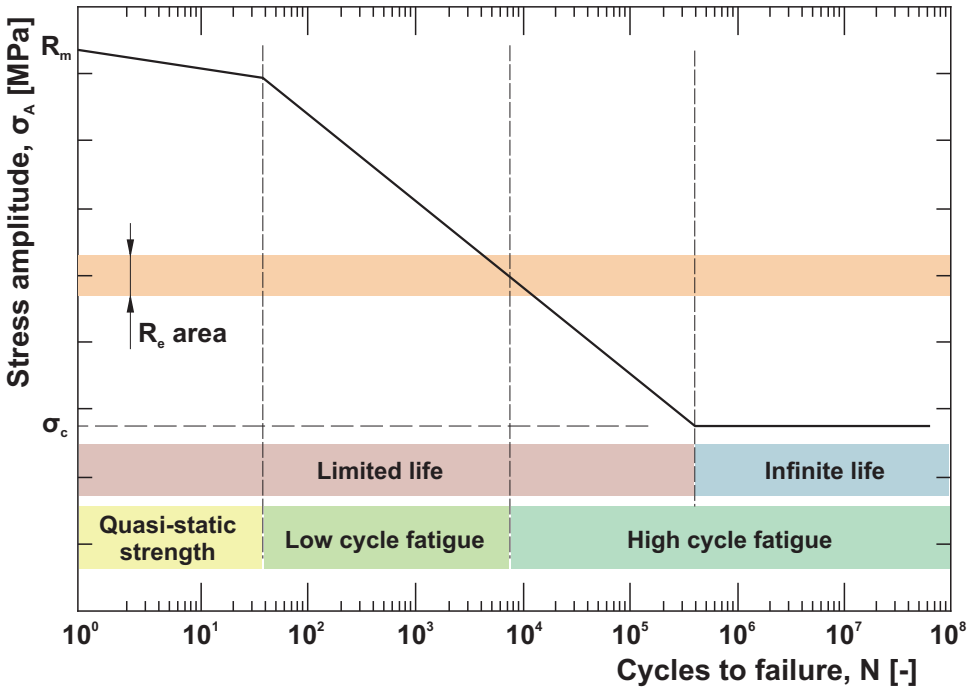

Figure 4.2: Typical form of S-N curve for an alloy with distinct fatigue limit

1. *Area of Quasi-static Strength*

   First area is characterized by the fact that applied stress amplitudes are so high that failure occurs during either first cycle or several decades of cycles. This part is commonly not considered as part of fatigue curve because rate of crack occurrence and growth is very fast and resulting form of rupture is similar to the one caused by monotonic loading.

2. *Low Cycle Fatigue*

   While testing in Low Cycle Fatigue region, the stress amplitude reaches level well above Yield Stress of the material R_e. Thus, cyclic plastic deformations are present in the whole volume of specimen. Due to the fact that value of R_e represents threshold between linear and non-linear behaviour of the material, it also forms a boundary with last region of S-N diagram, i.e. High Cycle Fatigue.

3. *High Cycle Fatigue*

   If a rupture due to loading in High Cycle Fatigue region occurs, resulting surface of the fracture shows distinct border between two parts. First of them has polished-like look and it is caused by slow progression of fatigue crack. At some point, final rupture caused by overload of rest of the material occurs. Surface of this rupture is much coarser, similar to the one present in monotonic loading.

In the elastic part of S-N curve, i.e. in High Cycle Fatigue area, experimental data can be analytically characterized according to Basquin's power law (Equation 4.1). This relation will display as a linear function with slope $1/w$ in the case that S-N curve is plotted in log-log scale.

$$\sigma_a^w \cdot N = C \tag{4.1}$$

In Low Cycle Fatigue and in the case of complex loading history, the Basquin's equation is often expressed in relation to reversals N_f instead of the whole cycles to failure. Then, the equation is defined with Fatigue Strength Coefficient σ'_f and the Fatigue Strength Exponent b as following:

$$\sigma_a = \sigma'_f \left(2N_f\right)^b \tag{4.2}$$

4.1.2 ε-N fatigue curve

S-N approach is not very convenient method for the Low Cycle Fatigue region. When performing a test, the first cycle is accompanied with large strain because of crossing the yielding point of the material. In the following cycles, on the other hand, plastic strain is much smaller because of plastic strain hardening of the material. Thus, materials which are meant to operate in Low Cycle Fatigue are frequently examined via strain-driven tests, i.e. ε-N approach. In the fifties, Manson and Coffin proposed a model for approximation of plastic contribution to overall strain:

$$\varepsilon_{ap} = \varepsilon'_f \cdot (2N)^c \tag{4.3}$$

The total strain is a sum of its elastic and plastic part. The elastic part can be expressed from Equation 4.2 and final form of Manson-Coffin equation can be written as following:

$$\varepsilon_a = \varepsilon_{ae} + \varepsilon_{ap} = \frac{\sigma'_f}{E} \left(2N\right)^b + \varepsilon'_f \cdot (2N)^c \tag{4.4}$$

Graphical expression of Equation 4.4 is shown in Figure 4.3. In logarithmic scale, both contributions, elastic and plastic, are represented by linear functions with slopes b and c, respectively.

4.2 Fatigue design philosophies

Ideal part would withstand an infinite number of cycles. Despite this state is possible in some cases, vast majority of constructions are designed in area of low cycle fatigue. The infinite life concept means that fatigue limit of the material can not be crossed in any part of the

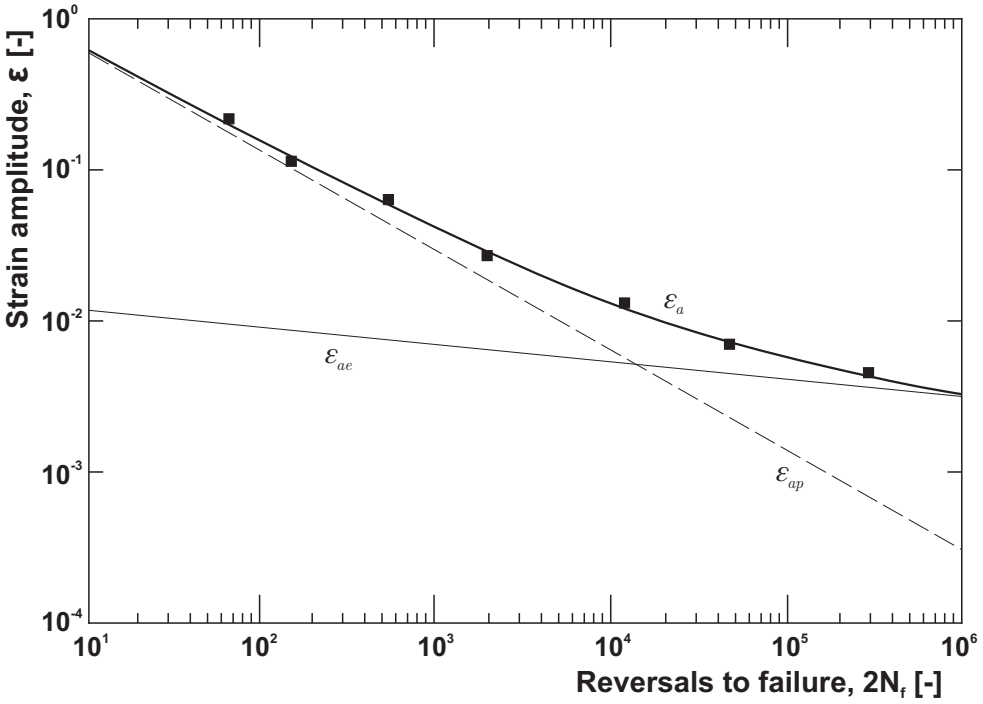

Figure 4.3: ε-N curve

construction, which would lead to need of high safety factors and robust constructions. This state is not acceptable especially from the economical point of view. As mentioned before, most of the structures are constructed in the area of limited life. There are three basic design philosophies, i.e. *Safe life*, *Fail safe* and *Damage tolerance*.

4.2.1 Safe life

This design philosophy is based on the idea that fatigue failure is not allowed during proposed life of the part or structure. Safe life approach is usually adopted by ground vehicle industry. Parts are designed with corresponding safety factors and after a prescribed life is reached the part should by replaced even in the case that no visible damage is present.

4.2.2 Fail safe

In particular, fail safe philosophy is aimed to the safety of the whole construction. While a failure of its particular part is allowed, it must not influence performance its overall functionality until repairs can be made.

4.2.3 Damage tolerance

Last philosophy can be marked as a middle ground between the two previous ones. It relies on the idea that cracks and failure of minor parts are present but thanks to knowledge of the crack propagation behaviour and periodic inspection, the structure can be operated with very low probability of catastrophic failure. Damage tolerance approach is often used in aerospace industry because it leads to the lightest possible structures with preservation of safe functionality.

4.3 Palmgren-Miner rule

Palmgren-Miner (P-M) rule is based on the idea of cumulative fatigue damage. The principle of the method is that each cycle contributes its part D_i to overall damage of the material. As soon as the latter quantity reaches a critical threshold $D = D_{cr}$, a fatigue failure occurs. Usually for design purposes, D_{cr} is assumed to be 1.

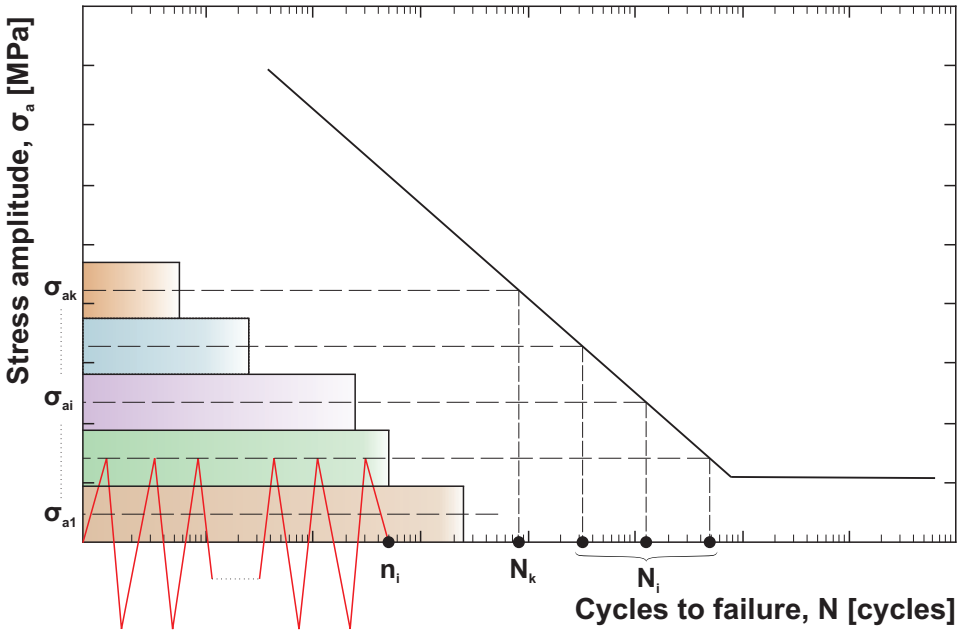

Figure 4.4: Principle of P-M damage summation

Despite the fact that there are numerous functions defining cumulative damage of material such as Haibach and Serensen-Kogajev, P-M rule still remains as one of the most commonly used methods for fatigue life prediction. Its main advantage lies in its simplicity, because overall damage is calculated as a sum of all the k minor contributions in following form:

$$D = \frac{n_1}{N_1} + \frac{n_2}{N_2} + ... + \frac{n_k}{N_k} = \sum_{i=1}^{k} \frac{n_i}{N_i} \tag{4.5}$$

The principle of P-M rule is shown in Figure 4.4 Each block of n_i cycles with constant amplitude is correlated with limit value N_i at the same stress level.

4.4 Fatigue life prediction

Together with deeper knowledge in the field of fatigue mechanics and with progress in stress-strain analysis using finite element method, it was possible to develop approaches for fatigue life prediction. Unfortunately, even the most present approaches are not able to cover all the conditions and mechanisms which contribute fatigue failure. Therefore, outcomes of these methods are somewhat limited.

The approach which is used later in this work is called Nominal Stress Approach (NSA). Historically, it is the oldest method for fatigue life estimation and it is also known as stress-life method. Standard input parameters and subsequent data processing are graphically shown in Figure 4.5.

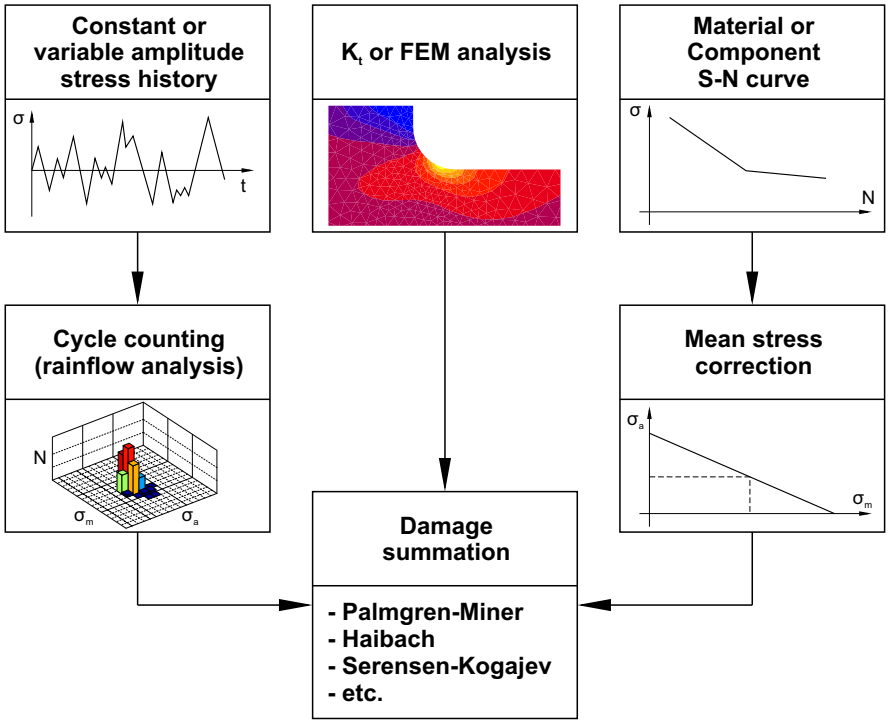

Figure 4.5: Fatigue life estimation using Nominal Stress Approach

As it can be seen in the Figure 4.5, the three inputs of this method are:

Input 1: Stress distribution data

First input deals with standard (usually static) FE analysis of the structure in order to obtain nominal stresses throughout the body. According to the nature of the problem, various stress combinations can be taken as input. The most commonly used are Equivalent Von Mises Stress and Principle Values of Stress.

Input 2: Loading history

Second input tells the solver how the stress results vary in time. In the case that the loading history is other than periodic with constant amplitude, the input signal has to be processed using some of the cycle counting methods. This process decomposes the signal to a set of cycles with given mean stress and amplitude and creates histogram of given load. In today's practice the most acknowledged method is called rainflow cycle counting. More details about this way of signal decomposition can be found in many publications such as [55] and [56].

Input 3: S-N curve of the material or component

Last input parameter is S-N curve of either material or the whole component. For the purpose of damage summation, raw S-N data are modified according to the current value of mean stress and amplitude of the cycle. Again, many methods were developed for this purpose, e.g. Goodman, Gerber and Soderberg line in Haigh diagram.

In present engineering practice, more and more attention is paid to local approaches instead of above described nominal stresses. Advantage of these methods is that they take into account plasticity which NSA ignores. As a consequence, these methods are suitable for evaluation of both high and low cycle fatigue whereas NSA should be used in HCF area only. The only drawback is that most of local approach methods require ε-N fatigue curve which database is considerably smaller in comparison with amount of S-N material data. One of the main representative of local approaches is Local Elastic-Plastic Strain and Stresses (LPSA) method, often marked as strain-life approach. Another approach, method of Local Elastic Stresses (LESA), exploits wide database of S-N curves yet it preserve advantages of local approach. More details about the methods for fatigue life estimation can be found in publication of M. Růžička et al. [57].

Chapter 5

Material tests of given NiTi Alloy

5.1 Chapter introduction

Purpose of this chapter is to analyse properties of the NiTi shape memory alloy used by ELLA-CS company to produce their stents. In order to do that, the processes which influence the stent during its life must be clarified in the first place. When taking into account possible load cases imposed on NiTiNOL endovascular stent-graft, i.e. loading into a catheter, its deployment in the blood vessel and following cyclic loading due to alteration of blood pressure and with regard to the facts discussed in Chapter 3, it must be stated that pseudoelastic effect of the material will play a crucial role. Although work of Kleinstreurer et al. [58] discusses use of shape memory effect for loading a stent-graft into a catheter and its deployment into the blood vessel, the most common way uses purely mechanical way to load the stent-graft. When implanted into an artery, stents are subjected to small, if any, changes of temperature and thus thermally induced martensitic transformation does not occur in the material.

5.1.1 Overview of performed tests

Because of the facts discussed above, first part of this chapter deals with determination of all the parameters needed to precise description of material's pseudoelastic behaviour. According to the list of standard tests given in publication of D.C. Lagoudas [32], three basic tests were carried out:

1) Spectral analysis

Spectral analysis reveals a percentage of the two basic metals - Nickel and Titanium - in given material. According to the literature, the composition influence NiTi's material parameters such as transformation temperatures very significantly. Y. Suzuki [31] states that one percent shift in Ni content causes a change of M_s point by 100 °C. Results of the test are also important to comparison of data from following tests with publications of other authors.

2) Differential scanning calorimetry

Second test which helps to map pseudoelastic behaviour of given NiTi alloy is Differential Scanning Calorimetry (DSC). In the case of shape memory alloys, results of the DSC test show transformation temperatures of the material under zero stress.

3) Tensile tests

Finally, tensile tests of the NiTi specimens were done under three different values of temperature. Not only does these tests shows the whole pseudoelastic cycle but all the transformation stress levels can be read. Results of tensile tests have also their importance to determination of constants for the material model used for FEM analysis in chapter 6.

Last and the most time consuming part of this chapter deals with evaluation of fatigue properties of the material. The goal is to obtain consistent data for construction of S-N curve of given material. This stress amplitude vs. number of cycles to failure dependency is crucial for further work and reliable data are not available in the literature as it was described in Section 3.5.1.

5.1.2 NiTiNOL specimens

Concerning the specimens themselves, ELLA-CS provided us with NiTi wires which they use for making of stents (Figure 5.1 a). Before any of the tests were carried out, the specimens were thermally treated in a the same way that the resulting stents are.

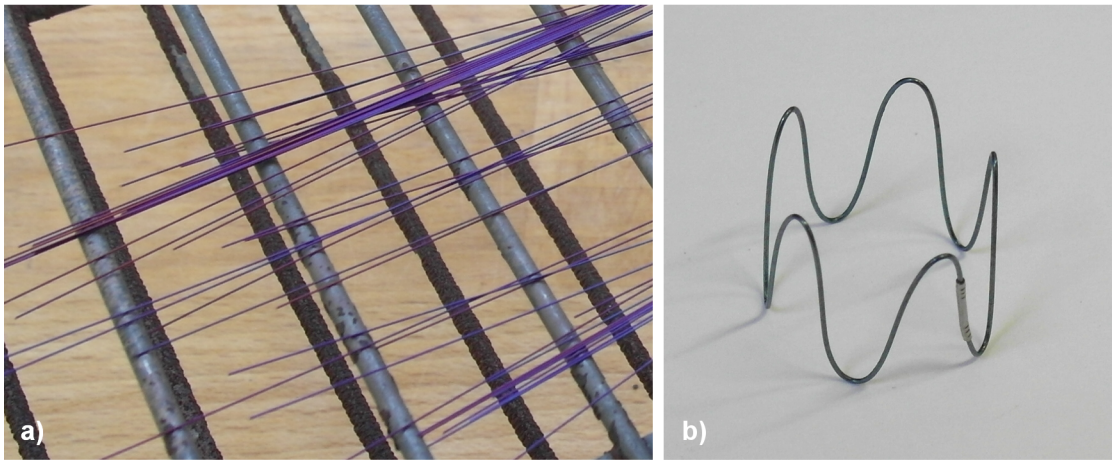

Figure 5.1: NiTi specimens
a) 0.18 mm wires (after heat treatment); **b)** stent made of 0.35 mm thick wire

The heat treatment procedure contains 5 minute annealing of the specimens at the temperature of 512 °C which corresponds to recovery annealing treatment under recrystallization temperature. The reason for this step is that under the room temperature, it is impossible to achieve such a shape of stent which is shown in Figure 5.1 b). Thus, the wire is mounted onto a special jig, composed of metallic pins over which the wire is bent. The following annealing process fixes this form.

The diameter of wire is 0.18 mm and first problem that had to be solved was to find a suitable clamping system for such a thin wire. Finding a solution lead to construction of special clamps, as described in following section.

5.2 Development of clamps

Although there are several solutions for clamping wires of various diameters, none of them was found suitable for our specimens. Most of the applications are meant for quasi-static tests hence their weight may cause a problem during accelerated fatigue tests.

For instance, INSTRON offers clamping system for fine cords and wires which is provided with pneumatic jaws (Figure 5.2). This solution reduces initial deformation of a specimen and preserves its rupture due to local stress concentration. Another solution solves tightening a wire by wrapping it around a cylindrical groove several times. Unfortunately, this solution is not very suitable for fatigue tests. Apart from the negatives described above, another limiting factor of commercially available solutions was, of course, their price.

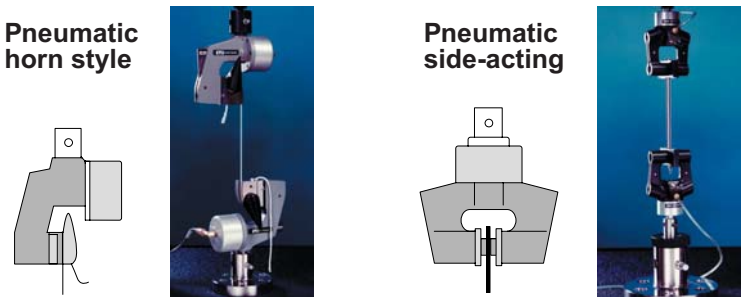

Figure 5.2: Commercially available clamps for fine cords and wires produced by INSTRON

For the purpose of performing tensile tests and following evaluation of material fatigue properties, special clamps were constructed. Their appearance can be seen in Figure 5.3 while complete documentation is enclosed in Appendix E. Main idea of these clamps is to avoid direct compression of wire specimen. To achieve this, a wire is guided over a cam of a circular shape and it is then fastened between two planar surfaces. As a consequence, stress concentration caused by tightening a wire do not influence overall results of tests.

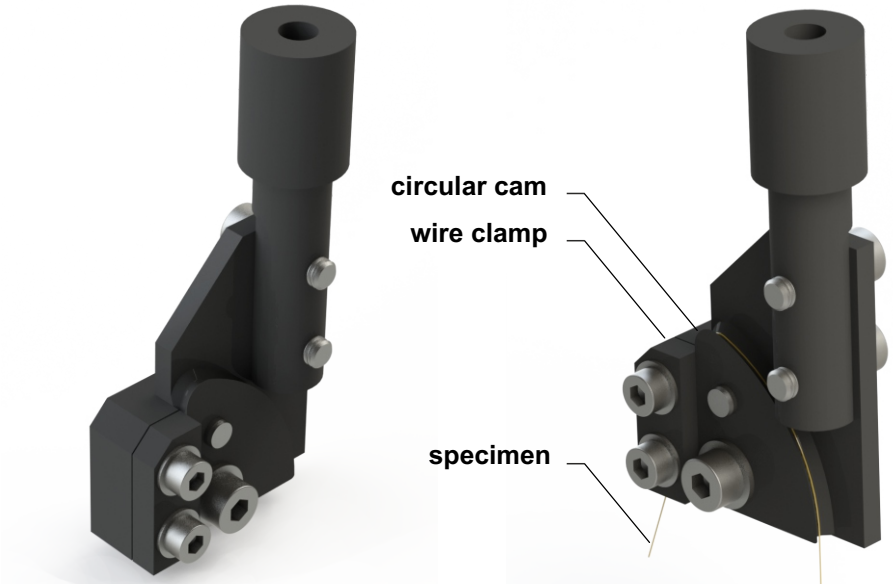

Figure 5.3: Special clamps for testing of fine wires

5.3 Composition of given material

Nowadays, there are several possibilities to evaluate composition of a material and to precisely compute weight or atomic percentage of the basic components. Without any attempt to be exhaustive, Optical Emission Spectrometry, Inductively Coupled Plasma Atomic Emission Spectrometry, Atomic Absorption Spectrometry or X-ray Fluorescence Spectrometry can be listed from a long list of methods which are used today.

In our case, composition of the material was tested together with the examination of specimen's surface quality on scanning electron microscope (SEM). The test itself is called Energy-dispersive X-ray microanalysis (EDX) which is a complementary method for SEM. The procedure was performed at Université de Franche-Comté, Besançon, France during my internship in Laboratoire de Mécanique Appliquée. During the test, a specimen is exposed to beam of electrons which causes a generation of X-Rays within the material. Thanks to the fact, that the specific energy of these X-rays can be assigned to an element which emits them, it is possible to construct a histogram to measure these quantities.

The specimen was exposed to electron beam for 300 s and the graphical representation of the EDX analysis is shown in Figure 5.4. The material is composed of 53.78 at.% Ni and 46.22 at.% Ti without any other alloying elements. With this composition, the alloy does not fit into the wide group of the near-equiatomic binary NiTi Alloys as its Ni content is higher than 50.5 at.% Ni. According to the literature, near-equiatomic NiTi alloys does not show good pseudoelastic behaviour [31]. In the case of tested alloy, distinct pseudoelastic behaviour can be expected.

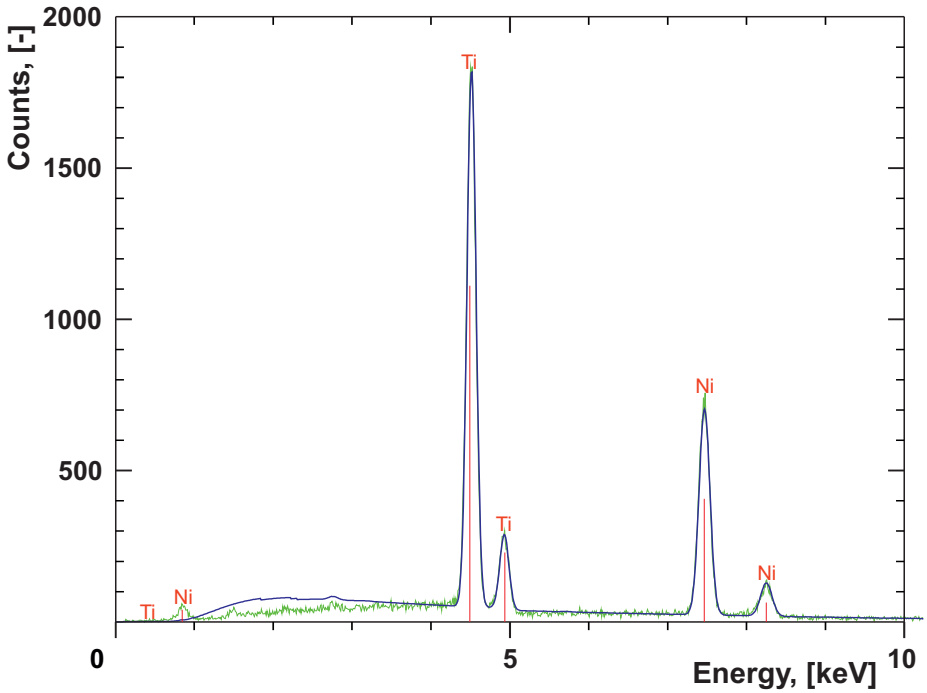

Figure 5.4: Histogram of the material evaluated using EDX analysis

5.4 DSC test

Differential Scanning Calorimetry (DSC) is a widely recognized thermoanalytical method used for evaluation of various temperature-dependent material parameters. It is valuable especially in the research of polymers for determination of glass transition temperatures, purity of a material, melting point and many others [59]. Details of use of DSC test for SMAs are described in ASTM Standard F2004 [60]. Thanks to this test, we are able assess transformation temperatures under zero stress as introduced in Section 5.1.1. This is possible due to the fact that forward phase transformation (from austenite to martensite) is an exothermic process. On the contrary, backward transformation is an endothermic process.

5.4.1 Principle of DSC test

Most commonly used power compensation differential scanning calorimeter is a device composed of two pans and a system for precise temperature control of these pans (Figure 5.5). One of the pans is dedicated for specimen and the other one for reference material. The reference is an inert material such as alumina, or just an empty aluminium pan. The temperature of both the sample and reference are increased at a constant rate and during this process, the difference in heat flow to the sample and a reference at the same temperature, is recorded as a function of temperature.

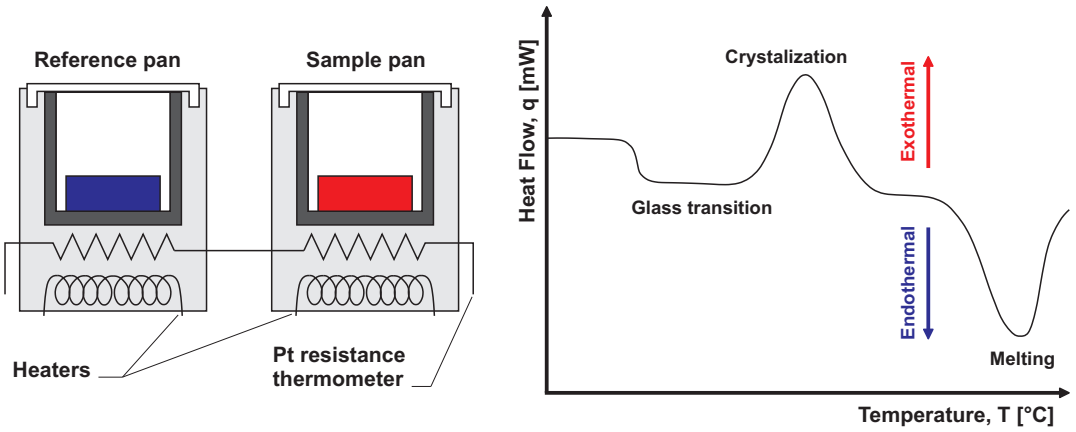

Figure 5.5: Diagram of DSC test and its typical resulting curve

When a sample undergoes a physical transformation such as a phase transition, more or less heat will need to flow to it than to the reference to maintain both at the same temperature. On the basis of the measured quantities, heat flow is calculated according to Equation 5.1 [61]:

$$q = \Delta p + \Delta T_0 \cdot \left(\frac{R_r - R_s}{R_r \cdot R_s} \right) - \frac{\Delta T}{R_r} + (C_r - C_s) \cdot \frac{\mathrm{d}T_s}{\mathrm{d}\tau} - C_r \cdot \frac{\mathrm{d}\Delta T}{\mathrm{d}\tau} \tag{5.1}$$

This equation has five terms. The first term is the difference in power supplied to the sample position versus the power supplied to the reference position. The second term accounts for differences between the thermal resistances of the sample and reference holders. The third term accounts for the heat flow that results from the difference in temperature between the sample and reference. The fourth term is the heat flow resulting from imbalances in thermal capacitance between the sample and reference holders. The fifth term reflects heat flow resulting from differences in heating rate between the sample and reference holders [61].

5.4.2 DSC test of given NiTi Alloy

Laboratory of Université de Franche-Comté is equipped with the TA Instruments Q100 Differential Scanning Calorimeter (Figure 5.6) which allows for property measurements on a broad variety of materials from -150 °C to 600 °C. Lowest temperatures are achievable with aid of liquid nitrogen. For the test itself, the wire specimen was cut into short pieces in order to fit into sample pan of the calorimeter. Overall weight of wire pieces was 11,04 mg. Temperature range of the test was set from -90 °C to 150 °C. This range was chosen according to the literature and it should cover transformation temperatures of most of the compositions of NiTi. Temperature rate of heating and cooling was 10 °C/min.

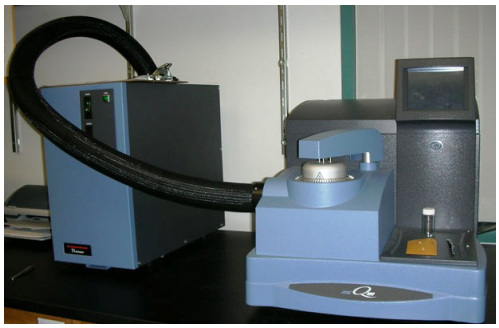

Figure 5.6: TA Instruments Q100 Differential Scanning Calorimeter

Result of the test is displayed in figure 5.7. One can clearly see the two peaks which are typical for a solid-solid phase transformation. In following post-processing part of the DSC test, the peaks were approximated by tangent lines. Then, a horizontal part of the curve was extended in order to intersect the lines created in previous step. These intersections defines the four desired transformation temperatures. Resulting values are as following: $M_s = -53.33\,^{\circ}\mathrm{C}$; $M_f = -72.66\,^{\circ}\mathrm{C}$; $A_s = 0.64\,^{\circ}\mathrm{C}$ and $A_f = 17.42\,^{\circ}\mathrm{C}$.

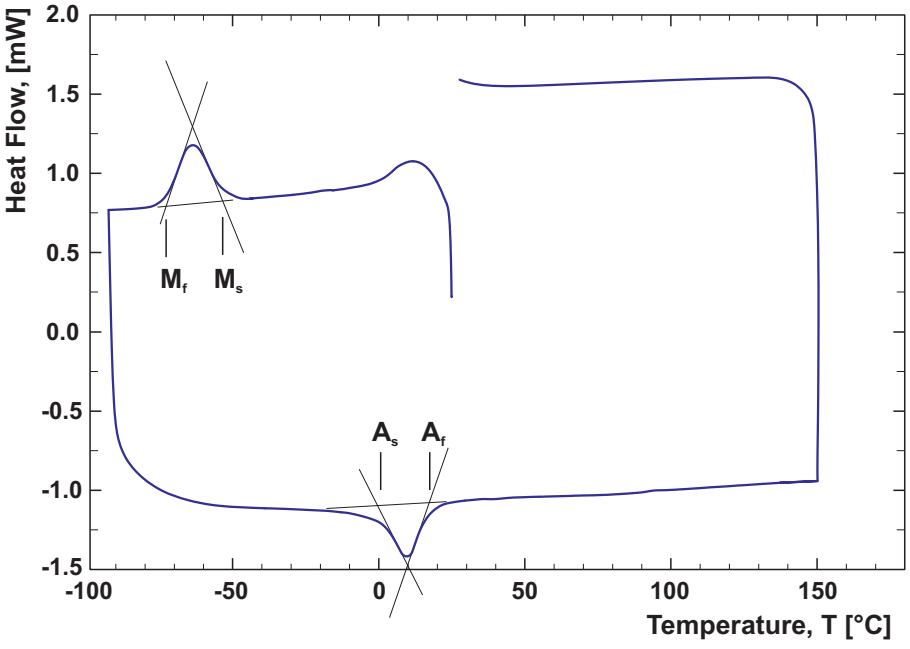

Figure 5.7: Results of the DSC test

5.5 Tensile tests

First natural step in establishment of material mechanical properties is to perform tensile tests. Thanks to these tests, we can evaluate several constants which define pseudoelastic cycle of given NiTi alloy. Unfortunately, we are able to do tensile tests only as compression tests are not possible in the case of wire specimens. This fact does not allow us to evaluate so called tension-compression asymmetry which is present in vast majority of NiTi alloys [62, 63].

5.5.1 Test equipment and method

Tests were done in the laboratory of Department of Applied Mechanics, Technical University of Liberec. Concerning the equipment, all the tests were carried out on Instron Electropuls E3000 testing machine (Figure 5.8) provided with ±1 kN dynamic load transducer (linearity and repeatability of the transducer better than ±0.25% of reading from 1% to 100% of load cell rating).

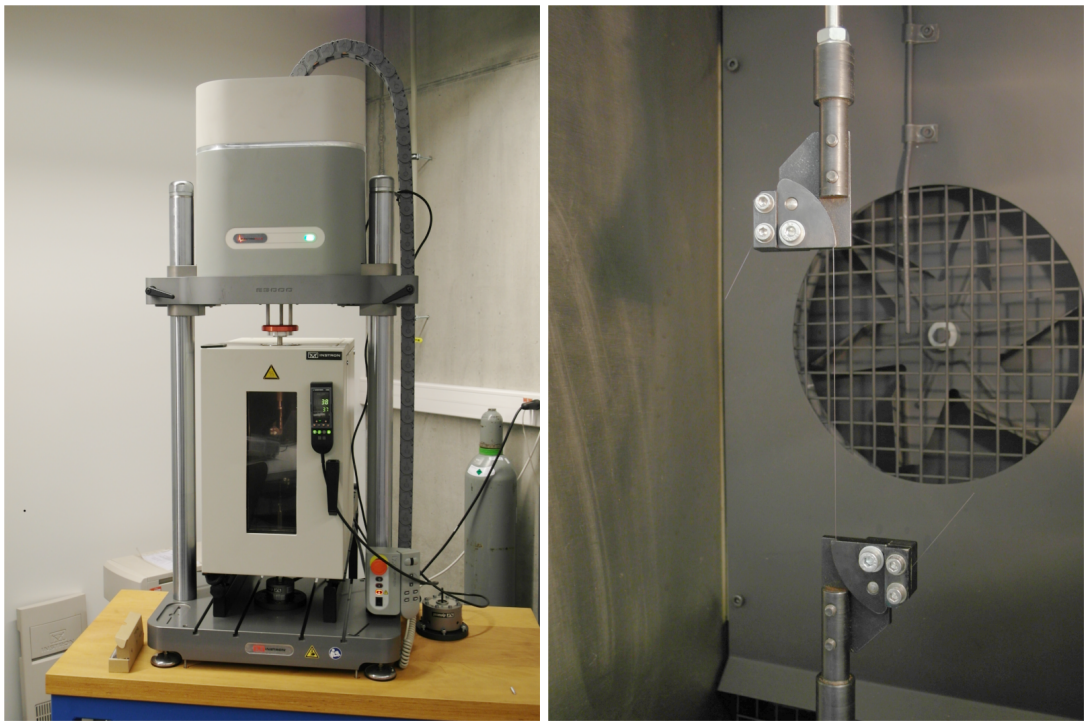

Figure 5.8: INSTRON Electropuls E3000 with Temperature Chamber

Wire specimen was fastened into the clamps which were introduced in Section 5.2. Active length of the specimen (distance between clamps) was 100 mm. The machine was driven under position control with load rate of 5 mm/min. During the test, a force response of the material

was recorded. As discussed in Chapter 3, transformation stress levels of NiTi are highly dependent on ambient temperature. Because of this fact and with respect to data needed for FEM simulations, tensile tests were performed under three different values of temperature, i.e. 20 °C (laboratory temperature), 37 °C (body temperature) and 60 °C. For this purpose, samples were tested using an optional testing equipment for the machine, the INSTRON SFL 3119-405 temperature control chamber (Figure 5.8).

Tensile tests were done in such a manner that the whole pseudoelastic behaviour of the material can be observed. Thus, initial experiment was performed until rupture of the material in order to obtain the two levels of stress at which martensitic transformation of the material begins and ends (σ^{Ms} and σ^{Mf}). Then, a sufficiently high strain at which a martensitic transformation is complete was chosen and following tests were carried out up until this strain only. After this selected threshold ($\varepsilon = 15\%$) was reached, a specimen was unloaded back to zero strain in order to evaluate stress levels of backward transformation (σ^{As} and σ^{Af}).

5.5.2 Tensile test results

Resulting tensile curves of the material in Engineering stress (σ) - Strain (ε) diagram are displayed in Figure 5.9. Pseudoelastic behaviour of the material is in accordance with the facts introduced in Section 3.3.

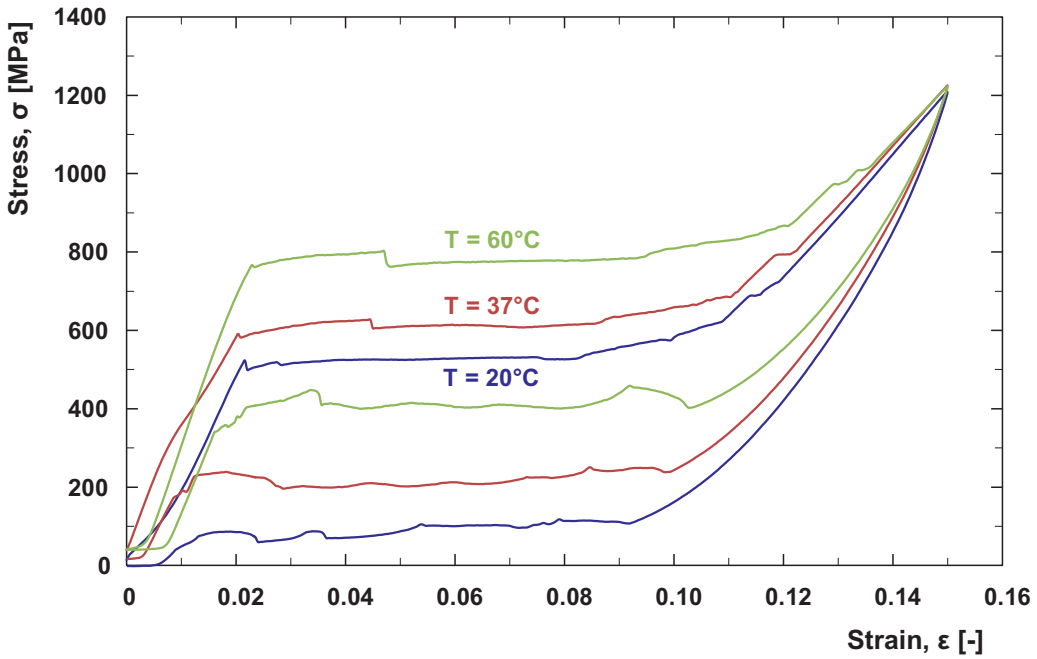

Figure 5.9: Tensile tests of given material under various temperatures

The cycle is characterized by closed hysteresis loop with clearly recognizable transformation stress levels. Another notable fact is that the values of transformation stresses rise together with raising values of testing temperature.

5.6 Derivation of material parameters

In this part, a data which were measured in previous section will be analysed with respect to definition of input parameters for SMA material models introduced in Section 3.6. For this purpose, a hysteresis loop will be characterized by seven constants, all of which are input values of Auricchio's mechanical model. In Figure 5.10, the method of constant derivation is depicted. The pseudoelastic cycle was fitted by piecewise linear function, according to the recommendation which can be found in publication of D. C. Lagoudas [32]. One can note that martensitic part of the loop is characterised by its unloading part.

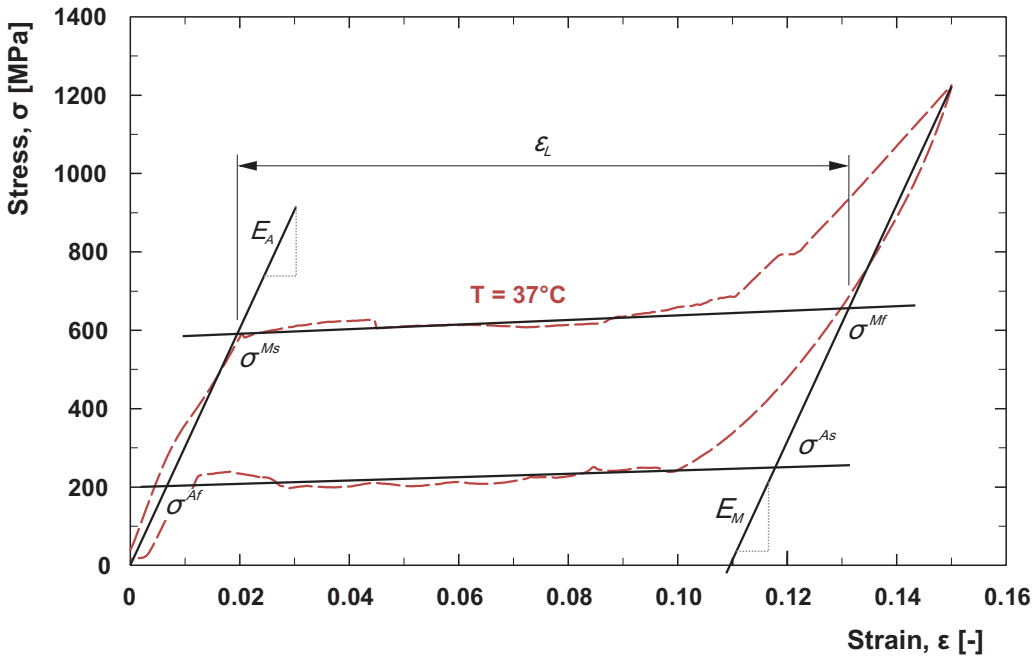

Figure 5.10: Linear approximation of pseudoelastic cycle and derivation of constants

Each intersection of above described linear approximations defines one transformation stress level. Another values obtained from this post-process is Young's modulus of both austenitic and martensitic phase. In the case of given NiTi alloy, the moduli E_A and E_M have the same value ($E_A = E_M = 30{,}190\,\mathrm{MPa}$). This state is not unique, similar or equal values of the moduli were published in several publications such as in Liu et al. [64]. Evaluated transformation stresses for the three tested temperatures are summarized in Table 5.1.

Table 5.1: Overview of tranformation stresses for given NiTi alloy

Temperature T [°C]	Transformation stresses			
	σ^{Ms} [MPa]	σ^{Mf} [MPa]	σ^{As} [MPa]	σ^{Af} [MPa]
20	507	573	117	70
37	592	657	250	203
60	769	834	435	388

5.7 Phase diagram of the material

As soon as both DSC test and analysis of tensile test curves are done, a phase diagram of the given NiTi Alloy can be constructed. This diagram is valuable especially for Saeedvafa's thermomechanical model because the diagram contains two of its input values. With use of linear functions, corresponding transformation levels are approximated and slopes of austenitic and martensitic parts are evaluated (Figure 5.11). Thanks to these functions, the model is capable to calculate any transformation stress level according to the temperature which is defined as an initial condition.

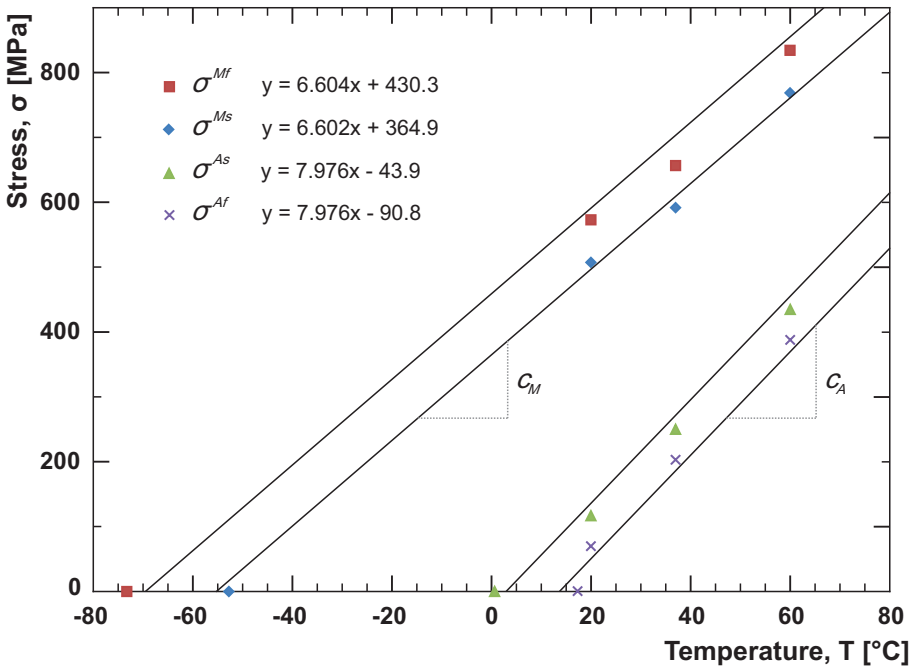

Figure 5.11: Phase diagram of given NiTi Alloy

5.8 Fatigue tests of NiTi wires

Last and most time consuming part of mechanical tests dealt with evaluation of material fatigue properties. As stated before, such a data are essential for further numerical fatigue analysis of a stent subjected to systolic pressure pulse.

First of all, we had to decide which type of fatigue curve will be evaluated to characterize fatigue properties of given NiTi shape memory alloy. With respect to aim of this work, i.e. cardiovascular stents, I consider a potential rupture of this device in an artery as the most life threatening event that can occur. In contrast with previous statement, initiation of a crack and its propagation does not seem to be essential quantities which should be evaluated. Moreover, stresses acting on stent after implantation into an artery can be expected not to even reach first transformation stress level σ^{Ms}. Thus, evaluation of stent's life is closely connected with high cycle fatigue region. On the basis of these facts, we decided to subject wire specimens to load driven cyclic tests in order to evaluate S-N fatigue curve.

5.8.1 Setup of fatigue tests

Fatigue tests were carried out on the same machine and with the same equipment as in the case of tensile tests (see Section 5.5). Keeping in mind that durability analysis of the stent is meant to be performed under conditions similar to human body, we had to take an influence of temperature into account. As it can be seen in results of tensile tests, even small change of temperature increases value of stress in the order of tens of megapascals. As a consequence, we decided to test and construct S-N curves under laboratory temperature (20°C) and body temperature (37°C).

After the specimen was clamped, a slight pretension of 0.1 N was applied. Considering form of the specimens, we could only choose from two types of cyclic loading, i.e. the one with zero R-ratio or the one with positive R-ratio. With respect to the pressure evolution in the aorta (see Figure 2.4) which lower value never reaches zero, we decided to carry out the experiments with constant value of cycle asymmetry of $R = 0.2$. Testing procedure itself was created in INSTRON WaveMatrix Dynamic Testing Software and it is composed of four parts (Figure 5.12).

Block 1 and 2 Quasistatic load and unload of the wire

As depicted in the figure, these two first blocks are carried out under position control. Generally, this step represents tensile test of the material with load rate of 50 mm/min up to 15% strain. Meaning of this first part is related with stabilisation of pseudoelastic cycle. Moreover, the step is also crucial for machine's control system which is then switched into force control.

Block 3 and 4 Ramp to setpoint and cycling of the specimen

Third block ensures force ramp to desired setpoint (mean load) of the cycle. The block is characterized by its duration of 10 s. Last step of the test starts cyclic loading with given amplitude and frequency.

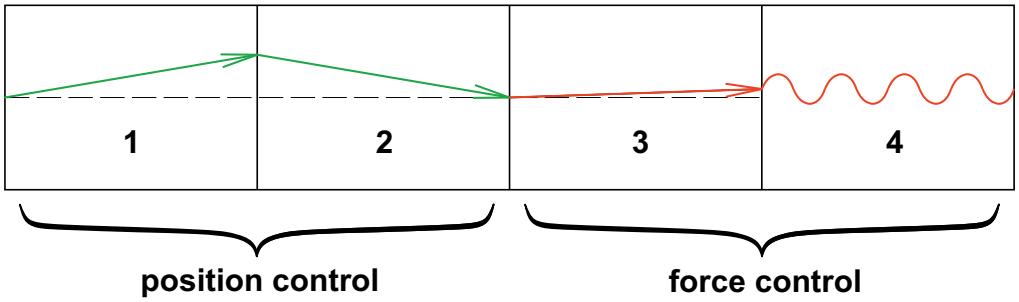

Figure 5.12: Block scheme of NiTi wire fatigue testing procedure

5.8.2 Fatigue tests remarks

With chosen loading cycle of $R = 0.2$ there were three possible regions in which the cycling of the specimen could have been performed. According to the maximal force of the cycle, these regions can be sorted as following:

1) Cycling in pure martensitic phase

In this case, peak value of the cycle is high enough to finish martensitic transformation. On the other hand, its bottom value never reaches a level needed to induce backward transformation. In the Figure 5.13, an evolution of hysteresis loop for a specimen tested at 37°C with peak value of engineering stress $\sigma_{max} = 690$ MPa is displayed. One can notice that stabilisation of hysteresis loop takes place after about 100 cycles. Shape of the loop is narrow and it does not change its form until failure of the specimen occurs. From the durability point of view, specimens cycled in this region withstand up to 4 000 cycles at maximum. Fracture surfaces expected after cyclic tests shows very rough structure with distinct traces of high applied stress (see Appendix A).

2) Cycling in pseudoelastic domain

Second testing region was the most hard one to work with. It is characterized by a setting which ensures crossing of all the four transformation levels. High reversible strains which accompany pseudoelastic behaviour of the material cause huge problems for machine's control system. This problem get even worse with rising value of testing frequency.

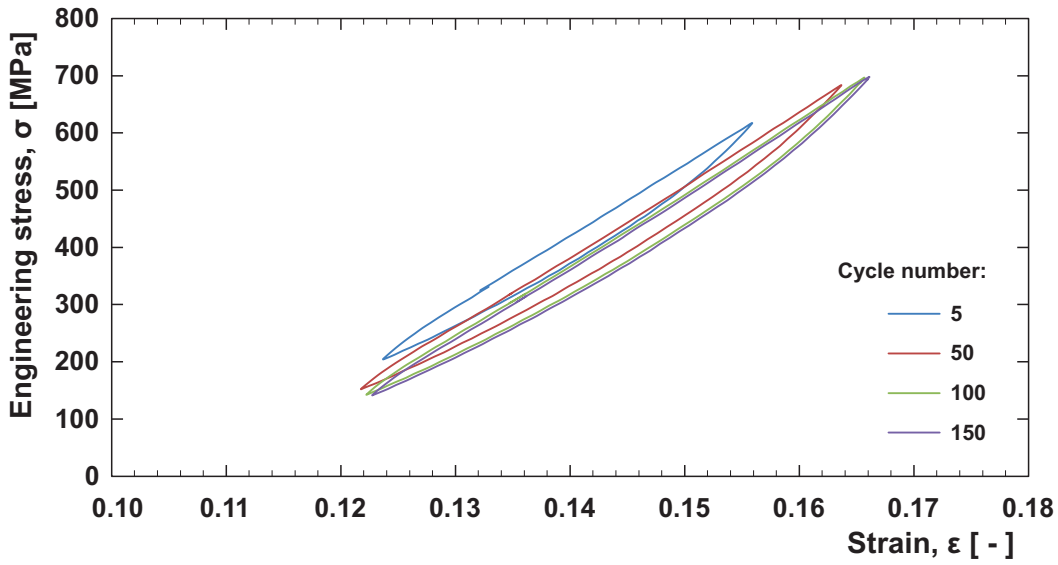

Figure 5.13: Evolution of hysteresis loop; NiTi wire cycled in pure martensitic phase; $\sigma_{max} = 690\,\mathrm{MPa}$

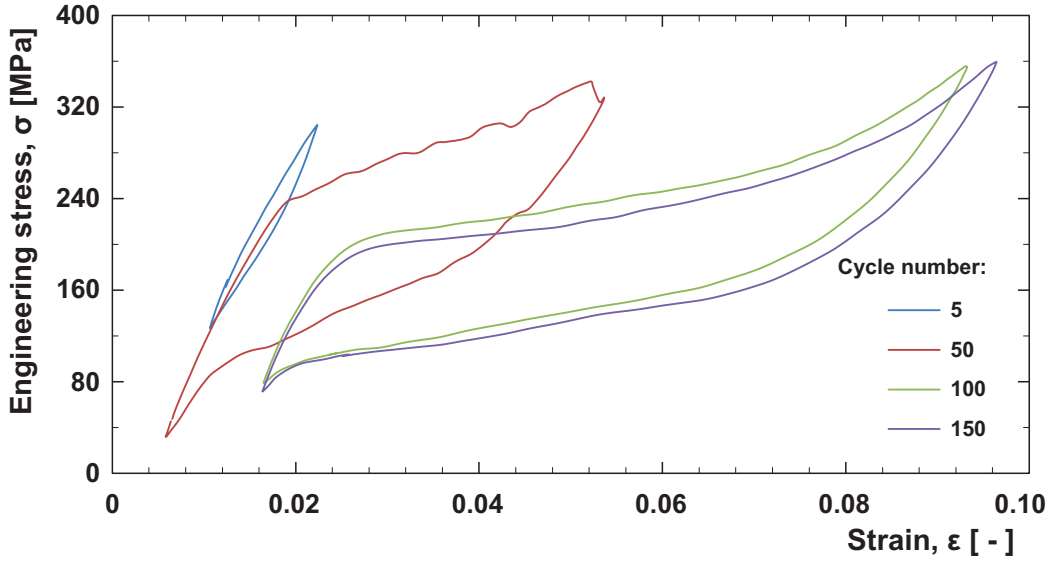

Figure 5.14: Evolution of hysteresis loop; NiTi wire cycled in pseudoelastic domain; $\sigma_{max} = 350\,\mathrm{MPa}$

Due to this fact, all the tests were carried out with frequency of 5 Hz. In the case that higher frequency was applied, life of the specimen got considerably shorter (Typically, 40% to 60% of life measured at 5 Hz). On the contrary, lowering the frequency did not change overall fatigue life of the specimen. In the Figure 5.14, typical evolution of the hysteresis loop during testing is shown. In this case, it took more than 150 cycles for the cycle to stabilize. Interesting fact is that even though peak values of force are notably lower than in the previous region, fatigue performance of the specimens tested in this region is similar to the previous one. This means that even in this region, fatigue life of the material does not breach a level of 5,000 cycles. This phenomenon causes a leap in resulting S-N data.

3) Cycling in pure austenitic phase

In the last testing region, maximal applied stress is lower than first transformation level. Therefore, cycling takes place in parent phase only. As it can be seen in Figure 5.15, it takes again more than 150 cycles before the resulting hysteresis loop stabilize. Considering the shape, its width remains constant and only height changes with increasing number of cycles. In comparison with two previous regions, no shifting of the curve to higher values of deformation occurs.

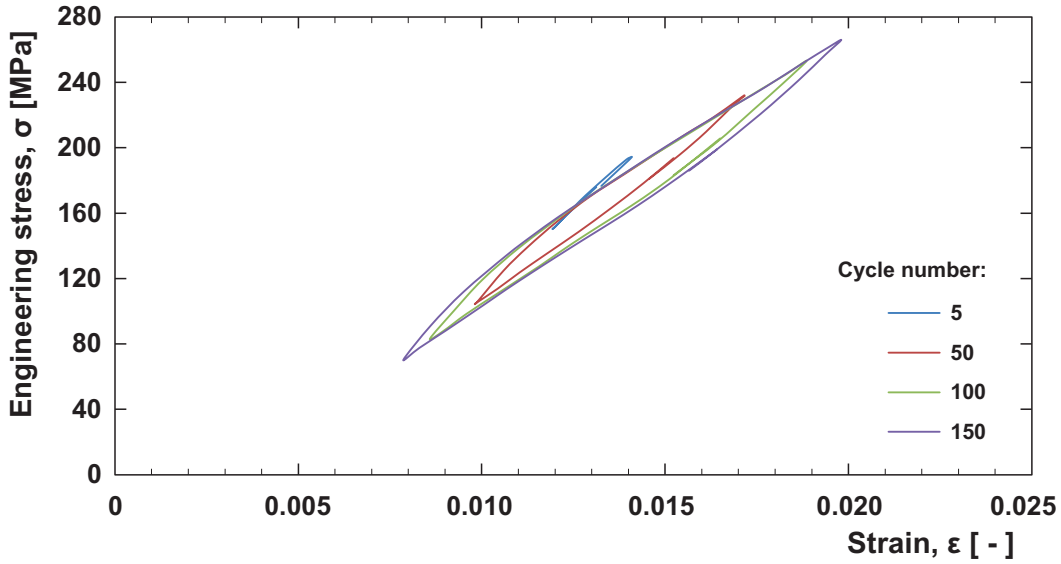

Figure 5.15: Evolution of hysteresis loop; NiTi wire cycled in pure austenitic phase; $\sigma_{max} = 270\,\mathrm{MPa}$

In general, specimens cycled in parent phase exhibit high fatigue life. With respect to data from fatigue tests, it can be stated that if the material was cycled in this region, it can achieve the endurance limit (10^7 cycles) without rupture.

5.8.3 Fatigue tests results

Complete data which arose from fatigue tests of NiTi wire specimens can be found in Appendix B. Resulting values of maximal value of stress vs. number of cycles until failure were fitted using following formula:

$$\sigma_{max} = SRI \cdot N^b \tag{5.2}$$

This relation is used by MSC.Fatigue software to enter material data into its database. *SRI* refers to stress range intercept and b is fatigue strength exponent. In fact, relation 5.2 is analogue of equation 4.2. Coefficients *SRI* and b were evaluated using linear regression.

Considering the remarks from previous part, the samples which were tested in either pure martensitic phase or in pseudoelastic regime shows very low fatigue life. Moreover, no major differences were found in fracture surfaces of the samples. Thus, all the data from these two regions were fitted by a curve which defines low cycle fatigue part of the S-N diagram. On the other hand, samples tested in pure austenitic phase shows no other than infinite fatigue life. This phenomenon was tested and verified up to the first transformation level. In this case, there is no other option than to define high cycle fatigue curve as a horizontal line which crosses corresponding stress limit. As a result, we obtain bilinear model for NiTi shape memory alloy.

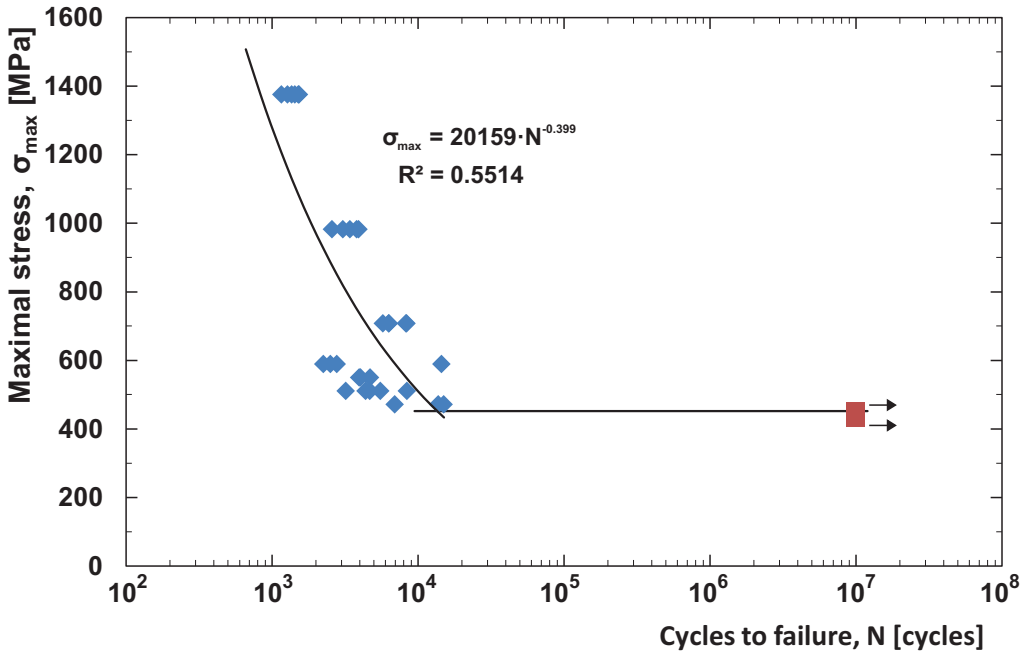

Figure 5.16: S-N curve for tested NiTi alloy; $T = 20°C$; $R = 0.2$

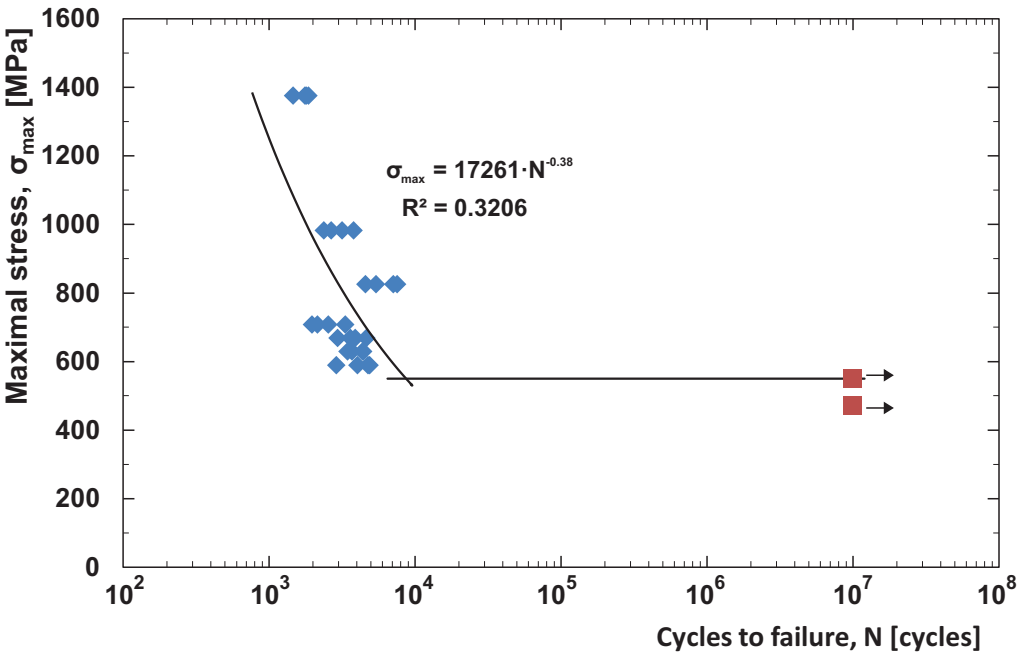

Figure 5.17: S-N curve for tested NiTi alloy; $T = 37°C$; $R = 0.2$

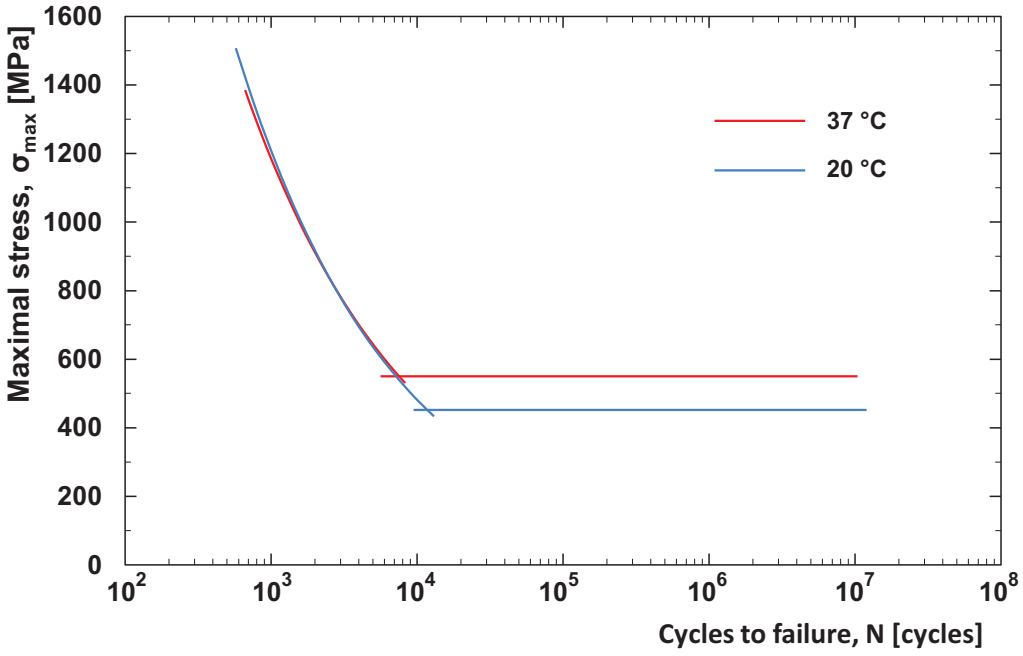

Figure 5.18: Comparison of NiTi alloy S-N curves evaluated for $T = 20°C$ and $T = 37°C$

In the Figures 5.16 and 5.17, resulting S-N curves are displayed for testing temperatures 20°C and 37°C, respectively. For the curve which refers to LCF region, its equation and coefficient of determination R^2 are shown. With respect to R^2 value, the fit is not very convenient. This fact can be mainly attributed to high scatter in data caused by leap in value of cycles until failure between test done in pure martensitic phase and pseudoelastic region.

Finally, Figure 5.18 shows comparison of the two above displayed S-N curves. It can be seen that the curves which describe low cycle fatigue region are in good agreement for both tested temperatures. On the other hand, high cycle fatigue curve rises with rising value of temperature. This fact was observed and discussed in fatigue tests remarks part and it can be attributed to shift of the martensite start stress level for higher testing temperature (see subsection 5.8.2).

5.9 Chapter summary

Thanks to the all the tests which were done in this chapter, wide range of material properties were evaluated for given NiTi alloy. Special aim was to determinate the parameters of material's pseudoelastic behaviour as it is assumed that this property of NiTi is mostly employed in the case of coronary stents. As stated in the introduction of this chapter, shape memory effect of the material is not used at all. Moreover, data evaluation of individual tests was aimed to obtain material constants for the material models introduced in Section 3.6. Experiments were carried out on specimens in the form of wire with 0,18 mm in diameter. Before testing itself, specimens were thermally treated according to the procedure used by the stent producer (see Section 5.1.2).

Firstly, EDX analysis as an optional part of SEM showed precise composition of the alloy. The material is composed of 53.78 at.% Ni and 46.22 at.% Ti without any other alloying elements.

Data from two following experiments were used to fully determine pseudoelastic effect of the material. Namely, DSC test and tensile tests done under three different ambient temperatures were used for this purpose. Results of the former test offered transformation temperatures of given alloy under stress-free conditions. Latter named tensile tests showed strong dependency of pseudoelastic cycle and its transformation stress levels on temperature. Subsequent analysis of the data outcomes several material constants such as Young's modulus of the both phases and transformation stress levels for corresponding temperature (see Table 5.1). Using the data gained from DSC analysis and tensile tests, it was possible to construct the phase diagram of the material (see Figure 5.11). For comparison, Huang et al. in their paper [65] evaluated influence of annealing at different temperatures for Ti–50.85Ni at.% alloy. From published stress-strain curves it can be evaluated that for 30 min annealing at 500°C, the value of martensite start transformation stress level is 350 MPa and the value of austenite

start stress level is 75 MPa. Considering the data published in this work, the shift in the data can be attributed to different composition of tested NiTi alloy. Moreover, annealing of our specimens was done for 5 min only.

Last part of this chapter was focused on determination of material fatigue properties, namely to construction of S-N curve. Due to high temperature dependency of material parameters, it was decided to perform fatigue tests under two values of temperature, i.e. 20°C and 37°C. Results show high scatter of the data, especially on the border between cycling in pure martensitic phase and pseudoelastic region. Important finding was that as long as the specimen is cycled in pure austenitic phase, the material withstands the endurance limit of 10^7 cycles without rupture. Therefore, first transformation level σ^{Ms} can be considered as material's fatigue limit.

Chapter 6

FEM analysis

6.1 Chapter introduction

Since its first practical use in the mid 1950s, the finite element method has become the essential computational tool in solid and structural mechanics. What is more, its application is much wider nowadays, containing a possibility to deal with multiphysics engineering problems such as thermal, electric and magnetic analyses. In the time of its greatest grow, FEM was also marked as a method which will completely abolish a need to perform any experimental measurements. Today's experience is, of course, different - when considering all the inputs which influence final result of FEM analysis, experiments still have their importance in verification and correlation of results.

6.1.1 Overview of performed simulations

In order to perform reliable analyses, first part of this chapter deals with verification of SMA material models which were mentioned in Chapter 3. Results of two experiments are compared with results of their simulation using FEM. On the basis of this comparison, one of the models is then selected for further work. Main goal of this chapter is a complex stress-strain analysis of stents which would otherwise be hard to evaluate experimentally. All the possible load cases will be taken into account and examined separately. Thus, practical part of this chapter deals with three areas of interest:

1. Loading a stent into a 24 F (1F $\doteq$ 0,33 mm) outer diameter catheter
2. Expansion of the stent in an artery
3. Cyclic loading due to evolution of blood pressure

First two load cases are possible to solve via standard structural analysis. On the other hand, to evaluate an influence of mechanical cyclic loading, durability analysis of the stent

must be performed. As mentioned in Chapter 3, all the simulations will be performed in MSC.Software products, namely MSC.Marc/Mentat in the case of structural simulations and MSC.Fatigue in the case of durability analysis.

6.2 Verification of material model

First of the two tests which should verify Auricchio's and Saeedvafa & Assaro's SMA material models and their constants, evaluated in previous chapter, is a simulation of tensile tests. Second test which will be carried out is so called "crush test" of the stent. This test is recommended by Center for Devices and Radilogical Health which belongs under Food and Drug Administration of the U.S.A. According to the document [66], its significance lies in the fact that peripheral stents in some anatomic locations may experience external, non-cardiac, focal, or distributed loads. These loads could cause stent deformation and, possibly, adverse clinical consequences.

6.2.1 Tensile test

From the computational point of view, the easiest way to simulate a tensile test is to define it as a 1-D job with use of beam elements. Unfortunately, this is only possible in the case of Saeedvafa & Assaro thermomechanical model as Auricchio model is not applicable to beam elements. Thus the simulation, in which Auricchio mechanical model is used, will be defined as a 3-D structural analysis. Model of wire is characterised either by linear hexahedron elements or by beam elements for mechanical and thermomechanical model, respectively (Figure 6.1).

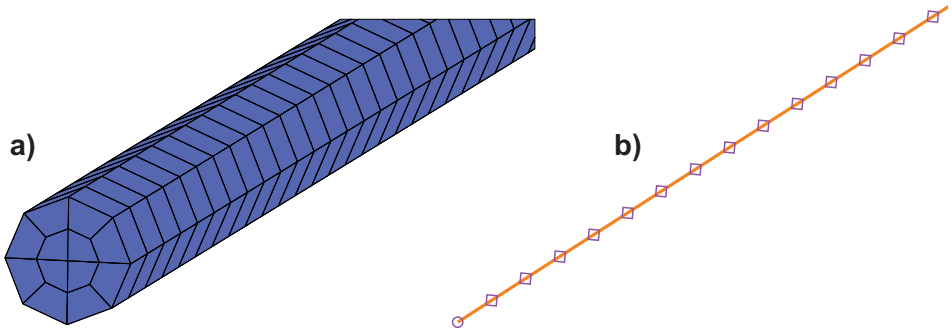

Figure 6.1: Models of 0.18 mm thick NiTi wire
a) solid; **b)** beam

Boundary conditions for both of the approaches were set equally. For the nodes (or one node in case of beam elements) on first end of the model, the displacements in each direction were set to zero. For the nodes on the opposite side of the wire, an axial displacement of 15 mm was prescribed, same as it was set in experimental tensile tests. Apart from boundary

conditions, a testing temperature was prescribed as an initial condition in the case of thermomechanical model for precise evaluation of transformation stresses. Most of the values for material models were evaluated in Chapter 5. Nevertheless, all of the material constants used in following studies are summarized in Table 6.1.

Table 6.1: Material constants of SMA models

Common properties			
Group	Quantity	Nomenclature	Value
Austenitic phase	Young's modulus	E_A	30,190 MPa
	Poisson's ratio	ν_A	0.33
Martensitic phase	Young's modulus	E_M	30,190 MPa
	Poisson's ratio	ν_M	0.33
Auricchio mechanical model			
Group	Quantity	Nomenclature	Value
Phase transformation stresses	Martensite start	σ^{Ms}	According to testing temperature (see Table 5.1)
	Martesite finish	σ^{Mf}	
	Austenite start	σ^{As}	
	Austenite finish	σ^{Af}	
Control parameters	Plateau length	ε_{psl}	0.122
Saeedvafa thermomechanical model			
Group	Quantity	Nomenclature	Value
A to M transformation parameters	M start temperature	M_s	-55.3°C
	M finish temperature	M_f	-65.2°C
	Slope	c_M	6.6 MPa/°C
M to A transformation parameters	A start temperature	A_s	5.5°C
	A finish temperature	A_f	11.4°C
	Slope	c_A	7.98 MPa/°C
Transformation strains	Deviatoric	ε^T_{eq}	0.11
	Volumetric	ε^T_V	0
	Twinning Stress	σ^g_{eff}	100 MPa
	Constants of g-function	g_a	-4
		g_b	2
		g_c	0
		g_e	0
		g_0	1,000

Jobs were submitted with variable time step while the displacement was released gradually with each time step up until its peak value. After completion of the simulation, a history plot of Equivalent Von Mises Stress vs. Displacement of the node at loaded end of the specimen was plotted. Results of simulations and their comparison with experiments for testing temperature 37 °C are depicted in Figure 6.2. Results for other tested temperatures are enclosed in Appendix C.

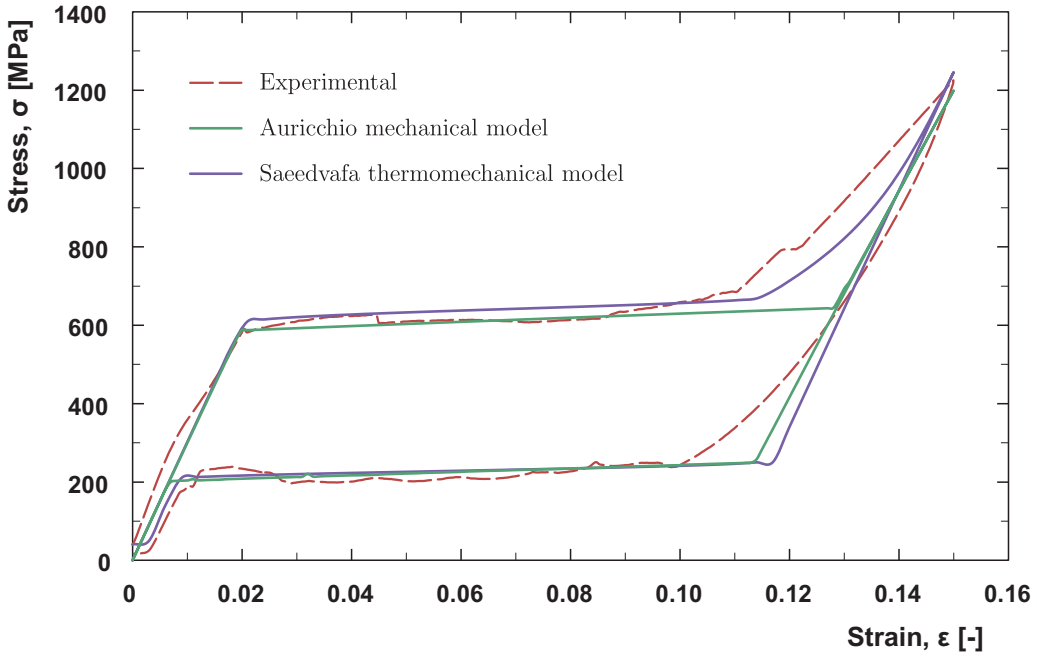

Figure 6.2: Experimental and numerical tensile test data of given NiTi alloy; $T = 37°C$

In the Figure 6.2, a good agreement between experimental and numerical results can be seen. In most of the pseudoelastic cycle, the two models behave similarly, i.e. composing the pseudoelastic cycle with piecewise linear function. Single exception is the end of martensite formation where results of Saeedvafa's model follow experimental data more conveniently.

6.2.2 Crush test

Due to the fact that all the tests of stents, proposed in document [66] (see introduction in section 6.2), are in the form of recommendations, precise description of crush test is not available. Nevertheless, the goal of this test is to evaluate a force which induce a permanent deformation of the stent. For our purpose, crush test will be carried out in such a way that the stent will be compressed between two parallel planes and force response will be recorded. Tested stent, made of 0,35 mm thick NiTi wire, was introduced in Section 5.1.2. Its outer diameter is 15 mm with height of 12 mm and it is formed of five similar threads. Concerning

its practical use, this type of stent can be found in bifurcated stent-grafts and it fits into common iliac artery.

Experimental part of the test was carried out in the laboratory at Department of Applied Mechanics, Technical University of Liberec. Resulting peak value of force during crush test was expected to be very low, hence a ±100 N load cell was used (HBM type S2, accuracy class: 0.05, linearity deviation: 0.05%). Specimen was placed on round compression plate of TIRA test 2810 tensile testing machine. Upper pusher was lowered into contact with stent and as soon as the change in value of force was registered, position counter was set to zero. Subsequently, the test itself was performed. Machine was driven under position control with load rate of 5 mm/min up to displacement of 12 mm from initial position (Figure 6.3).

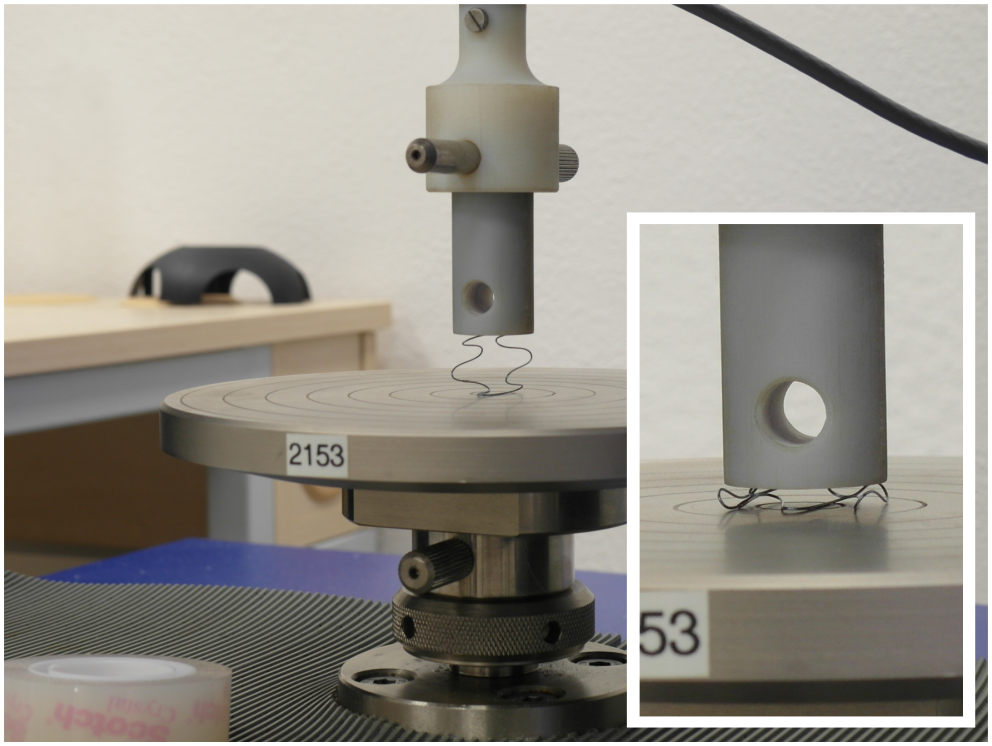

Figure 6.3: Crush test of NiTi stent: experiment

After the experimental part of the test was done, the whole procedure was simulated using FEM software MSC.Marc/Mentat in version 2014.0.0. First step was creation of stent CAD model in Autodesk Inventor 2014. Definition points of one thread were measured from physical model of the stent using digital calliper. Then, 3D spline was lead through these definition points while precise continuity was ensured by defining tangent relation to following threads. Finally, volume model was created by sweeping a circular profile along previously modelled path and subsequent circular array outcomes the whole model of the stent.

Numerical model of the stent is represented by 35,380 eight-node hexahedron elements (Figure 6.4). FE model itself was created in SIEMENS Femap preprocessor on the basis of stent CAD data. Compression plates are represented by two rigid planes, lower of which is fixed during the analysis. On the contrary, constant displacement rate in Y-axis direction is prescribed for upper plane according to actual time of simulation. Between the two rigid planes and FE model of the stent, a geometric/deformable contact was defined. All the contact parameters such as separation stress and values related to contact detection were left in default settings. Friction coefficient between contact bodies was not considered.

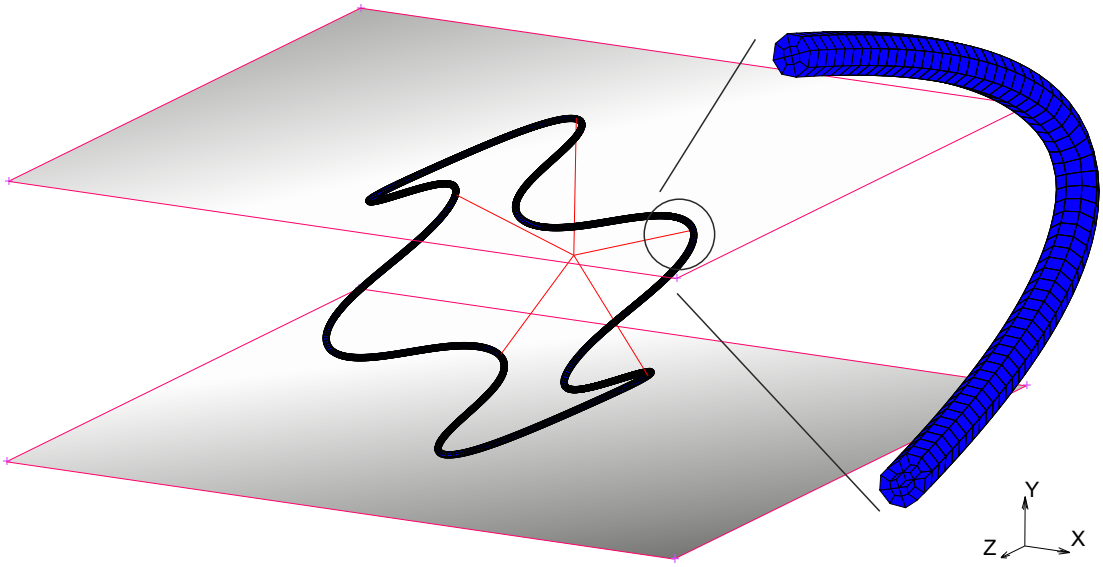

Figure 6.4: Crush test of NiTi stent: FE model

To ensure the right position of the stent during analysis, a numerical stabilization was used. This was possible thanks to dedicated links which behave as springs with very low value of stiffness (concretely, 10^{-6} N/mm). These links were set to tie a node in the top part of each thread of the stent to a ground point which is stationary during a job. In our case, the ground point forms centre of the circle which connects all the tied nodes (Figure 6.4). Six links are needed to influence a displacement in each direction and a rotation around each axis as only one degree of freedom is possible to prescribe for one link. Thus, thirty links were used to stabilize the whole model.

Resulting shape of the stent after successful completion of simulation is shown in Figure 6.5. When comparing the peak value of Equivalent Von Mises Stress (357 MPa) with tensile test curve at 20°C it can be stated that the stress is not high enough to even start a process of martensitic transformation. This fact was also verified by the analysis itself as one of the evaluated scalars called Volume Fraction of Martensite can be displayed.

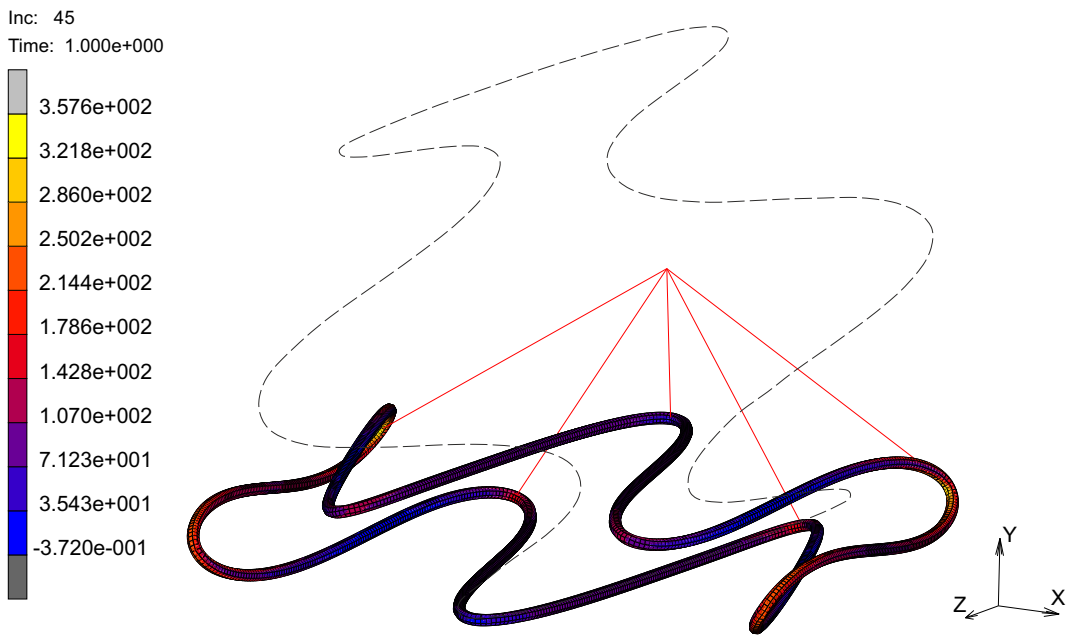

Figure 6.5: Crush test of NiTi stent: final configuration
Equivalent Von Mises Stress [MPa]

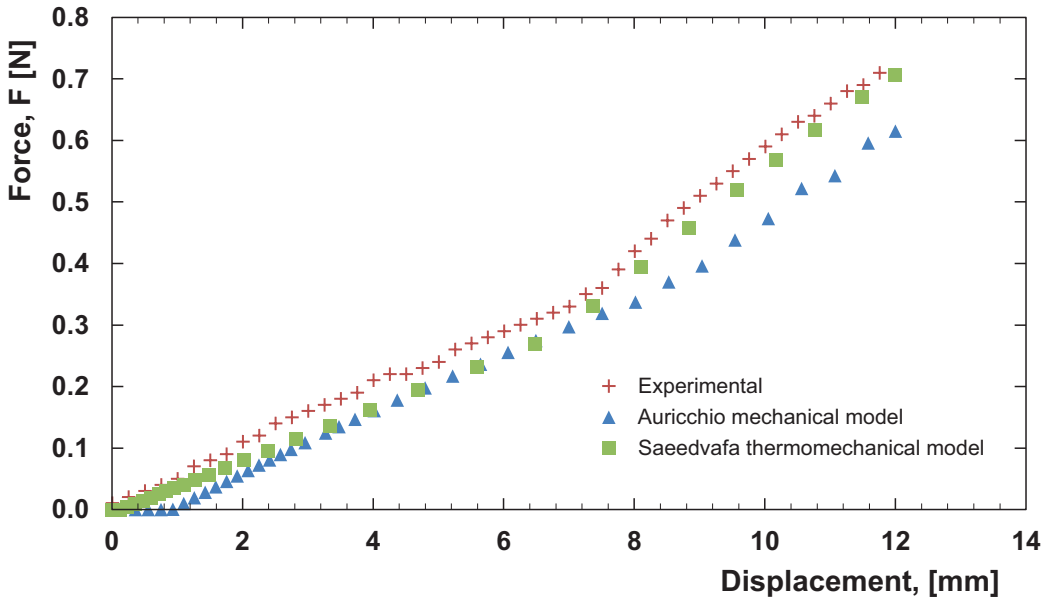

Figure 6.6: Crush test of NiTi stent: evolution of compression force

Nevertheless, main goal of the simulation was comparison with experimental data. For this purpose, history plot of Contact Normal Force versus Displacement of the upper plane was evaluated. Comparison of data evaluated experimentally and with use of finite element method is shown in Figure 6.6.

Similarly to simulation of tensile test, a good agreement between experimental and FEM data can be seen. The three curves show increase of stent's stiffness when it is subjected to compression of about 7.5 mm. At this point, typical turn of the characteristics is present. In the case of Auricchio's mechanical model, reaction force remains zero during first few iterations. This behaviour is probably caused by process of contact detection between affected bodies. As a conclusion of second verification test it can be stated that data of Saeedvafa model are again in better correlation with experimental data. This model will be therefore used for further work.

6.3 Loading a stent into catheter

During process of loading stent-graft into a catheter, stent must undergo large deformation. With respect to individual patient, common diameter of the stent which fits into abdominal aorta is about 27 mm. On the other hand, catheter which is used in this case study has inner diameter of 24 F (8 mm). In the case of stents which are made of surgical steel, the process of loading often cause their permanent deformation hence their implantation is often supplemented by expansion with use of inflatable balloon. As already told, NiTi stents are able to fully restore their given shape thanks to its unique properties.

Simulation of a loading should tell us how large stress is induced by stent compression and whether martensitic transformation is present. These parameters are important for a possibility of long time storing the stent-graft in catheter. This condition may occur during transport of the device to patient. Moreover, the data will be also used as input parameters for second simulation indicated in Section 6.1.1.

6.3.1 Simulation method

FEM model of the problem is depicted in Figure 6.7. It is composed of deformable body of the stent with diameter of 27 mm. This type was used with respect to the fact that it must undergo the largest deformation and thus highest values of stress can be expected. Stent is again characterized by eight-node hexahedron elements with amount of 35,856. Compression of the stent is realized thanks to rigid cylindrical surface. Between the two bodies a geometric/deformable contact was defined. Similarly to simulation of crush test, the model of stent is stabilized with use of links. Rigid body is prescribed to linearly decrease its diameter up to the final value of 8 mm with respect to to actual simulation time.

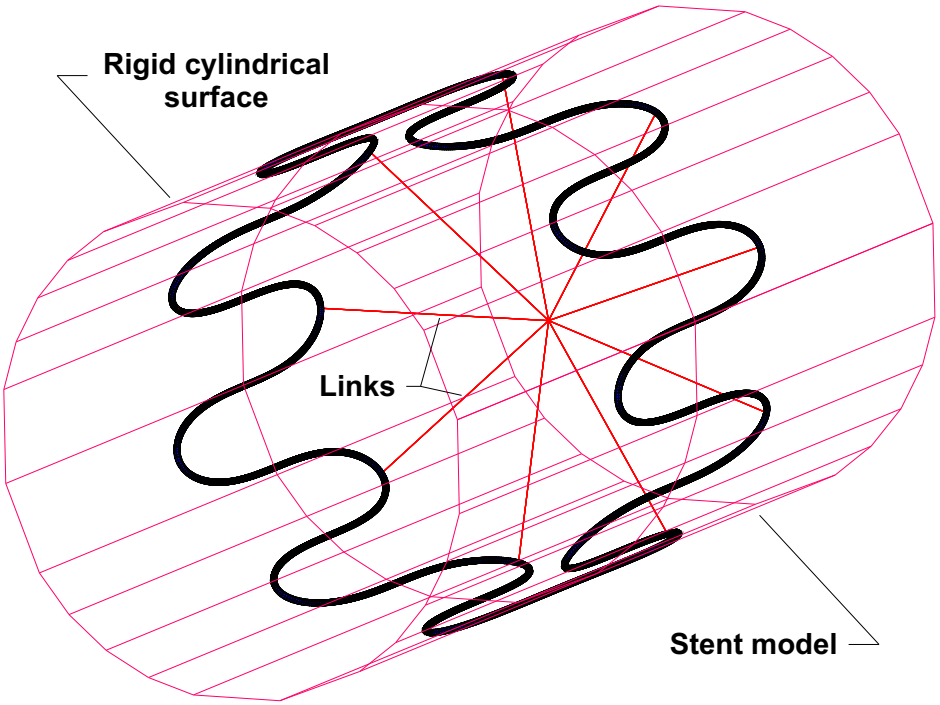

Figure 6.7: Loading a stent into catheter: FEM model

6.3.2 Results

In the Figure 6.8, the distribution of Equivalent Von Mises Stress throughout the stent is displayed at the end of simulation. According to the results, peak value of stress (420 MPa) occurs in bends of the stent.

Very interesting outcome of the simulation is that the material begins to transform from austenitic to martensitic phase. In the Figure 6.9, Von Mises Stress and Volume Fraction of Martensite in the most loaded area of the stent are displayed in more detail. Right hand picture clearly shows that this area undergoes martensitic transformation. In order to fully evaluate this phenomenon, evolution of the two values in most loaded node was plotted according to actual diameter of the cylindrical surface (Figure 6.10). Stress characteristic begins with slight rise until self contact of stent's threads occur at the diameter of 11.4 mm. From this point further, Von Mises Stress rises with much higher ratio. Another significant border occurs at diameter of 10.2 mm in which martensitic transformation begins. At this point, stress characteristic tends to decrease a little due to crossing of material's superelastic plateau region (see Section 3.3).

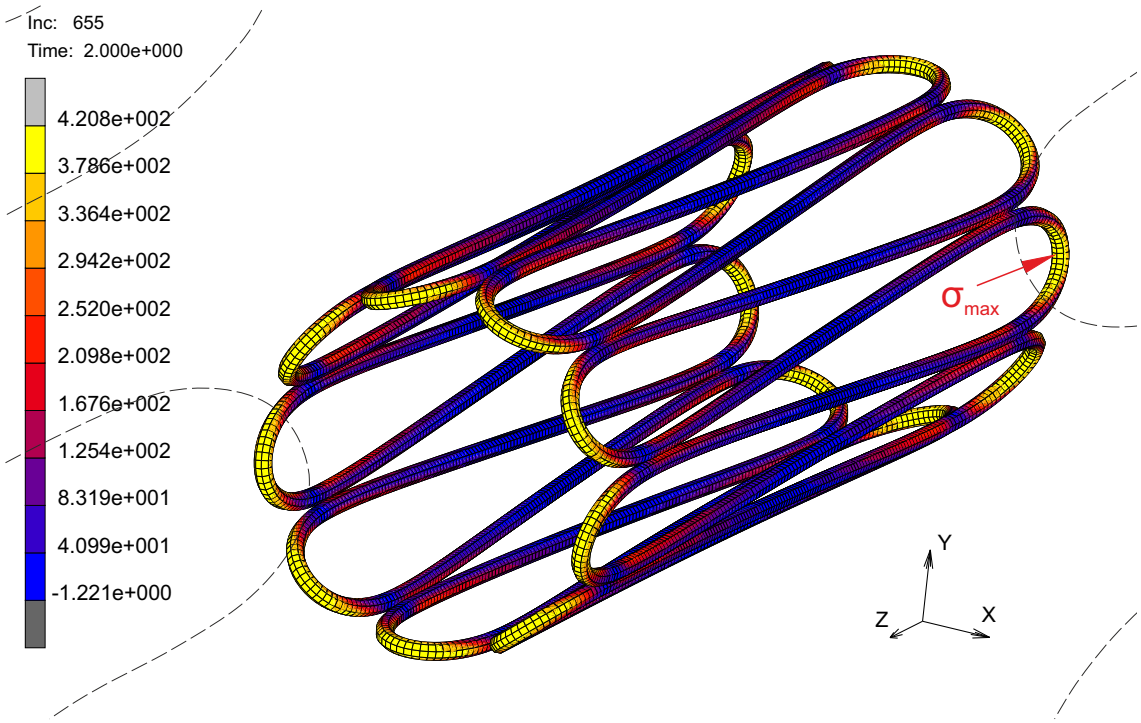

Figure 6.8: Loading a stent into catheter: final configuration
Equivalent Von Mises Stress [MPa]

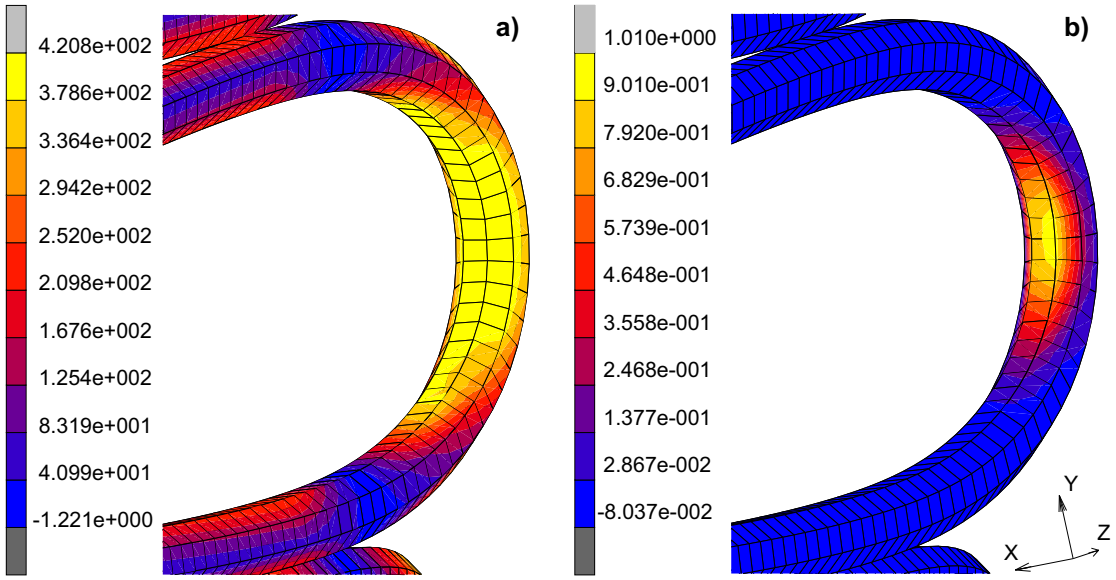

Figure 6.9: Loading a stent into catheter: detail of the most loaded area
a) Equivalent Von Mises Stress [MPa]; **b)** Volume Fraction of Martensite [-]

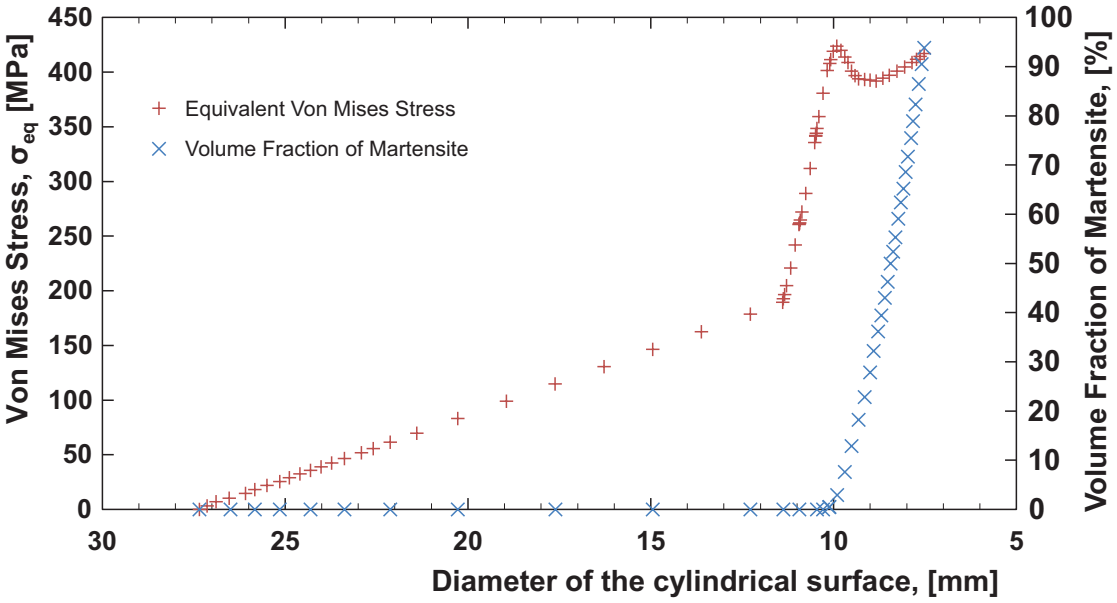

Figure 6.10: Loading a stent into catheter: stress evolution in the most loaded node

6.4 Stress distribution in stent during the cardiac cycle

Main goal of this section is to evaluate stress distribution in stent which is implanted into an aorta and subjected to shape change due to the systolic/diastolic pressure pulse. As introduced in Section 4.4, knowledge of stress distribution in cycled part is one of the three inputs needed for successful durability analysis of NiTi stent.

Formally, present simulation is an expansion of previous job. Stent and rigid cylindrical surface which is used to drive stent's diameter remain unchanged. The only feature which had to be added was a deformable body which represents aorta. For our purpose, the latter body is represented by a cylinder which is composed of 1,440 four-noded quadrilateral shell elements with constant thickness of 1.5 mm (Figure 6.11). Diameter of the cylinder is set to 19 mm. All the dimensions should represent proximal part of the aneurysm, i.e. the part which is not affected by aneurysmal dilatation but its mechanical properties might be influenced by the disease. When a stent-graft is introduced into blood vessel, this part of aorta is in direct contact with the device.

Boundary conditions of newly added aortic model were defined in such a manner that they should influence contact area with stent as least as possible. To achieve such conditions, displacements u_x, u_y and u_z of the nodes at both faces of aortic tubular structure were set to zero. Considering the length of aortic model 120 mm, stresses which are induced due to defined boundary conditions do not act in the area where stent interacts with aortic wall.

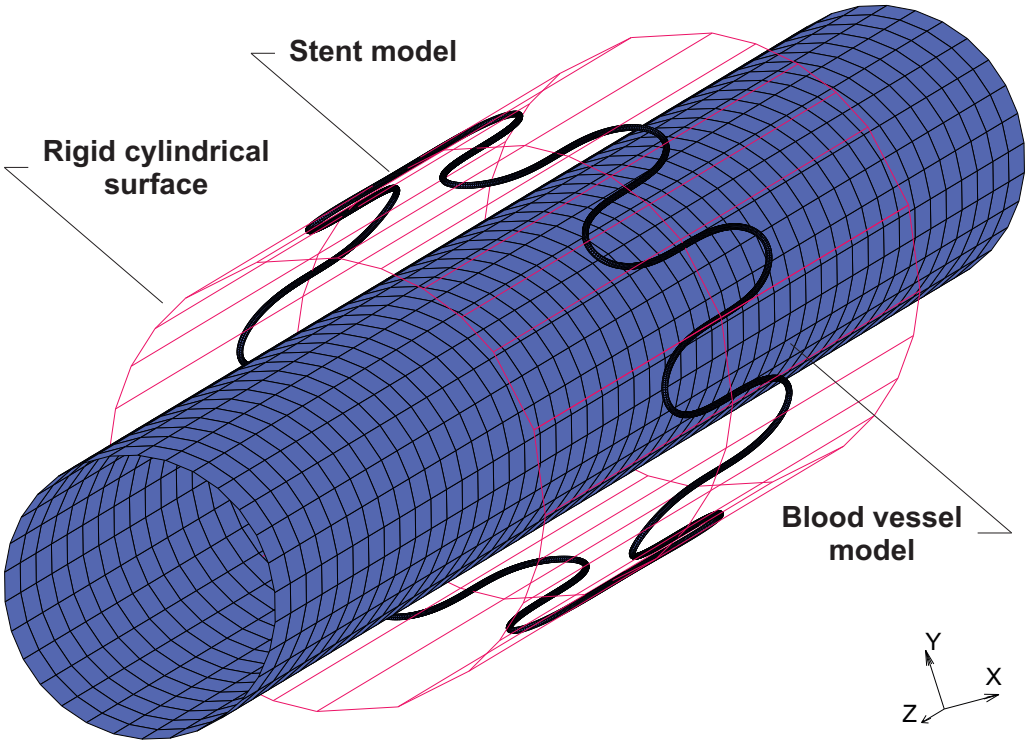

Figure 6.11: Numerical model of the study

6.4.1 Material model of aortic wall

In 1999, Raghavan et al. published a work which outcome was material model for AAA [67]. Proposed model is two parameter, hyperelastic, isotropic and incompressible. The two constants were evaluated using statistical tools according to mechanical tests of 69 freshly excised AAA specimens. Since the time of its publication, the model has become widely used and acknowledged. Originally, Raghavan model is defined as generalized power law neo-Hookean model with following notation of strain energy density function:

$$W = \alpha(\mathrm{I_B} - 3) + \beta(\mathrm{I_B} - 3)^2 \tag{6.1}$$

In Equation 6.1, $\mathrm{I_B}$ is the first invariant of Left Cauchy-Green tensor and α and β are above introduced model constants. In MSC.Marc software, the neo-Hookean material model is not included hence it was necessary to find a suitable replacement from available model database. In the work of Angelo et al. [68], Raghavan model was approximated with use of five parameter Mooney-Rivlin hyperelastic model. Results of this work were used also in our case as Mooney-Rivlin model is standard part of material database in MSC.Marc. For the model, following constants are defined:

$$c_{10} = \alpha \quad c_{01} = 0 \quad c_{20} = \beta \quad c_{11} = 0 \quad \text{and} \quad c_{02} = 0$$

Concerning material constants α and β, the mean values were chosen from statistical data available in the work of Raghavan et al. Thus, the two constant used in this study are as following:

$$\alpha = 17.4\,\mathrm{N/cm^2} \quad \beta = 188.1\,\mathrm{N/cm^2}$$

6.4.2 Simulation method

In order to obtain desired stress evolution in stent during the pressure pulse, it was firstly needed to maintain a contact between the stent and aorta. Therefore, the whole process was divided into three loadcases, each of which had different contact interaction defined between the three bodies which are present in this job.

Loadcase 1: Stent compression and application of diastolic pressure

In the first loadcase, diameter of the stent was reduced to a value smaller than inner diameter of artery model. This process was done using the same technique as it was used in previous section. In addition to squeezing a stent, a diastolic pressure of 75 mmHg was applied to aortic wall during this step. For this loadcase, the contact is defined between rigid surface and stent only.

Loadcase 2: Maintaining a contact with aortic wall

In the second loadcase, process of stent squeezing is reversed and diameter of cylindrical surface (together with the stent) is gradually enlarged. In this case, two types of contacts are defined, i.e. stent/surface and stent/aorta. At some point of the simulation, surface passes through the model of aorta hence the initial contact between stent and aorta is maintained. With rising simulation time, this contact stabilizes and stent remains fixed towards the aortic wall.

Loadcase 3: Application of blood pressure characteristics

Finally, the last loadcase should give us an answer on how the stress in stent changes during the pressure pulse. In this step, only stent/aorta contact remains active and pressure characteristics, introduced in Section 2.1.3 is imposed on aortic wall. Simulation time was set to 0.85 s with respect to real duration of one pulse.

6.4.3 Results

In the Figure 6.12, a stent configuration after execution of second loadcase is presented. In this display, model of the aorta was virtually expanded to defined thickness of 1.5 mm in order to clearly see a contact with stent.

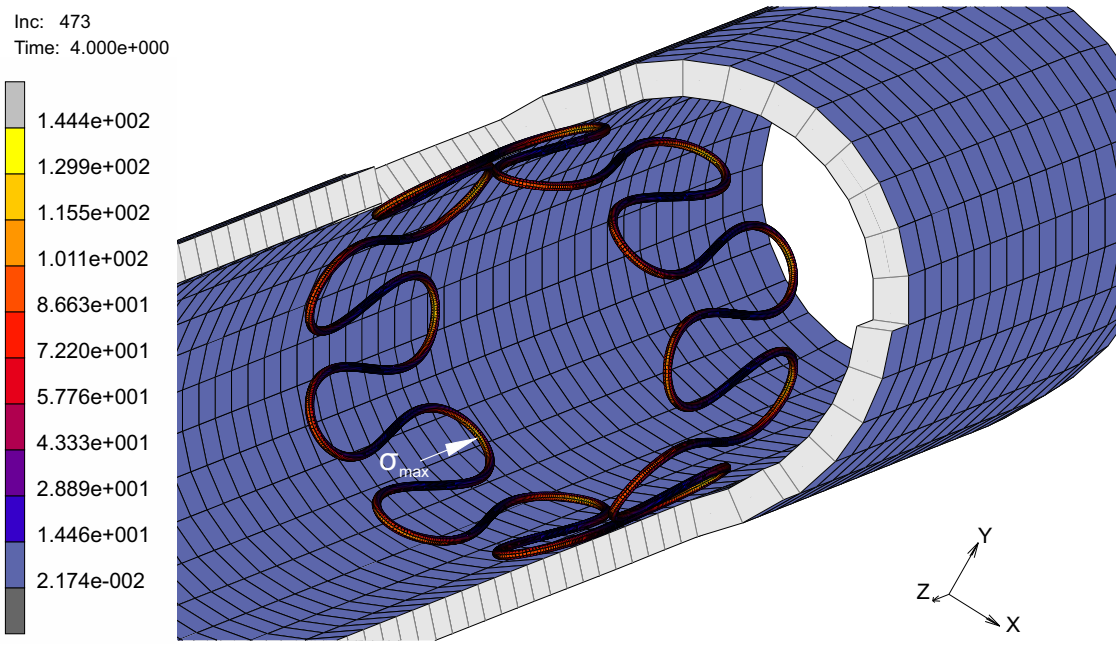

Figure 6.12: Stent in contact with aortic wall after execution of second loadcase
Equivalent Von Mises Stress [MPa]

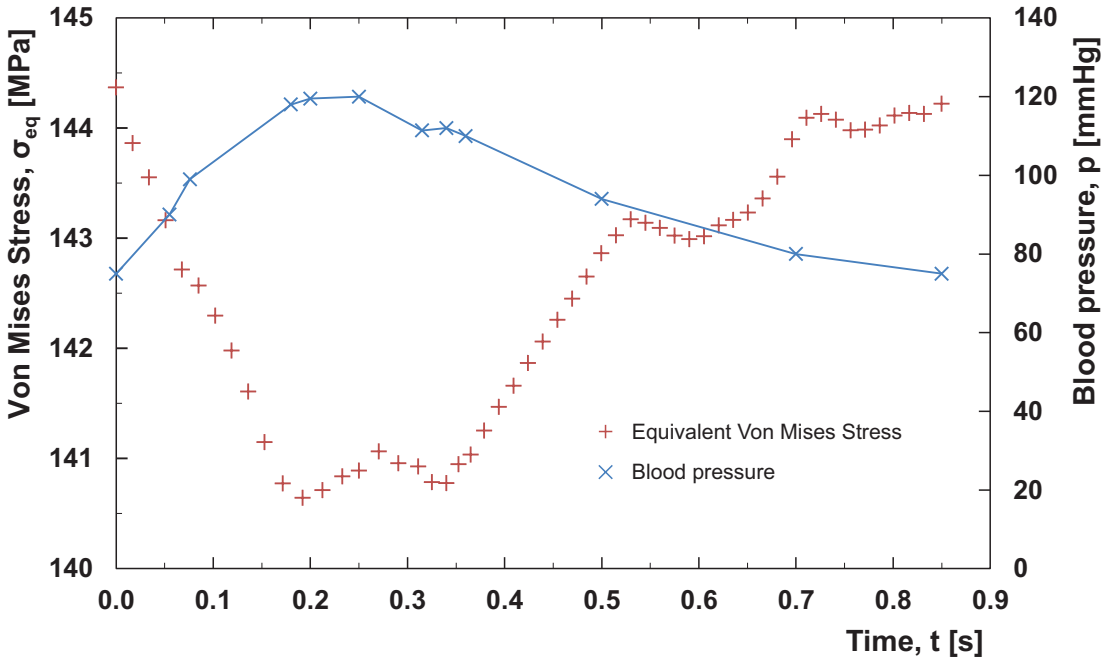

Figure 6.13: Stress evolution in the most loaded node

In the whole simulation of cardiac cycle, maximal stresses can be found at the time step which is shown in Figure 6.12. Blood pressure characteristics which is defined in the last loadcase causes radial enlargement of aorta and consequently, the stent. Thus, stresses in stent can be either lower or the same as they are at this time step. In the Figure 6.13, history plot of Equivalent Von Mises Stress in the extremal node (see Figure 6.12) according to the simulation time is shown. Similarly to previous study of loading the stent into a catheter, the highest values of stress occurs on the inner side of the bends. For clarity, pressure characteristics which was defined as a piecewise linear function is shown in the same figure as well.

As a conclusion of this study, we can finally identify a stress evolution in the most loaded node of stent. According to the results shown in Figure 6.13, stress range of the cycle is 4 MPa with mean value of 142 MPa. Stress fluctuations which are present especially in the final part of the diagram can be attributed to contact related issues.

Apart from the stress distribution in stent, it is also interesting to examine stress which occurs in the model of aorta. Maximum stress state throughout this feature is shown in Figure 6.14. In this time step, pressure which is defined as a boundary condition at the inner side of the aorta reaches its peak value of 120 mmHg. Together with that, radial deformation of aorta is also at its maximum. At both ends of the aorta model, an influence to the results due to displacement boundary conditions can be clearly seen. Nevertheless, this phenomenon is fading away together with rising distance from both ends. In the area where stent/aorta contact takes place, an influence of stress state due to these boundary conditions is reduced as much as possible. Maximum stress in the aortic wall is 0.076 MPa and maximal circumferential strain of the aorta is 11%.

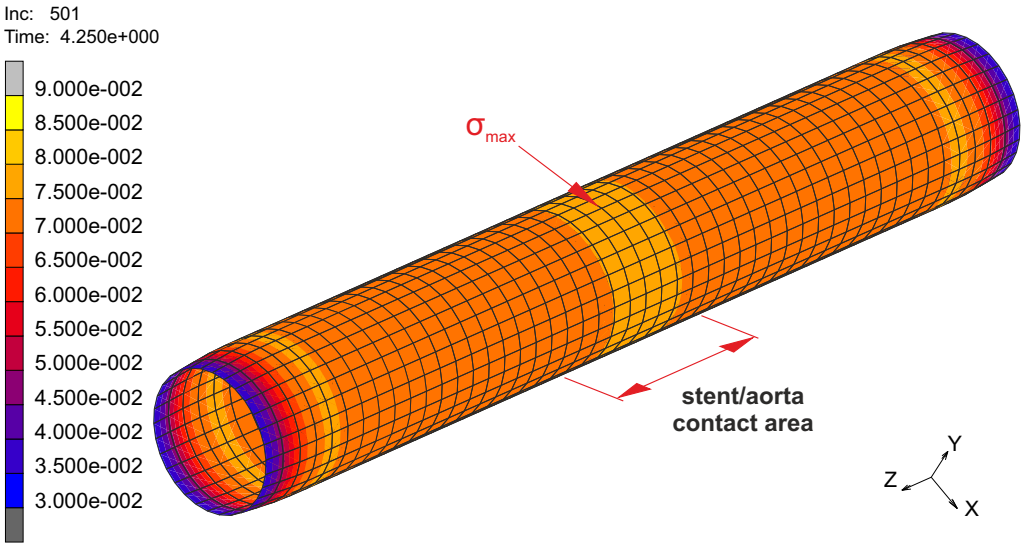

Figure 6.14: Stress distribution in aortic wall at systolic pressure
Equivalent Von Mises Stress [MPa]

Second figure from evaluation of the stresses in aortic wall (Figure 6.15) contains history plot of Equivalent Von Mises Stress in the extremal node (see Figure 6.14) according to the simulation time. As it can be seen, the stress in aortic wall follows the presure characteristics which was applied as a boundary condition. As mentioned above, Equivalent Von Mises Stress reaches the highest value of 0.076 MPa at the moment when systolic pressure is applied and 0.049 MPa during diastolic pressure.

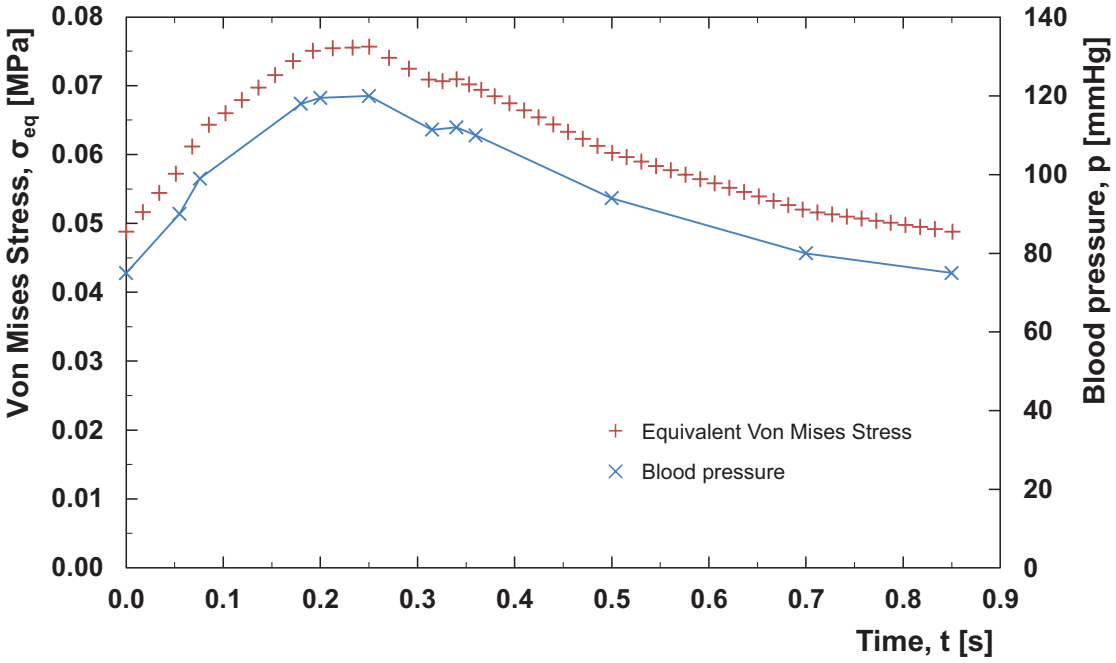

Figure 6.15: Stress evolution in the most loaded node

6.5 Durability analysis of the stent

At this point, the results from previously done mechanical tests and FEM simulations offer a possibility to perform durability analysis of the stent structure. In Section 4.4, nominal stress approach as a life prediction tool was introduced together with needed input parameters. Durability analysis of the stent was done in MSC.Patran software, version 2013 provided with MSC.Fatigue module. Following subsection deals more in detail with inputs of the analysis.

6.5.1 Input parameters

Input 1: Stress distribution data

For this input, a configuration of the stent at the beginning of the cardiac cycle was used. This state was already displayed in the Figure 6.12 but for clarity, the stress distribution

in stent is shown in Figure 6.16 without the model of aorta. As it was addressed before, the stresses acting throughout the stent are the highest at the beginning of the cardiac cycle, i.e. while diastolic pressure acts on aortic wall.

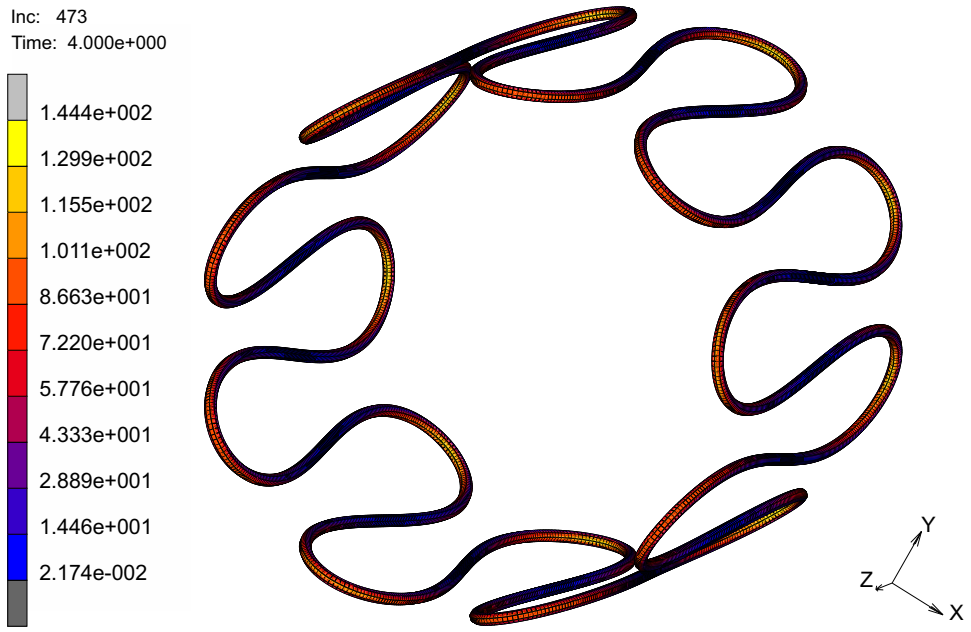

Figure 6.16: Durability analysis of the stent: stress distribution in stent

Input 2: Loading history

Second input deals with time variation of the static stress results from input 1. In our case, this characteristic is shown in Figure 6.13. To the needs of durability analysis, Equivalent Von Mises Stress characteristic from proposed graph was normalized according to the highest value of the cycle. Final loading history which forms second input of the analysis is shown in Figure 6.17.

Input 3: S-N curve of the material

Fatigue curve is the last input needed for submission of the job. Due to the fact that the stent is now considered to be implanted into aorta, the S-N data from cyclic tests carried out under 37°C were used. In the figure 6.18, the S-N data are plotted from MSC.Fatigue material database in which it was entered. One can notice that the display is in log-log scale. Thus, even high cycle fatigue part of the diagram is now displayed as a line.

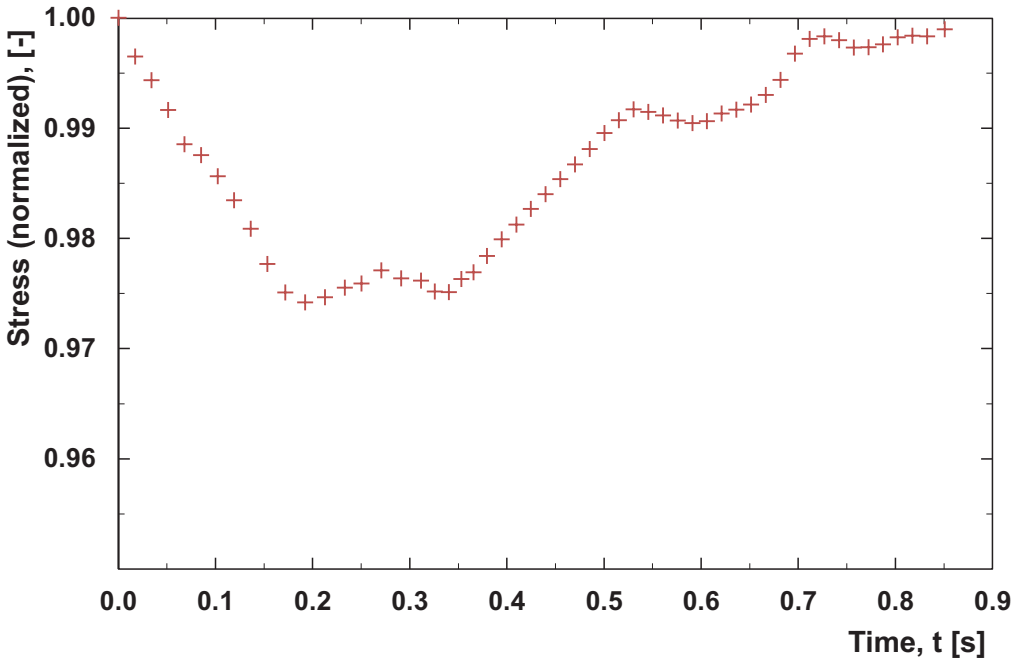

Figure 6.17: Durability analysis of the stent: loading history

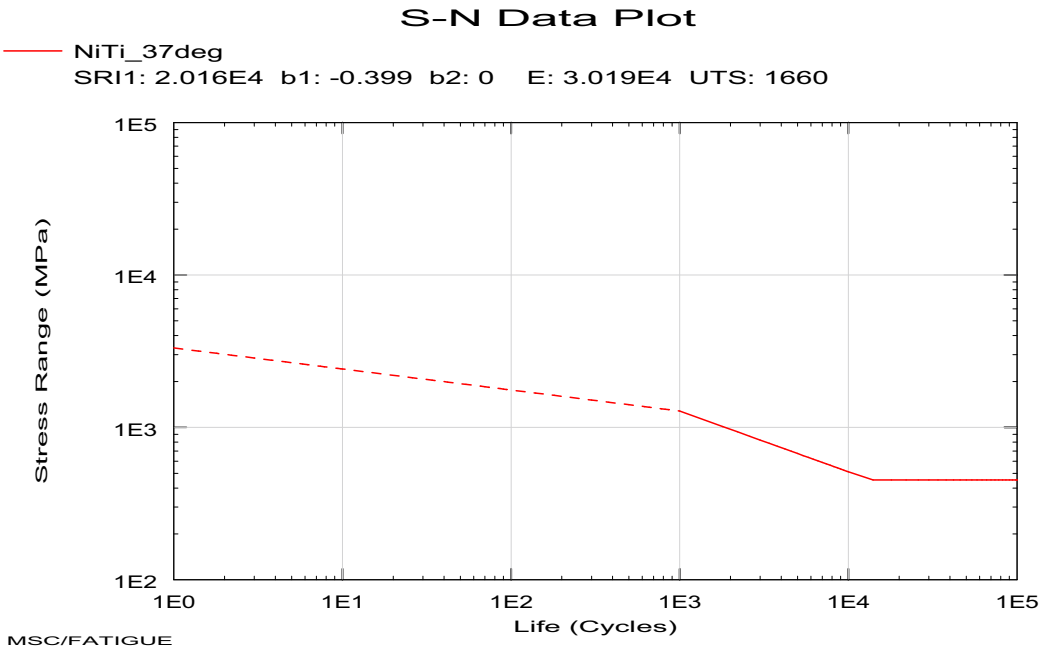

Figure 6.18: Durability analysis of the stent: NiTi S-N curve

6.5.2 Results

Standard outcome of durability analysis are quantities such as damage and life in cycles. In the Figure 6.19, Log of Damage throughout the whole structure is displayed. Results show that no damage, even in the highest loaded areas, is present.

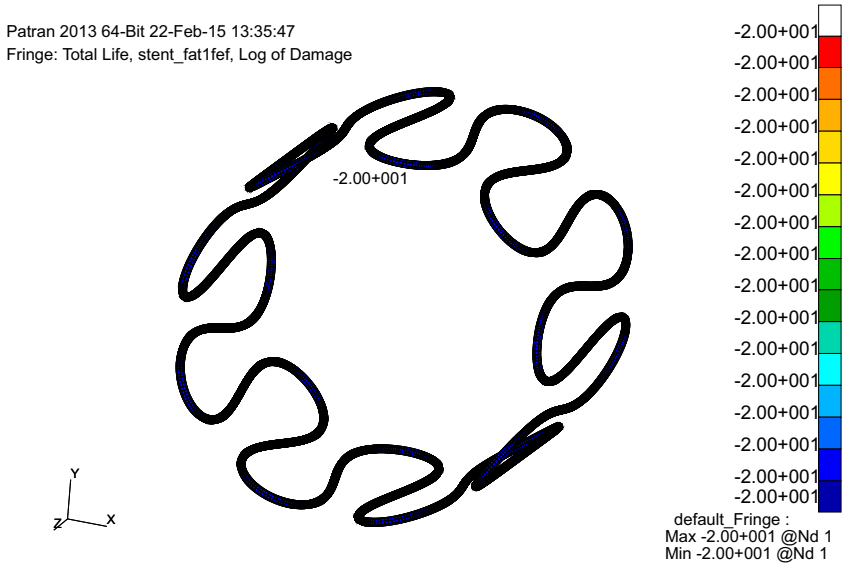

Figure 6.19: Result of stent durability analysis
Log of Damage

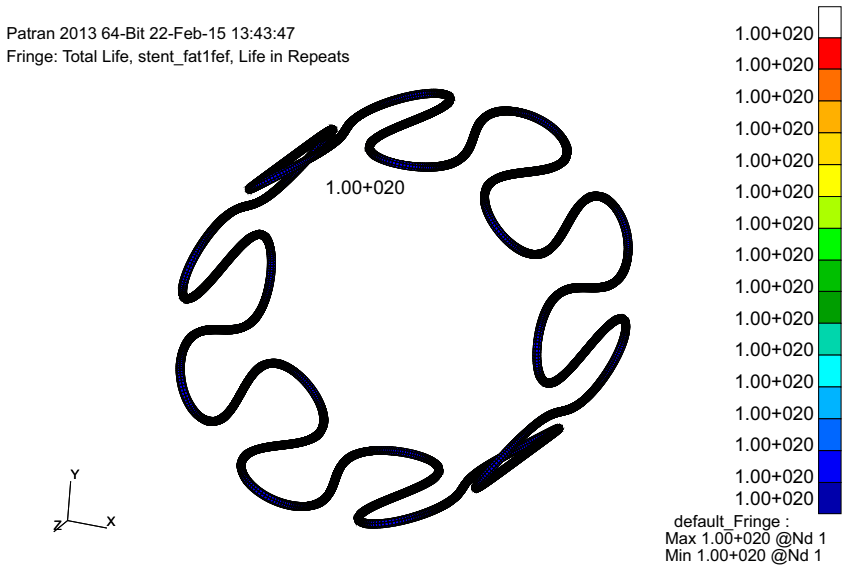

Figure 6.20: Result of stent durability analysis
Life in Repeats

The fact that to damage is present in the structure is supported with display of Life in Repeats quantity (Figure 6.20). As it can be seen, for all the parts of the structure an infinite life was estimated. Thus, it can be concluded that no malfunction of the stent caused by cyclic change of its diameter in aorta should be present during its life.

6.6 Chapter summary

In this chapter, all the possible loadcases which are connected with implantation and following life of the stent were studied using finite element method and NSA durability analysis. Initial work dealt with verification of material models which are implemented in MSC.Marc software. Simulation of tensile test of the wire specimen and crush test of a stent were carried out. History data gained from simulations were confronted with experimental values which lead to selection of Saeedvafa material model for further work.

First study was aimed to simulation of squeezing a stent into catheter with 24 F (8 mm) outer diameter. For this purpose, a stent made of 0.35 mm wire with outer diameter of 27 mm was used. This type of stent has the biggest diameter of the whole stent-graft structure and after an implantation it is in contact with abdominal aorta. Results of this simulation shows that such a high compression of the stent is capable of starting the martensitic transformation in bends of the structure (see Figure 6.9). Thus, long time storage of the stent in a catheter (for instance during transportation of the device to patient) cannot be recommended as it would cause its permanent deformation.

Next simulation was designed to evaluate how a stress varies in stent while it is implanted into an artery and subjected to systolic/diastolic pressure pulse. Data from previous part were used and the model was supplemented with a tubular structure which represented aorta. This new feature was characterized by Raghavan material model. History plot at the extremal node of the stent showed the stress evolution during the pulse (see Figure 6.13). The cycle can be described to have a mean value of stress 142 MPa and stress range of 4 MPa. Another outcome of this simulation was stress distribution in aortic wall. It was found that the highest values of stress occur when systolic pressure is applied. At this moment, peak value of stress in aortic wall is 0.07 MPa. In the work of Kleinstreuer et al. [58], authors dealt with closed cell design stent/aorta interaction. In contrast with our work, isotropic material model was used for aorta. Results of the study shows highest Von Mises stress in aortic wall of 0.265 MPa. Raghavan et al. tested their material model on a geometry of aorta with AAA which was loaded with systolic pressure [67]. In their case, 0.27 MPa was reported as a peak value of the Von Mises stress. Similar study with different geometry was done by Danao et al. [68]. Authors of this report marked 0.55 MPa as a peak value of Von Mises stress in aortic wall.

Last part dealt with durability analysis of the stent due to its cycling in aorta. The goal was to verify whether stresses acting on stent could cause a fatigue failure. For this purpose,

MSC.Fatigue solver based on Nominal Stress Approach was used. Results showed that no damage is present under previously evaluated stress cycle as peak values of stress are lower than fatigue limit of the material.

Chapter 7

Development of stent-graft durability testing device

7.1 Chapter introduction

In the two previous chapters, the work dealt with characterization of material properties and then with application of a FEM to solution of various stent-related load cases. At this point it must be said that in the case of FEM analysis, many factors which may influence the durability of a stent were omitted. Among these factors, the most important are a highly corrosive environment and influence of the graft to the overall properties of stent-graft.

Due to the hard implementation of above mentioned factors into FEM simulations, it was decided to evaluate life of the whole stent-graft in conditions similar to human body. As a result, the work was aimed to construction of a dedicated device which will be able to test bifurcated stent-grafts.

7.2 Overview of existing solutions

To my knowledge, there are only two commercially available solutions which are suitable for bifurcated stent-graft fatigue testing. First of them is provided by the American company BOSE ElectroForce Systems Group and it is called ElectroForce Stent/Graft Test Instrument (Figure 7.1). The system consists of mock arteries, two closed-loop pulsatile power heads and manifolds and a laser measurement system. Thanks to the laser monitoring of the artery's diameter evolution, it is possible to maintain strain conditions similar to the biologic ones in desired part of the mock artery. Interchangeable faces of the system allow for clamping variety of the mock arteries and therefore testing many types of stent-grafts. In the case of bifurcated type of the stent graft, the mock artery has a diameter of 32 mm and it is possible to perform a fatigue test up to the frequency of 60 Hz.

This test device seems to be very useful, but it is a question how a failure of the stent

is monitored. Apart from this, price of the machine (54,000 USD) is another limiting factor which makes it inaccessible for our purpose.

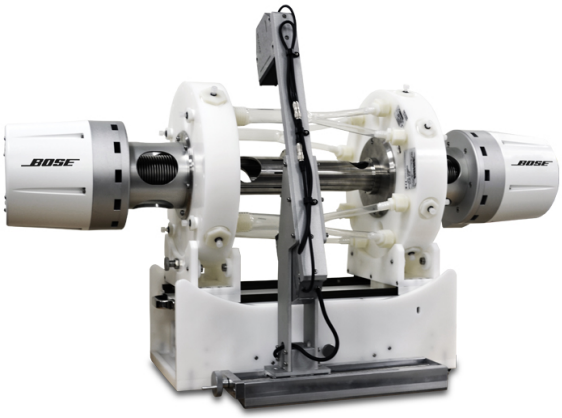

Figure 7.1: BOSE ElectroForce Stent/Graft Test Instrument

Second stent-graft life testing solution is produced by Dynatek Labs company. The Universal Stent Tester (Figure 7.2) is equipped with a single linear motor that drives fluid with a pulsatile motion into the whole sample.

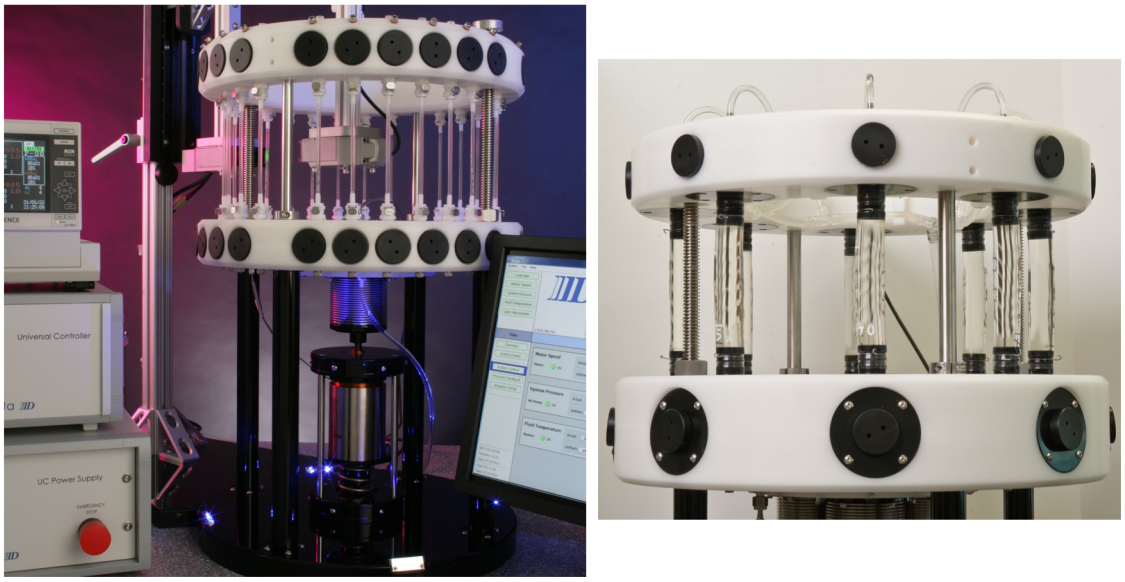

Figure 7.2: Dynatec Labs UST (Universal Stent Tester)

Dynatek Labs challenges the use of two motors for creation of pressure pulse. Main objection against this solution, which is used in the case of BOSE Stent/Graft Test Instrument, is that the two wave fronts rush toward themselves and collide in the middle of mock artery.

According to available data, this method creates valid testing conditions only in certain part of the artery. Described effect is more present in the case of longer samples, where the two extremities of the sample are further away from the central test region on the sample.

7.3 Principle of experimental device

For starters, several facts about basic functionality of the device must be stated. In the process of designing the machine, few assumptions and simplifications ware made in comparison with biologic blood flow in vessels. First and maybe major simplification is the way the stent graft is loaded. In my design I considered that shape change of the stent during systolic/diastolic pressure alteration is a factor which influence its fatigue life the most. Thus, the device can be designed in such a manner that a liquid does not necessarily have to flow through the stent-graft. Closed system, in which pressure alteration and subsequent shape change of the stent is caused by compression of the liquid allows for more compact device. What is more, the design will prevent a need of external pumps and liquid reservoirs.

General scheme of the proposed device is shown in Figure 7.3. In the concern of cyclic tests efficiency, we decided to design a machine which will be able to test eight bifurcated stent-grafts at the same time. First notable thing about the device is a method used for the pressure pulse generation. Alternating of systolic and diastolic pressure is governed by cam mechanism with flat rotating follower. Although the linear motors which are used in above described commercial solutions are precise and easily programmable, their price is still very high. Moreover, their power is limited and simultaneous run of eight samples would require an adequately large motor. On the other hand, radial cams can be easily fabricated thanks to Electroerosion machining with very high precision and surface quality.

Circular motion of the cam is transferred via flat follower to linear motion of the transferring rod. Precise guidance of this part is ensured by linear bearing SKF LTBR12-2LS. Rod is then connected with the centre of a membrane by a screw. The membrane, together with pressure chamber, forms a whole in which a final pressure pulse is generated. This pulse is led via bushings and piping to mock arteries fabricated of silicone. In these models, stent-grafts are deployed and a pressure pulse enlarges its diameter. One can note that the mock arteries are tightened upside-down in the system. This solution has two reasons: Firstly, it is easier to have only eight inputs into the upper part of the device instead of sixteen if the system was set physiologically. Another comparison with philological state shows that the pressure pulse also begins in aorta and then it spreads into common illiac arteries.

For the tests, physiological saline (sterile solution of NaCl) is used as a process liquid. This solution is commonly used in medicine for cleaning of flesh wounds and incisions. It is also served intravenously in the case of developed dehydration. Saline solution will also represent a corrosive environment which affects the stent while implanted into the blood vessel.

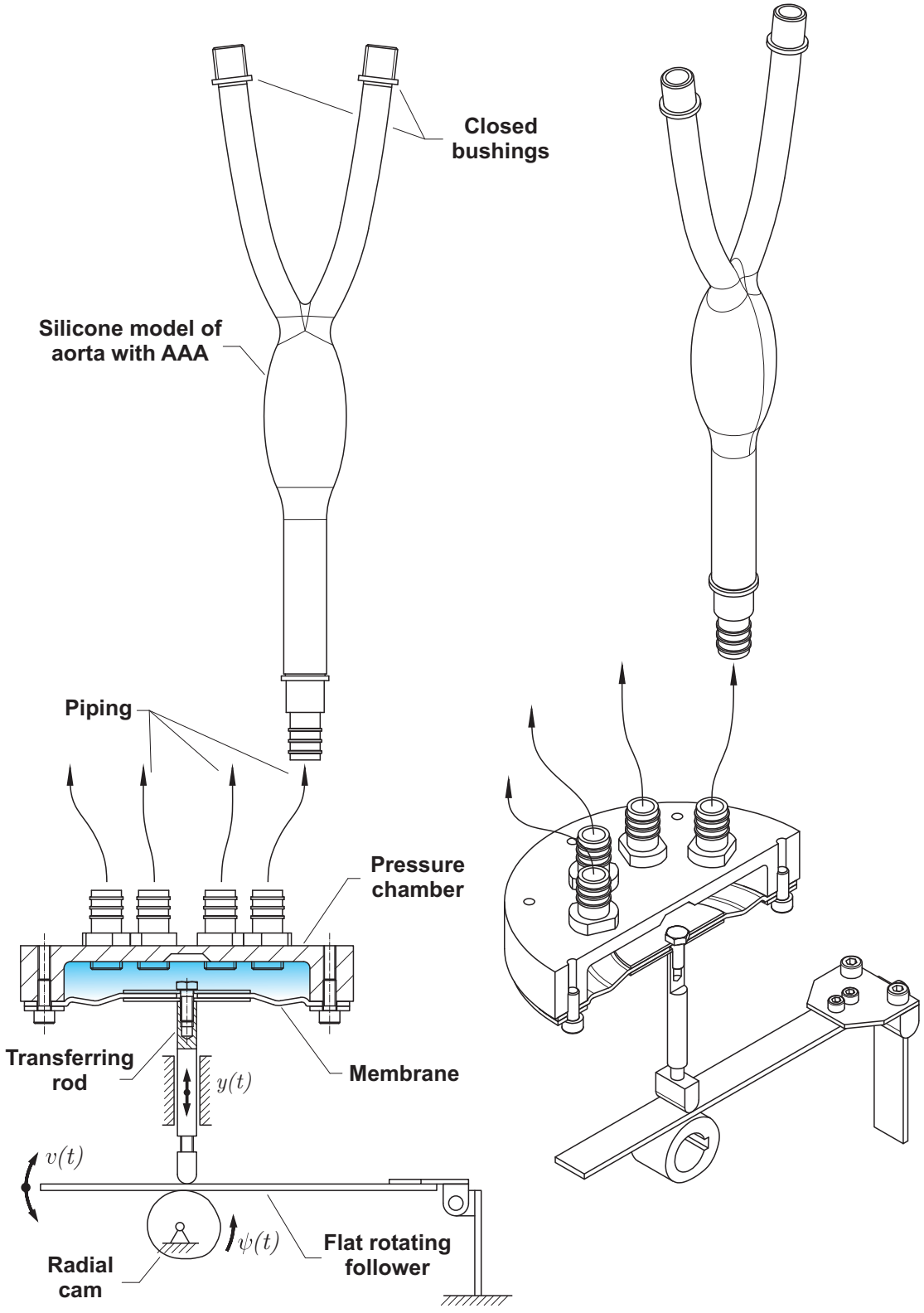

Figure 7.3: Device for cyclic testing of Stent-Grafts; Principle of function

The whole hydraulic system is closed with use of a silicone plugs (Figure 7.4). The purpose of these elements is not only to seal the end bushings but they are also meant as an entry part for optical inspection of stents.

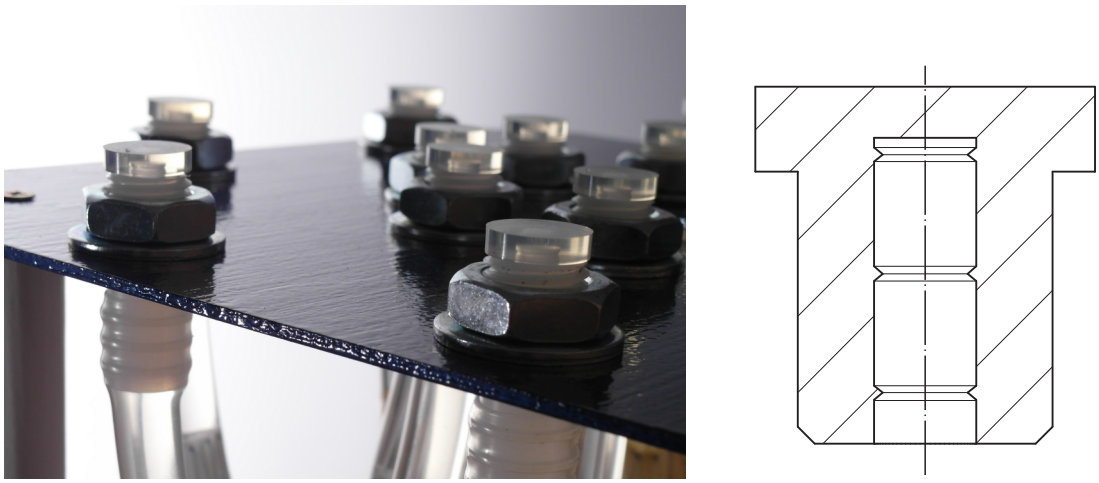

Figure 7.4: Silicone plugs at the top of the system

7.4 Cam mechanism

In this part, a cross-sectional shape of a radial cam in normal plane will be evaluated. In the case of proposed device, the pressure characteristic which was introduced in Section 2.1.3) should be present in mock arteries. Thus, first part of this section deals with evaluation of input parameters needed for successful synthesis of a radial cam with regard to precise alteration between systolic and diastolic pressure. The kinematic scheme of the problem is shown in Figure 7.5 in which the cam profile is highlighted in red colour. The centre of cam's rotation is marked as "0" and the flat follower is characterized by line m with centre of rotation in point M. During the work of this type of cam mechanism, the distance between these two points is constant in time.

First desired input parameter for cam synthesis is denoted as $v(t)$ and it represents an angle of the follower in certain time. Second input parameter needed for evaluation of cam's shape is connected with relative motion of a cam versus machine's frame - an angle $\psi(t)$. On the basis of the two functions, it is possible to evaluate all the parameters of cam's outer profile. For the actuation of the whole system, a stepper motor with constant value of angular velocity ω will be used. Thus, second input function will be defined simply as $\psi(t) = \omega t$. On the other hand, function $v(t)$ must be derived with regard to pressure evolution in aorta.

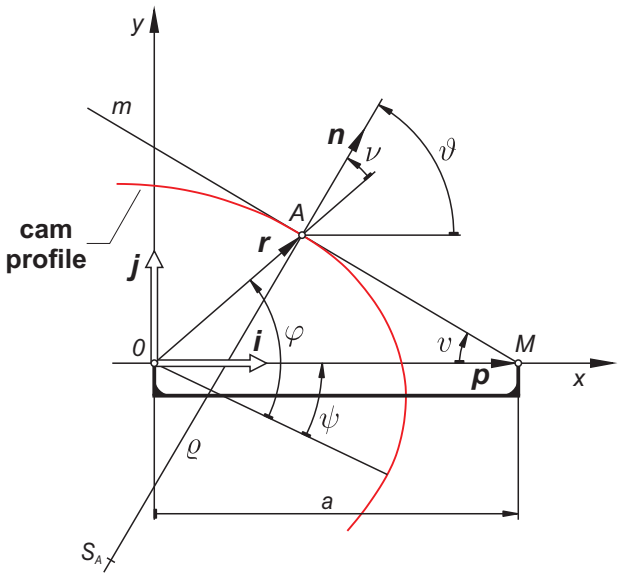

Figure 7.5: Radial cam with a rotating flat follower [69]

7.4.1 Evaluation of v(t) function

All the calculations in this section were carried out in Maplesoft MAPLE 14 software and the whole program can be found in Appendix D. First step in derivation of $v(t)$ function was fitting data of average blood pressure (120 mmHg systolic and 80 mmHg diastolic) gained from publication of S. Silbernagl [7]. For this purpose, a cubic spline was used (Figure 7.6).

After the mathematical expression of the pressure curve was done, movement of another two members of the mechanism could be analysed. To excite a water column, the centre of membrane and transferring rod carry out the same linear movement of a specific deviation. In order to easily compute the quantities which characterize the movement of these two components, we can estimate a volume change needed to achieve biologic circumferential strain during systolic pressure. In the article of Stefanidis et al. [70], a blood pressure-aorta diameter relation was measured with aid of ultrasonic displacement meter. According to the data, a circumferential strain of the aorta during peak value of the pressure is $\varepsilon_c = 8\%$ for healthy individuals.

Provided we have a silicone mock artery with value of elastic modulus similar to the aortic wall. According to the analysis of CAD data, the initial volume of one mock artery is $V_0 = 274{,}708\,\mathrm{mm}^3$ and outer diameter of the aneurysm part is 50 mm. If the diameter underwent prescribed strain, the volume of an aorta will have to enlarge ε_c^2 times. Due to the fact that eight models will be cycled at the same time, final volume change of the liquid in all the mock arteries has to be $\Delta V = 8V_0\varepsilon_c^2 = 14{,}065\,\mathrm{mm}^3$.

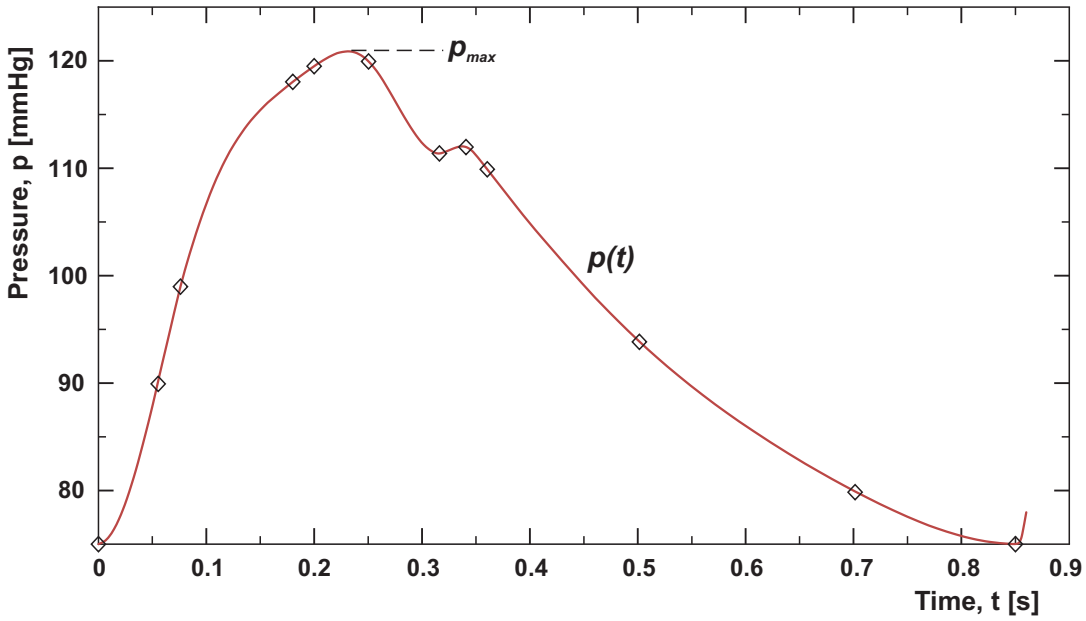

Figure 7.6: Fit of the data by Spline function

Volume change caused by membrane and its fastening plate in pressure chamber during a stroke is considered to have the form of conical frustum (Figure 7.7).

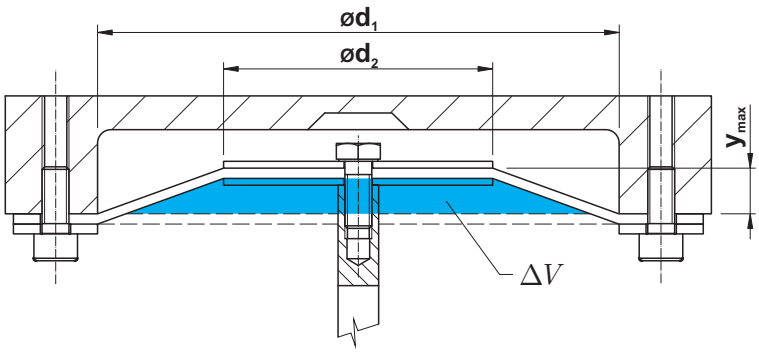

Figure 7.7: Volume change during one stroke

Desired travel y_{max} can be assessed according to the relationship which defines conical frustum volume. With known volume and diameters of pressure chamber and membrane's fastening plate, height of the frustum can be calculated as following:

$$y_{max} = \frac{3\Delta V}{\pi \left(r_1^2 + r_1 r_2 + r_2^2\right)} \tag{7.1}$$

Finally, full characteristic of membrane's linear motion $y(t)$ can be evaluated. For this purpose, a pressure function $p(t)$ from Figure 7.6 was normalized. This step produces a dimensionless function which begins and ends at the value of zero and which peak value equal to one. The function is subsequently multiplied by the amplitude y_{max}:

$$y(t) = \frac{p(t) - p_{min}}{p_{max} - p_{min}} \cdot y_{max} \tag{7.2}$$

All the previous calculations lead to quantification of $v(t)$ function which describes an angle of the follower at the certain time (Figure 7.8).

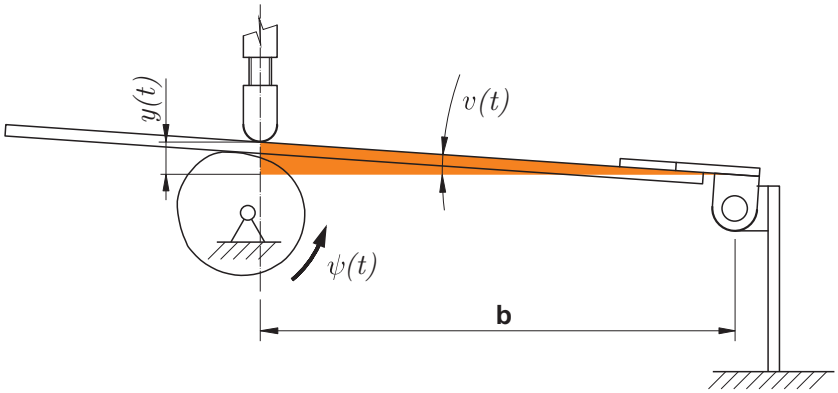

Figure 7.8: Evaluation of $v(t)$ function

According to the highlighted triangle in previous Figure, the $v(t)$ function was expressed as following:

$$v(t) = \arctan \frac{y(t)}{b} \tag{7.3}$$

In the Figure 7.9, the $v(t)$ function and its two derivations are expressed graphically for one cycle. The device is meant to work ten times faster than the actual biologic pulse. Keeping in mind that values of velocity and acceleration grows with rising cycle frequency, the plots are expressed for the highest frequency for which the machine is designed, i.e. 10 Hz.

7.4.2 Synthesis of radial cam

As soon as the both input functions $v(t)$ and $\psi(t)$ are known, all the parameters of radial cam can be evaluated. Following equations for cam synthesis are adopted from publication of Koloc et al. [69]. Same as in previous section, the synthesis was performed in Maplesoft MAPLE 14 software and the whole program is enclosed in Appendix D.

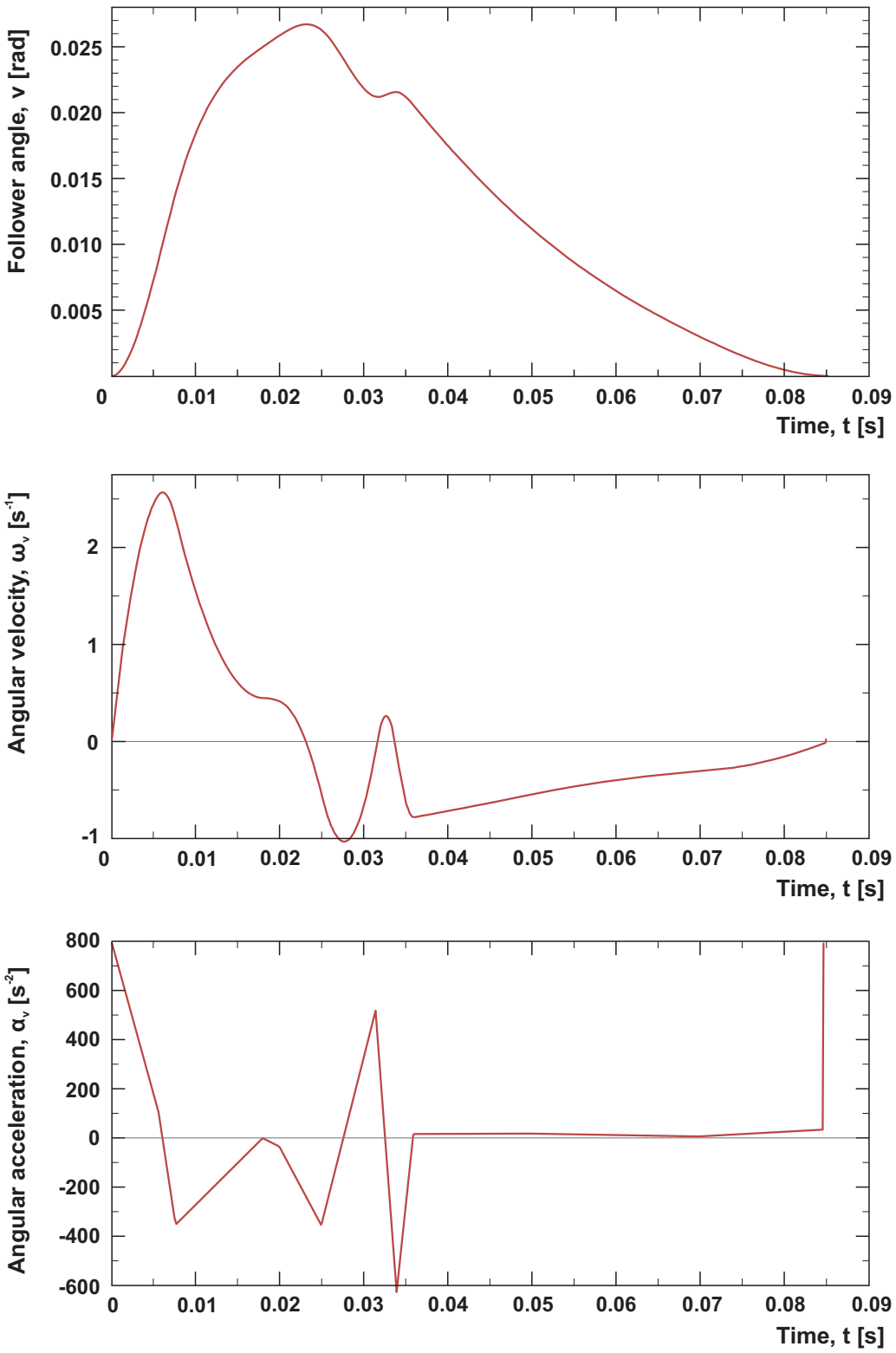

Figure 7.9: Graphical expression of $v(t)$ function and its derivations

As mentioned in Section 7.4, one of the mechanism's parameter is distance between the centre of cam's and the centre of follower's rotation a which remains constant in time. For some calculations, a function defined as $S = \operatorname{sgn} v(t)$ will be also needed. First step of cam synthesis is evaluation of $q(t)$ function which describes distance evolution between centre of follower's rotation M and cam-follower touching point A (see Figure 7.5):

$$q = S\frac{\dot{\psi} a \cos v}{\dot{\psi} - \dot{v}} \tag{7.4}$$

Afterwards, the profile of the cam can be evaluated in polar coordinates according to the functions u and φ. The final profile is then shown in Figure 7.10. In this case, basic diameter of the cam's body is considered to be 20 mm.

$$u = \sqrt{a^2 + q^2 - 2Saq\cos v} \tag{7.5}$$

$$\varphi = \psi + S\arccos\frac{a - Sq\cos v}{u} \tag{7.6}$$

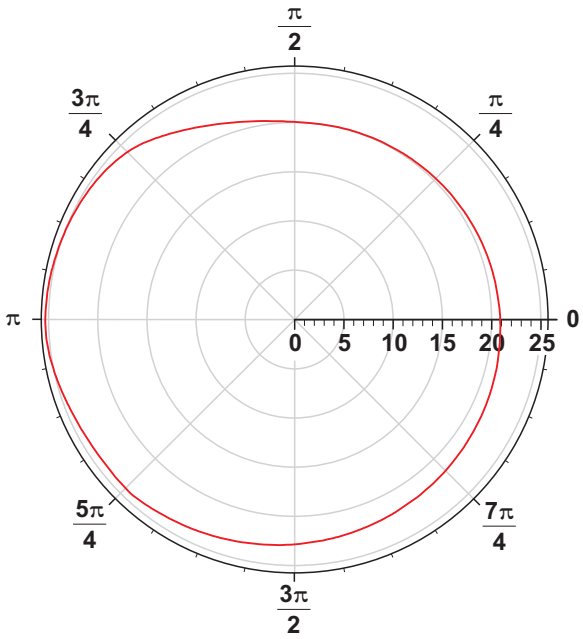

Figure 7.10: Profile of the cam in normal plane

In order to evaluate quality of cam's profile, a radius of curvature ϱ was calculated (Equation 7.7). Its graphical expression can be found in Appendix D.

$$\varrho = S\frac{a}{(\dot{\psi} - \dot{v})^3}\left[\dot{\psi}(\dot{\psi} - \dot{v})(\dot{\psi} - 2\dot{v})\sin v + (\dot{\psi}\ddot{v} - \ddot{\psi}\dot{v})\cos v\right]. \tag{7.7}$$

7.5 Final form of the device

From the functional point of view, the whole device can be divided into three sections, according to their specific function. First section which can be found on the bottom of the machine provides excitation of the system. Second unit which can be clearly distinguished is a pressure chamber with membrane. Last section which is situated on the top of the device is formed by mock arteries and their holders. In the following subsections, these assemblies will be described more in detail. Complete documentation and drawings of the parts can be found in Appendix F.

7.5.1 Excitation of the system

The unit is formed by stepping motor SANYO DENKI SM2862-5255 and a shaft which are connected together using flexible connector SRJ30 14-14. Shaft is then fastened between pair of SKF SY 20 TF pedestal bearing units (Figure 7.11). The cam which was made using electroerosion machining is connected to the shaft via parallel key. In order to reduce coefficient of friction between cam and follower, the cam is lubricated using an oil reservoir which is situated under cam. During each revolution, the cam dips into oil which lowers the probability of premature wear of these two highly loaded parts.

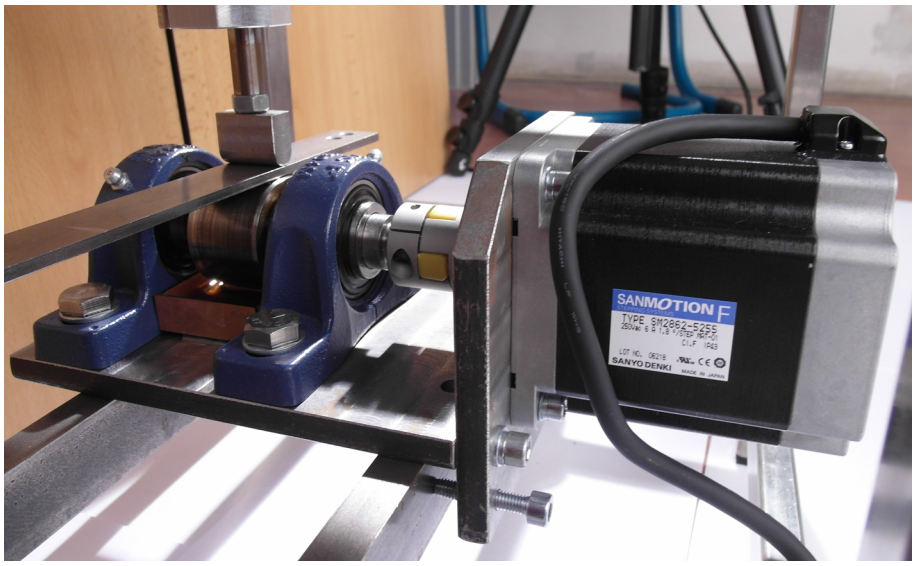

Figure 7.11: Drive unit of the device

During designing of the system, aortic pressure characteristic was normalized according to the Equation 7.2. As a consequence of this step, it must be somehow possible to adjust value of initial pressure in the system to the value of systolic pressure. In our case, there are two ways to do so. Firstly, the table which holds above described unit can be levelled

in vertical direction. In this case, the pressure rises due to slight deformation of membrane. Secondly, the whole system can be overfilled with liquid. Thanks to the fact that hydraulic system is closed and provided that all the components are sealed, it is possible to regulate value of pressure in the system.

7.5.2 Pressure chamber

Function and most of the parts which belong to this unit were introduced in Section 7.3. Body of pressure chamber is made of stainless steel, considering the fact that saline solution will be used as a process liquid. The membrane was cut out from a plate of 3 mm thick cord-reinforced rubber. This part is tied to pressure chamber with use of 3 mm thick metallic ring and eight screws.

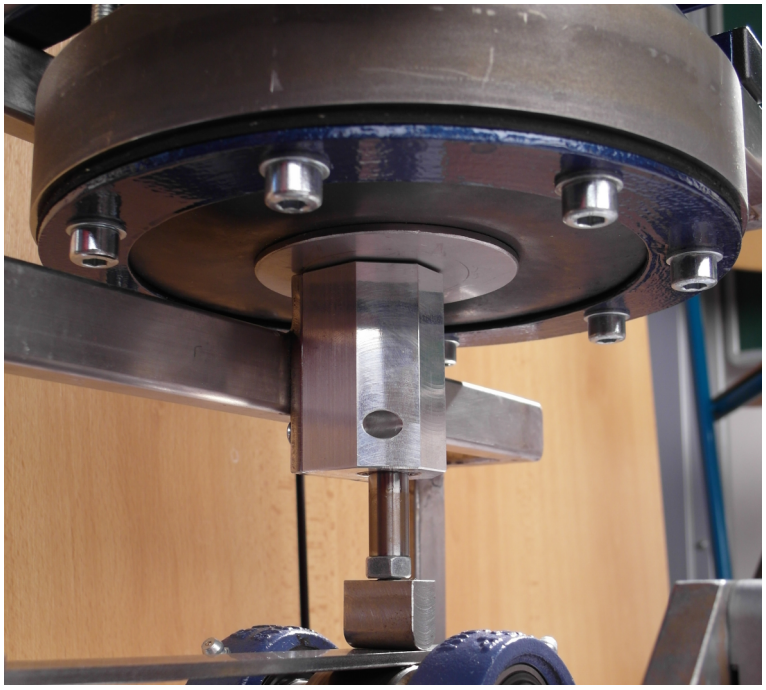

Figure 7.12: Pressure chamber with membrane

In the figure, a transferring rod with linear bearing can be also seen. The rod is connected to membrane using two circular stainless steel plates 2 mm thick. One of the plate is situated under and second plate above the membrane, i.e. in the chamber. Using a screw, all these parts are tighten together. This connection is also secured using thread sealant. On the top of the pressure chamber, there are eight bushings for connection with last section of the machine. Pressure chamber is also equipped with a screw which serves to let the air flow out while filling the system with process liquid.

7.5.3 Mock arteries

The last section of the machine serves to hold tested stent-grafts and to provide strain conditions similar to human body during testing. Stent-grafts are implanted into silicone model of an abdominal aorta with aneurysm. Abdominal aorta has very complex shape which is slightly different for each human. Considering this fact, exact model of the aorta would be very expensive to make. Moreover, such model would make no advantage for stent-graft testing. Thus, final model is considered to be symmetric about both longitudinal and frontal plane. The models are made of LR 3003 silicone with 30 ShA hardness.

Figure 7.13: Mock arteries with stent-grafts

7.6 Verification of pressure evolution

As soon as the device was assembled, another step for successful testing was calibration of the work cycle. To do so, we decided to measure pressure evolution in mock arteries during test run at three places of aorta (7.14):

1. Proximal part of aorta (p_1)
2. Centre of aneurysm (p_2)
3. Common iliac artery (p_3)

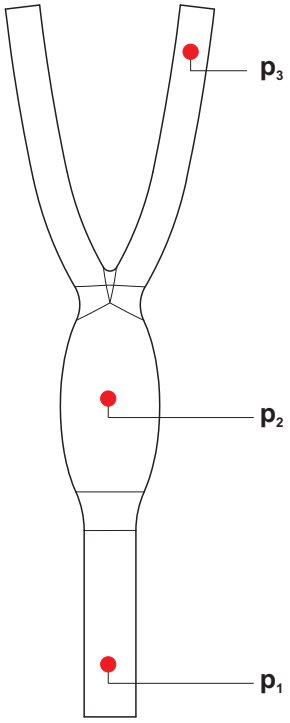

Figure 7.14: Places of pressure measurement

Pressure changes at selected places of mock artery were measured using SMC PSE543A-R06 sensors which operate in range of ±100 kPa. Data were recorded with National Instruments (NI) PXIe 1062Q via NI Shielded 68-Pin Connector Block SCB-68A. Due to the fact that output from the sensors during measurement is changes of voltage, this quantity had to be first correlated to values of pressure. According to the manufacturer, this relation should be linear.

7.6.1 Calibration of sensors

Thanks to SMC ZSE30AF-01-E switch which is already calibrated to display pressure values, we were able to calibrate the sensors. One pressure sensor and the switch were mounted to SMC KQ2T Union Tee and pressurized using Makita MAC610 compressor (Figure 7.15). With use of pressure regulation on the compressor, five values of pressure were correlated. During each of this of these correlations a value of voltage from pressure sensor and related value of pressure from the switch were registered. As a result, we obtained linear relation between output voltage of pressure sensors and pressure itself (Figure 7.16).

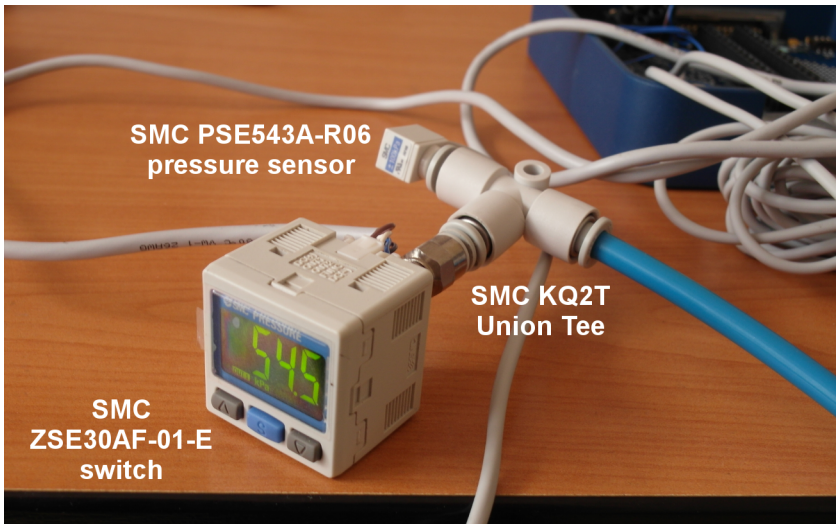

Figure 7.15: Calibration of sensors

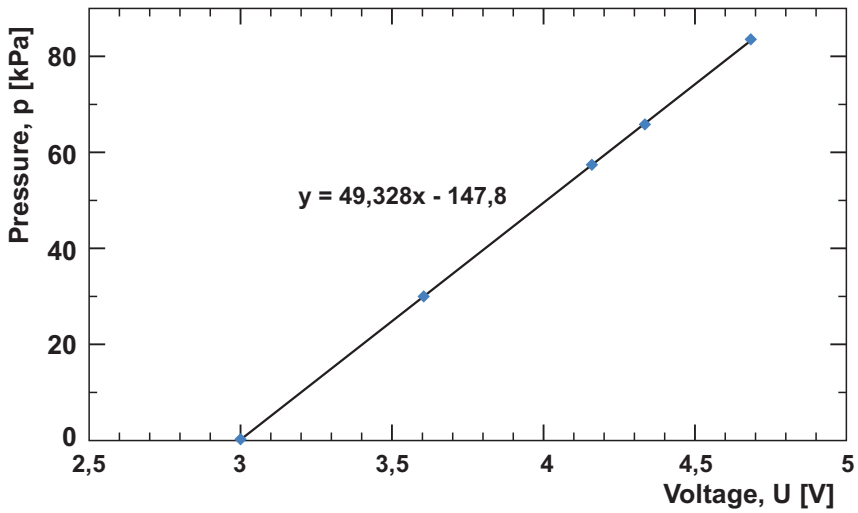

Figure 7.16: Resulting curve from sensor calibration

7.6.2 Pressure measurement

For the purpose of pressure measurement at selected parts of mock arteries, SMC plastic system tubes were mounted on the system through silicone plugs which are shown in the Figure 7.4. This was done in such a way that end of the tube reaches desired area in the mock artery. As a result of measuring, we obtained three values of pressure which allowed us for precise adjustment of the work cycle. The measuring assembly at the top of the machine is shown in the Figure 7.17 together with indication of individual channels p_1, p_2 and p_3.

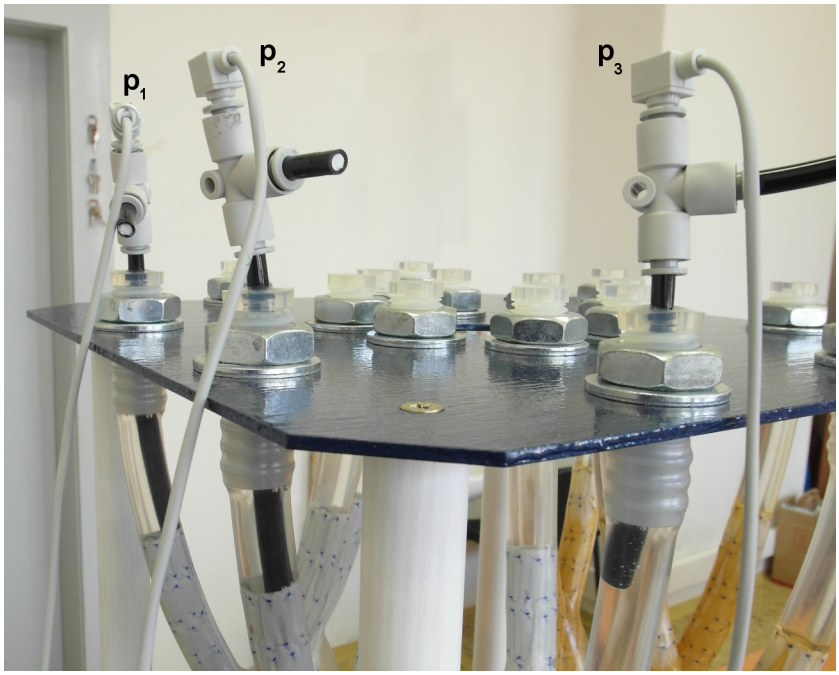

Figure 7.17: Detail of measuring assembly

In the first stages of measurement, one phenomenon was observed while evaluating the data from pressure sensors. Pressure pulse which spreads throughout the system during machine's run causes little vibrations of mock arteries. This is caused by the fact that the arteries are fixed to the device at its ends only. Thus, when filled with process liquid they are susceptible to transversal vibrations. In the Figure 7.18, measured signal is displayed with thin dashed line. Pressure alterations caused by transversal motion of mock arteries are relatively high which causes a resulting signal to be scattered. In order to obtain plain pressure characteristics in the system, the data were processed using two parameter Butterworth filter with order N=2 and cutoff frequency W_n=0.015 rad/s. In the Figure 7.18, comparison of raw and filtered signal can be seen.

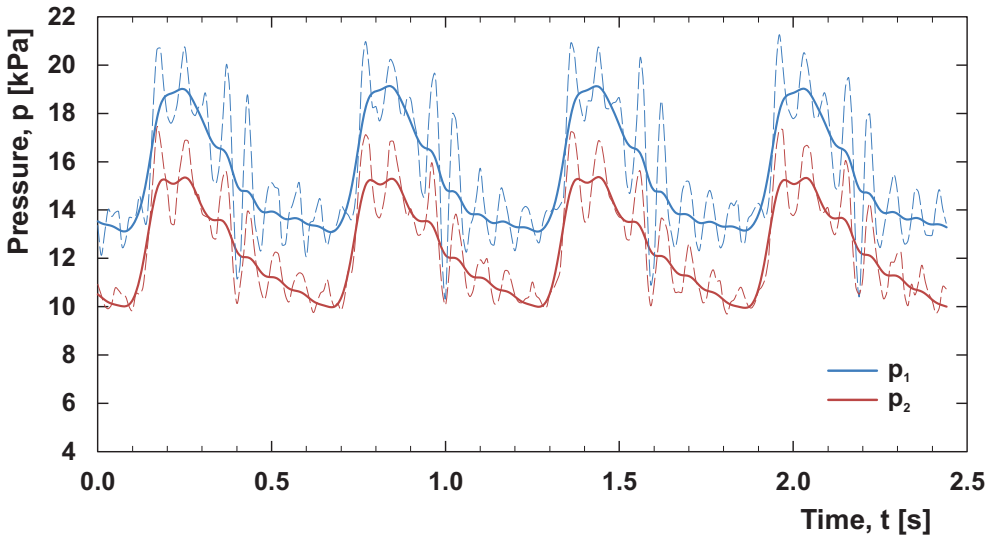

Figure 7.18: Display of raw and filtered signal

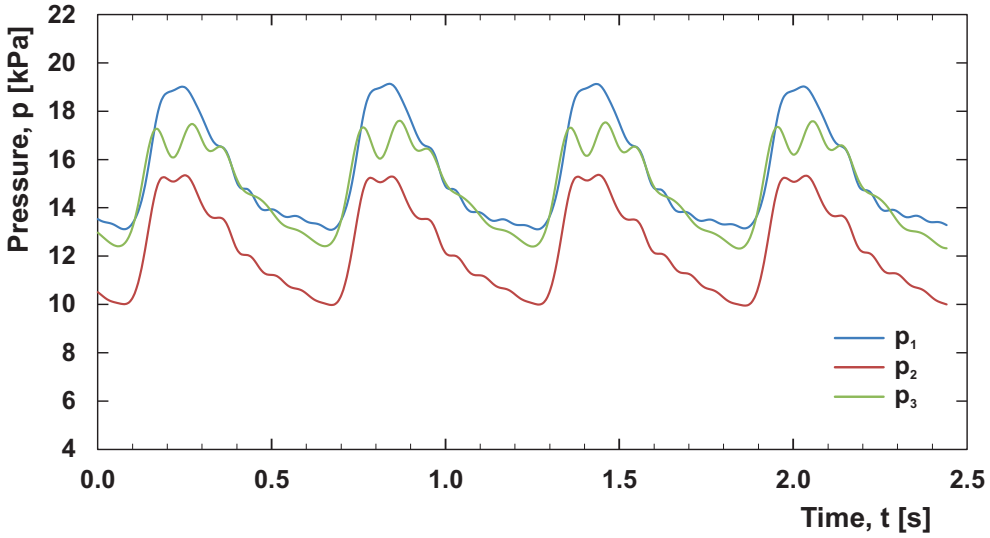

Figure 7.19: Results of pressure measurement at 1.7 Hz

In the following four figures (7.19 to 7.22), filtered signals from all the three sensors are displayed. Measurement was done for four frequencies according to the setting of potentiometer which is situated on motor's drive unit. The four settings of potentiometer were 0.00, 0.50, 1.00 and 1.50 while corresponding test frequencies are 1.7, 1.9, 2.0 and 2.4, respectively. Higher test frequency than the latter one lead to incorrect behaviour of the machine due to high transversal motion of mock arteries. Furthermore, membrane was not able to follow accelerated motion of the follower which lead to lose of contact between the follower and transferring rod.

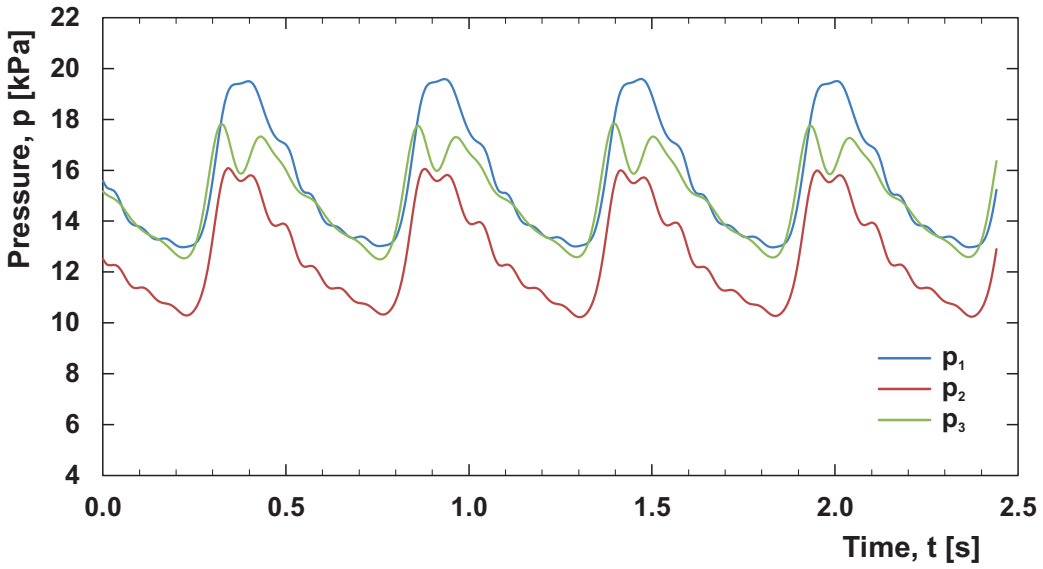

Figure 7.20: Results of pressure measurement at 1.9 Hz

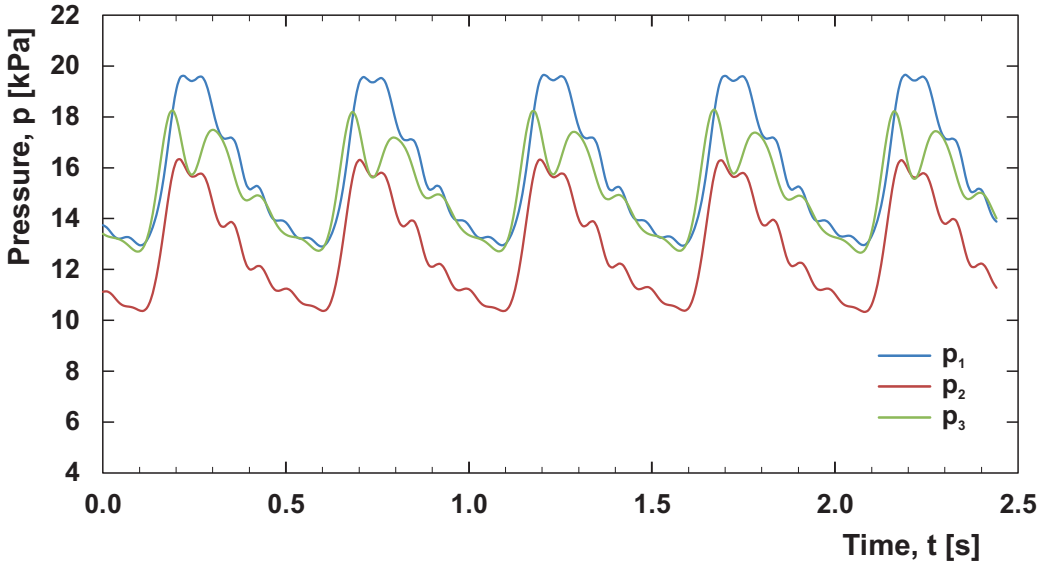

Figure 7.21: Results of pressure measurement at 2.0 Hz

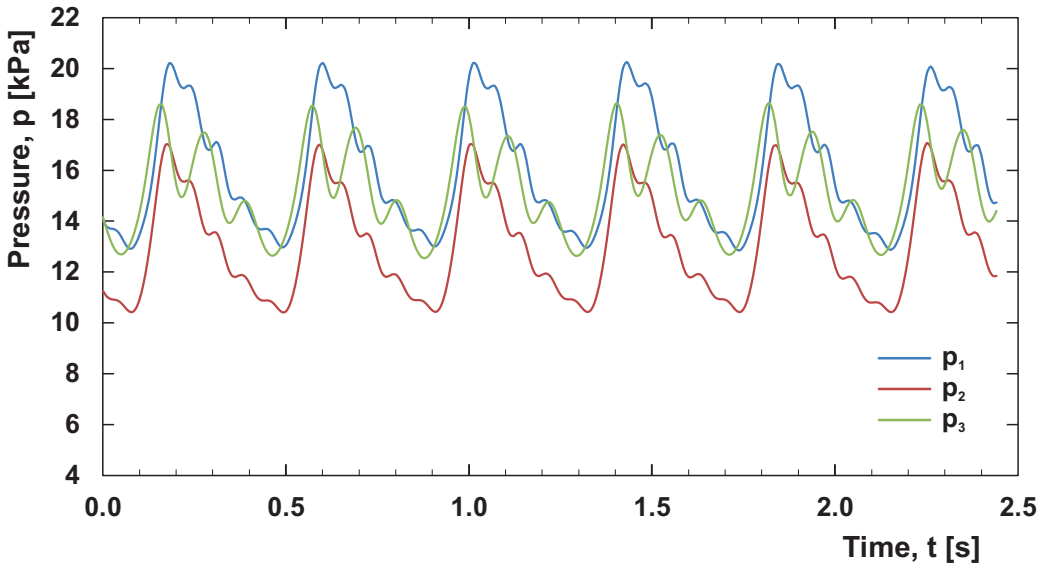

Figure 7.22: Results of pressure measurement at 2.4 Hz

7.7 Chapter summary

In this chapter, the whole process of designing the device dedicated to bifurcated stent-graft cyclic testing was described. On the basis of all the facts mentioned in the chapter and the results of pressure measurement, a final assessment of machine's functionality can be made.

In comparison with commercially available solutions which were introduced at the beginning of this chapter, the device is not capable of achieving such high testing frequency. As described in Section 7.6.2, testing at frequency higher than 2.5 Hz leads to incorrect behaviour of the work cycle. Result of this phenomenon can be seen in the Figure 7.22. Even though the signal filtration was applied, a big scatter of the resulting data can be observed. To solve the problem, mock arteries should be placed in such an environment which is capable to dampen their transversal motion. For instance, a water bath or some kind of foam structure can be used. Properties of the environment should be also close to those which are present in human body.

From the financial point of view, cost of the presented device (approx. 2,700 USD) together with injection mould for mock arteries (approx. 2,300 USD) is much lower than in the case of commercial devices. In future, the machine should be supplemented with more parts in order to be able to fully evaluate and regulate all the parameters of the work cycle. Among these, heating unit for process liquid and strain monitoring of mock arteries would be the most needed features. Positive aspect of the device is its potential variability. With simple modifications, various medical devices can be tested under desired conditions.

As a conclusion it could be stated that the device is fully operational and its limitations can be removed with minor constructional modifications. Though this concept would hardly ever reach testing frequencies of the devices which are excited using linear motor, it is a good solution for minor applications in which a variability plays a crucial role.

Figure 7.23: Full assembly of the device

Chapter 8

Conclusion

Minimally invasive operations such as endovascular repair of abdominal aortic aneurysm are of great importance for future development of surgery. Even today, many types operations which always demanded large open surgery can be carried out via small body incisions. Thus, any kind of advance and knowledge improvement in this field of interest can bring much help to the general public. I believe that the work and its results which were presented in my thesis will help to deepen the confidence in NiTi shape memory alloy for wider application in cardiovascular surgery and medicine in general. In this conclusion, only major facts and new contributions to present problematic are described because each chapter contains summary of corresponding results.

First practical part of this thesis is covered in Chapter 3 and it dealt with characterisation of mechanical properties for a NiTi alloy which is commonly used in health applications. At the beginning, alloy composition was evaluated using Energy-dispersive X-ray microanalysis. Due to the fact that no major temperature changes are present during the life of a stent, only pseudoelastic effect of the alloy was evaluated. This phenomenon was mapped thanks to Differential scanning calorimetry and tensile tests which were carried under under three different values of temperature. One of the main parts of the thesis is included in this chapter and it deals with fatigue properties of given NiTi alloy. Load driven cyclic tests were carried out in order to construct S-N curve of the material. Main contribution of this chapter can be seen in precise description of material's pseudoelastic behaviour. In my view, last part which dealt with fatigue characterization offers reliable and consistent S-N data of the material. Thanks a frequent application of this kind of NiTi alloy in biomedicine, these data are very useful for other authors. Limitation of the data lies in the fact that the cyclic tests were done under stress control with positive value of stress ratio R. Apart from this fact, strain-driven tests may be also very valuable because strain-based approaches are getting more and more attention in both high and low cycle fatigue. These areas will be dealt with in further work of my research.

In second part of the thesis, i.e. Chapter 6, all the possible loadcases which occur during

life of the stent were took into consideration and simulated using finite element method in MSC.Marc 2014.0.0 software. For this purpose, mechanical data from previous chapter were used for precise definition of material constants in shape memory alloy material models. To assure right function of these models, two experimental tests were carried out and the results were confronted with simulation of the same problem. Three main studies dealt with following problems: squeezing a stent into catheter, deployment of the stent in blood vessel and analysis of stress variation in stent during cardiac cycle. Latter study offered data needed for last and most valuable point of this chapter. Performing durability analysis with nominal stress approach we tried to answer a question whether stresses acting in stent structure during cardiac cycle may cause failure due to fatigue of the material. Results of the durability analysis showed that no damage is present under previously evaluated stress cycle as peak values of stress are lower than fatigue limit of the material. The topic of FEM analysis of loading a stent into catheter has already been published for various types of stents. What is new to the topic is the use of numerical durability analysis of the stent. To the author's knowledge, this topic has not been published so far in this field of interest. The authors such as C. Kleinstreuer et al. [58] and Alan R. Pelton et al. [71] assessed the fatigue resistance of diamond shaped stent structure with use of strain approach. Their studies are based on static FEM analysis and comparison of resulting strain data with limit values from strain-driven fatigue tests. Described approach does not take a strain alteration in the stent during cardiac cycle into account and it is limited to comparison of maximal values of strain with ε-N curve only. As it can be seen, study presented in this thesis brings new insight and approaches to the topic. Considering limits, presented data lacks influence of graft to the overall results. Moreover, the durability analysis might be also carried out via some of the local approaches in order to compare the results with nominal stress approach.

Last part of the thesis is dedicated to constructional solution of the machine which is capable to perform fatigue testing on the whole stent-graft structure. The machine is driven by stepping motor and cardiac cycle is generated with use of cam mechanism. Function of the whole machine was verified experimentally thanks to measurement of pressure characteristics in mock arteries. Outcome of practical tests with this device showed that the machine will need further development and modifications to fulfil desired parameters, especially desired frequency of the cycle of at least 10 Hz was not reached. Strong side of the device is that it can be easily modified to perform any type of loading cycle and it can be equipped with variety of mock arteries. All the parts of the machine which are in contact with process liquid are designed to sustain corrosive environment and elevated values of temperature. In the following work, I would like to perform all the design changes needed to reach the desired parameters of the working cycle and to equip the machine with a system for measurement of circumferential change of mock artery diameter. All these changes will ensure proper function of the device and hence it will be capable to fulfil its purpose - cyclic testing of stent-grafts.

Bibliography

[1] Wang, Z.L. - Kang, Z.C. *Functional and Smart Materials: Structural Evolution and Structure Analysis*. Springer, 1998. ISBN 0-306-45651-6.

[2] Duerig, T. - Pelton, A. - Stöckel, D. An overview of nitinol medical applications. *Materials Science and Engineering: A*. 1999, vol. 273, pp. 149–160.

[3] Gray, H. *Anatomy of the human body*. Bartleby.com; 20th edition, 2000. ISBN 978-1587341021.

[4] Taylor Jr., L.M. - Porter, J.M. Basic data related to clinical decision-making in abdominal aortic aneurysms. *Annals of vascular surgery*. 1987, vol. 1, no. 4, pp. 502–504.

[5] *Zygote Body* [online]. Zygote Media Group, Inc., 2012. [acc. 07-May-2014]. URL `http://zygotebody.com/`.

[6] Čihák, R. *Anatomie 3 (druhé, upravené a doplněné vydání)*. Grada publishing, 2004. ISBN 80-247-1132-X.

[7] Silbernagl, S. *Color atlas of pathophysiology*. Thieme, 2010. ISBN 978-3131165527.

[8] Klabunde, R.E. *Arterial Blood Pressure* [online]. 2014. [acc. 29-April-2014]. URL `http://www.cvphysiology.com/Blood%20Pressure/BP002.htm`.

[9] Adam van der Vliet, J. - Boll, A.P. Abdominal aortic aneurysm. *The Lancet*. 1997, vol. 349, no. 9055, pp. 863–866.

[10] Johnston, K.W. - Rutherford, R.B. - Tilson, M.D. et al. Suggested standards for reporting on arterial aneurysms. *Journal of vascular surgery*. 1991, vol. 13, no. 3, pp. 452–458.

[11] Reed, D. - Reed, C. - Stemmermann, G. et al. Are aortic aneurysms caused by atherosclerosis? *Circulation*. 1992, vol. 85, no. 1, pp. 205–211.

[12] Upchurch Jr., G.R. - Schaub, T.A. Abdominal aortic aneurysm. *Am Fam Physician*. 2006, vol. 73, no. 7, pp. 1198–204.

[13] Sakalihasan, N. - Limet, R. - Defawe, O. Abdominal aortic aneurysm. *The Lancet*. 2005, vol. 365, no. 9470, pp. 1577–1589.

[14] Arko, F.R. - Smith, S.T. - Zarins, C.K. Repair of infrarenal abdominal aortic aneurysms. In *ACS surgery: principles & practice*, edited by W.W. Souba M.P. Fink, 6th edition, pp. 1105–1166. WebMD Professional Publishing, June 2007. ISBN 978-0977222629.

[15] Tilson, M. Aortic aneurysms and atherosclerosis. *Circulation*. 1992, vol. 85, no. 1, pp. 378–379.

[16] MacSweeney, S. - Powell, J. - Greenhalgh, R. Pathogenesis of abdominal aortic aneurysm. *British journal of surgery*. 1994, vol. 81, no. 7, pp. 935–941.

[17] Lindholt, J.S. - Henneberg, E.W. - Fasting, H. et al. Hospital based screening of 65–73 year old men for abdominal aortic aneurysms in the county of Viborg, Denmark. *Journal of medical screening*. 1996, vol. 3, no. 1, pp. 43–46.

[18] Brown, L.C. - Powell, J.T. et al. Risk factors for aneurysm rupture in patients kept under ultrasound surveillance. *Annals of surgery*. 1999, vol. 230, no. 3, p. 289.

[19] Blanchard, J.F. - Armenian, H.K. - Friesen, P.P. Risk factors for abdominal aortic aneurysm: results of a case-control study. *American journal of epidemiology*. 2000, vol. 151, no. 6, pp. 575–583.

[20] Vardulaki, K. - Walker, N. - Day, N. et al. Quantifying the risks of hypertension, age, sex and smoking in patients with abdominal aortic aneurysm. *British journal of surgery*. 2000, vol. 87, no. 2, pp. 195–200.

[21] Rasmussen, T.E. - Hallett Jr, J.W. - Tazelaar, H.D. et al. Human leukocyte antigen class II immune response genes, female gender, and cigarette smoking as risk and modulating factors in abdominal aortic aneurysms. *Journal of vascular surgery*. 2002, vol. 35, no. 5, pp. 988–993.

[22] Greenhalgh, R. Comparison of endovascular aneurysm repair with open repair in patients with abdominal aortic aneurysm (EVAR trial 1), 30-day operative mortality results: randomised controlled trial. *The Lancet*. 2004, vol. 364, no. 9437, pp. 843–848.

[23] Thompson, M. Controlling the expansion of abdominal aortic aneurysms. *British journal of surgery*. 2003, vol. 90, no. 8, pp. 897–898.

[24] Gillum, R.F. Epidemiology of aortic aneurysm in the United States. *Journal of clinical epidemiology*. 1995, vol. 48, no. 11, pp. 1289–1298.

[25] Law, M. Screening for abdominal aortic aneurysms. *British medical bulletin*. 1998, vol. 54, no. 4, pp. 903–913.

[26] Wolf, Y. - Bernstein, E. A current perspective on the natural history of abdominal aortic aneurysms. *Vascular*. 1994, vol. 2, no. 1, pp. 16–22.

[27] US Preventive Services Task Force et al. Screening for abdominal aortic aneurysm: recommendation statement. *Annals of Internal Medicine*. 2005, vol. 142, no. 3, p. 198.

[28] Parodi, J.C. - Palmaz, J. - Barone, H. Transfemoral intraluminal graft implantation for abdominal aortic aneurysms. *Annals of vascular surgery*. 1991, vol. 5, no. 6, pp. 491–499.

[29] Lederle, F.A. - Freischlag, J.A. - Kyriakides, T.C. et al. Outcomes following endovascular vs open repair of abdominal aortic aneurysm: a randomized trial. *Jama*. 2009, vol. 302, no. 14, pp. 1535–1542.

[30] Schillinger, M. - Gschwendtner, M. - Reimers, B. et al. Does carotid stent cell design matter? *Stroke*. 2008, vol. 39, no. 3, pp. 905–909.

[31] Otsuka, K. - Wayman, C.M. *Shape memory materials*. Cambridge University Press, 1999. ISBN 0-521-663849.

[32] Lagoudas, D.C. *Shape memory alloys: modeling and engineering applications*. Springer, 2008. ISBN 978-0-387-47684-1.

[33] Bartzela, T.N. - Senn, C. - Wichelhaus, A. Load-deflection characteristics of superelastic nickel-titanium wires. *The Angle orthodontist*. 2007, vol. 77, no. 6, pp. 991–998.

[34] Bourauel, C. - Drescher, D. - Ebling, J. et al. Superelastic nickel titanium alloy retraction springs-an experimental investigation of force systems. *The European Journal of Orthodontics*. 1997, vol. 19, no. 5, pp. 491–500.

[35] McNichols Jr, J. - Brookes, P. - Cory, J. NiTi fatigue behavior. *Journal of Applied Physics*. 1981, vol. 52, no. 12, pp. 7442–7444.

[36] Eggeler, G. - Hornbogen, E. - Yawny, A. et al. Structural and functional fatigue of NiTi shape memory alloys. *Materials Science and Engineering: A*. 2004, vol. 378, no. 1, pp. 24–33.

[37] Piedboeuf, M. - Gauvin, R. - Thomas, M. Damping behaviour of shape memory alloys: strain amplitude, frequency and temperature effects. *Journal of Sound and Vibration*. 1998, vol. 214, no. 5, pp. 885–901.

[38] Gloanec, A.L. - Cerracchio, P. - Reynier, B. et al. Fatigue crack initiation and propagation of a TiNi shape memory alloy. *Scripta Materialia*. 2010, vol. 62, no. 10, pp. 786–789.

[39] Miller, D.A. - Lagoudas, D.C. Influence of cold work and heat treatment on the shape memory effect and plastic strain development of NiTi. *Materials Science and Engineering: A*. 2001, vol. 308, no. 1, pp. 161–175.

[40] Perkins, J. - Muesing, W. Martensitic transformation cycling effects in Cu-Zn-Al shape memory alloys. *Metallurgical Transactions A*. 1983, vol. 14, no. 1, pp. 33–36.

[41] Jones, N. - Dye, D. Martensite evolution in a NiTi shape memory alloy when thermal cycling under an applied load. *Intermetallics*. 2011, vol. 19, no. 10, pp. 1348–1358.

[42] McKelvey, A. - Ritchie, R. Fatigue-crack propagation in Nitinol, a shape-memory and superelastic endovascular stent material. *Journal of biomedical materials research*. 1999, vol. 47, no. 3, pp. 301–308.

[43] Melton, K. - Mercier, O. Fatigue of NiTi thermoelastic martensites. *Acta Metallurgica*. 1979, vol. 27, no. 1, pp. 137–144.

[44] Van Humbeeck, J. Cycling effects, fatigue and degradation of shape memory alloys. *Le Journal de Physique IV*. 1991, vol. 1, no. C4, pp. C4–189.

[45] Miyazaki, S. - Otsuka, K. Development of shape memory alloys. *ISIJ International*. 1989, vol. 29, no. 5, pp. 353–377.

[46] Janssen, J. - Willems, F. - Verelst, B. et al. The fatigue properties of some cu-zn-al shape memory alloys. *Le Journal de Physique Colloques*. 1982, vol. 43, no. C4, pp. C4–809.

[47] Duerig, T. - Pelton, A. Ti-Ni shape memory alloys. *Materials properties handbook: Titanium alloys*. 1994, pp. 1035–1048.

[48] Tobushi, H. - Hachisuka, T. - Yamada, S. et al. Rotating-bending fatigue of a TiNi shape-memory alloy wire. *Mechanics of Materials*. 1997, vol. 26, no. 1, pp. 35–42.

[49] Moumni, Z. - Van Herpen, A. - Riberty, P. Fatigue analysis of shape memory alloys: energy approach. *Smart materials and structures*. 2005, vol. 14, no. 5, p. S287.

[50] Polizzotto, C. A Study on Plastic Shakedown of Structures: Part I—Basic Properties. *Journal of Applied Mechanics*. 1993, vol. 60, no. 2, pp. 318–323.

[51] Auricchio, F. A robust integration-algorithm for a finite-strain shape-memory-alloy superelastic model. *International Journal of Plasticity*. 2001, vol. 17, no. 7, pp. 971–990.

[52] Auricchio, F. - Taylor, R.L. - Lubliner, J. Shape-memory alloys: macromodelling and numerical simulations of the superelastic behavior. *Computer methods in applied mechanics and engineering*. 1997, vol. 146, no. 3, pp. 281–312.

[53] Auricchio, F. - Sacco, E. A one-dimensional model for superelastic shape-memory alloys with different elastic properties between austenite and martensite. *International Journal of Non-Linear Mechanics*. 1997, vol. 32, no. 6, pp. 1101–1114.

[54] Duga, J. - Fisher, W. - Buxbaum, R. et al. Fracture costs United-States 119 Billion Dollars a year, says study by Battelle NBS. *International Journal of Fracture*. 1983, vol. 23, no. 3, pp. R81–R83.

[55] Amzallag, C. - Gerey, J. - Robert, J. et al. Standardization of the rainflow counting method for fatigue analysis. *International journal of fatigue*. 1994, vol. 16, no. 4, pp. 287–293.

[56] Khosrovaneh, A. - Dowling, N. Fatigue loading history reconstruction based on the rainflow technique. *International Journal of Fatigue*. 1990, vol. 12, no. 2, pp. 99–106.

[57] Ruzicka, M. - Papuga, J. New Concept of a Local Elastic Stress Approach for Fatigue Life Calculation. In *International Committee on Aeronautical Fatigue (ICAF)*. 2001. ISBN ISBN 2-85428-5743 pp. 161–174.

[58] Kleinstreuer, C. - Li, Z. - Basciano, C. et al. Computational mechanics of Nitinol stent grafts. *Journal of biomechanics*. 2008, vol. 41, no. 11, pp. 2370–2378.

[59] Höhne, G. - Hemminger, W. - Flammersheim, H.J. *Differential scanning calorimetry*. Springer, 2003. ISBN 978-3-662-06710-9.

[60] ASTM Standard F2004-05, 2010. "Standard Test Method for Transformation Temperature of Nickel-Titanium Alloys by Thermal Analysis", 2010. DOI: 10.1520/F2004-05R10, URL `http://www.astm.org`.

[61] Danley, R. Power compensation differential scanning calorimeter, September 26 2001. EP Patent App. EP20,010,106,270, URL `http://www.google.com/patents/EP1136803A1?cl=en`.

[62] Grolleau, V. - Louche, H. - Delobelle, V. et al. Assessment of tension–compression asymmetry of NiTi using circular bulge testing of thin plates. *Scripta Materialia*. 2011, vol. 65, no. 4, pp. 347–350.

[63] Gall, K. - Sehitoglu, H. - Chumlyakov, Y.I. et al. Tension–compression asymmetry of the stress–strain response in aged single crystal and polycrystalline NiTi. *Acta Materialia*. 1999, vol. 47, no. 4, pp. 1203–1217.

[64] Liu, Y. - Xiang, H. Apparent modulus of elasticity of near-equiatomic NiTi. *Journal of alloys and compounds*. 1998, vol. 270, no. 1, pp. 154–159.

[65] Huang, X. - Liu, Y. Effect of annealing on the transformation behavior and superelasticity of NiTi shape memory alloy. *Scripta Materialia*. 2001, vol. 45, no. 2, pp. 153–160.

[66] US Food and Drug Administration and others. Guidance for industry and FDA staff - Non-Clinical Engineering Tests and Recommended Labeling for Intravascular Stents and Associated Delivery Systems, 2010.

[67] Raghavan, M. - Vorp, D.A. Toward a biomechanical tool to evaluate rupture potential of abdominal aortic aneurysm: identification of a finite strain constitutive model and evaluation of its applicability. *Journal of biomechanics*. 2000, vol. 33, no. 4, pp. 475–482.

[68] Danao, L.A.M. - Publico, A.S. Development of an Alternative Diagnostic Tool for Rupture Risk Assessment of Abdominal Aortic Aneurysms Using Finite Element Simulation. *Philippine Engineering Journal*. 2006, vol. 27, no. 1, pp. 29–42.

[69] Koloc, Z. - Václavík, M. *Vačkové mechanismy*. SNTL - Nakladatelství technické literatury, 1988. ISBN 978-0444986641.

[70] Stefanadis, C. - Stratos, C. - Vlachopoulos, C. et al. Pressure-diameter relation of the human aorta a new method of determination by the application of a special ultrasonic dimension catheter. *Circulation*. 1995, vol. 92, no. 8, pp. 2210–2219.

[71] Pelton, A.R. - Gong, X.Y. - Duerig, T. Fatigue testing of diamond-shaped specimens. In *Medical Device Materials: Proceedings from the Materials & Processes for Medical Devices Conference*. 8-10 September 2003, Anaheim, California, pp. 199–204.

Publications of the Author related to the topic

Ackermann M. - Čapek L. Modelling of materials with shape memory effect with using finite element method. In *Proceedings of the 47th Experimental Stress Analysis conference.* 2011, Znojmo, Czech Republic. ISBN: 978-80-214-4275-7, pp. 11-16.

Čapek L. - Ackermann M. The Role of Graft to the Crush Resistance of the Stent-graft. In *Proceedings of IASTED BioMech 2011 conference.* 2011, Pittsburg, USA. ISBN: 978-0-88986-913-4 pp. 87-90.

Ackermann M. - Čapek L. Numerical durability evaluation of Nitinol stent. *Computer Methods in Biomechanics and Biomedical Engineering.* 2012, Volume 5, Supplement 1, Taylor & Francis Group, ISSN: 1025-5842, pp. 99-101. **IF 1,169**.

Ackermann M. - Čapek L. Verifikace materiálových modelů slitin s tvarovou pamětí v programu MSC.Marc. In *sborník příspěvků semináře "Výpočty konstrukcí metodou konečných prvků 2014".* 2014, ISBN: 978-80-261-0445-2, pp. 4-7.

Other publication activities

Ackermann M. - Čapek L. Optimization of unicondylar knee replacement according to contact pressure. *International Journal for Simulation and Multidisciplinary Design Optimization.* Volume 4, Number 3-4, e-ISSN: 1779-6288, pp. 167-170.

Ackermann M. - Henyš P. Natural frequencies of INSTRON Electropuls E3000 testing machine. In *Proceedings of 14th International Conference "Applied Mechnics 2012".* 2012, Pilsen, Czech republic. ISBN: 978-80-261-0097-3 pp. 77-80.

Ackermann M. - Čapek L. - Henyš P. Biomechanical analysis of mini-screw pullout strength. In *Proceedings of Human Skin Engineering and Reconstructive Surgery conference.* 2013, Prague, Czech republic. ISBN: 978-80-7372-956-1 pp. 3-4.

Ackermann M. - Šafka J. - Zelený P. et al. Properties of Models Produced by Direct Selective Laser Melting Technology. *Applied Mechanics and Materials.* 2014, Volume 693: Novel Trends in Production Devices and Systems II. ISSN: 1660-9336 pp. 231-236.

Appendices

Appendix A

Fracture surfaces

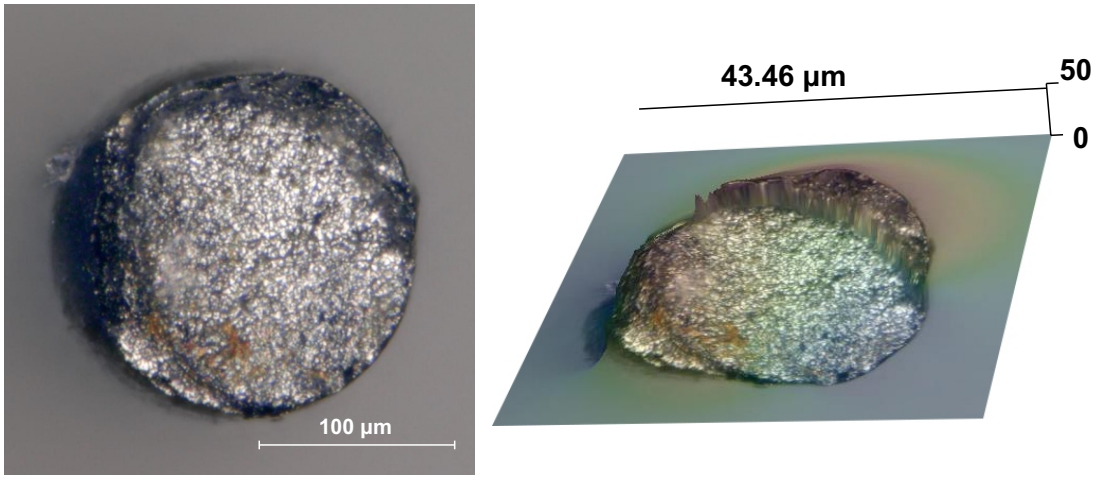

Figure A.1: Fracture surface of NiTi wire cycled in pure martensitic phase; $T = 37°\mathrm{C}$; $\sigma_{max} = 980\,\mathrm{MPa}$

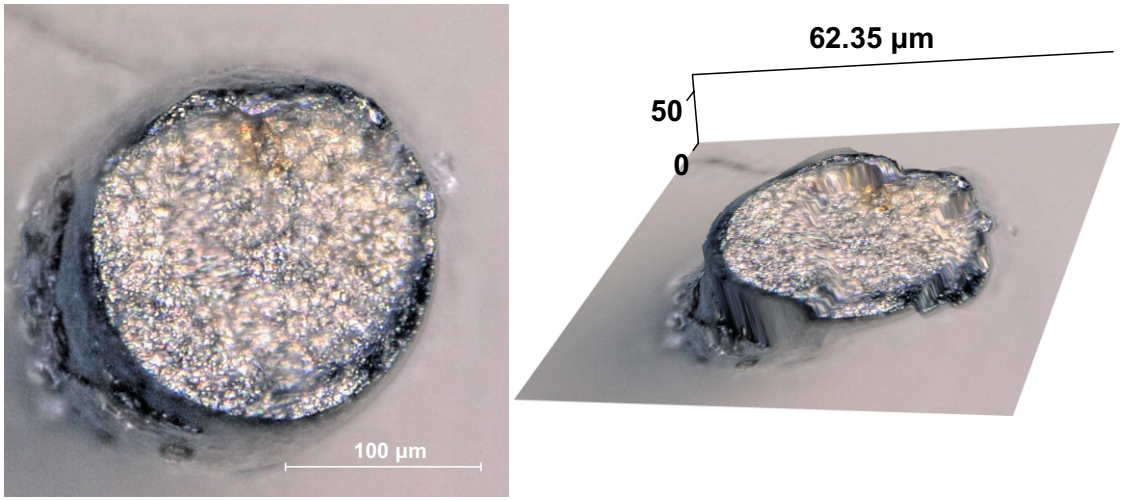

Figure A.2: Fracture surface of NiTi wire cycled in pure martensitic phase; $T = 37°\mathrm{C}$; $\sigma_{max} = 1370\,\mathrm{MPa}$

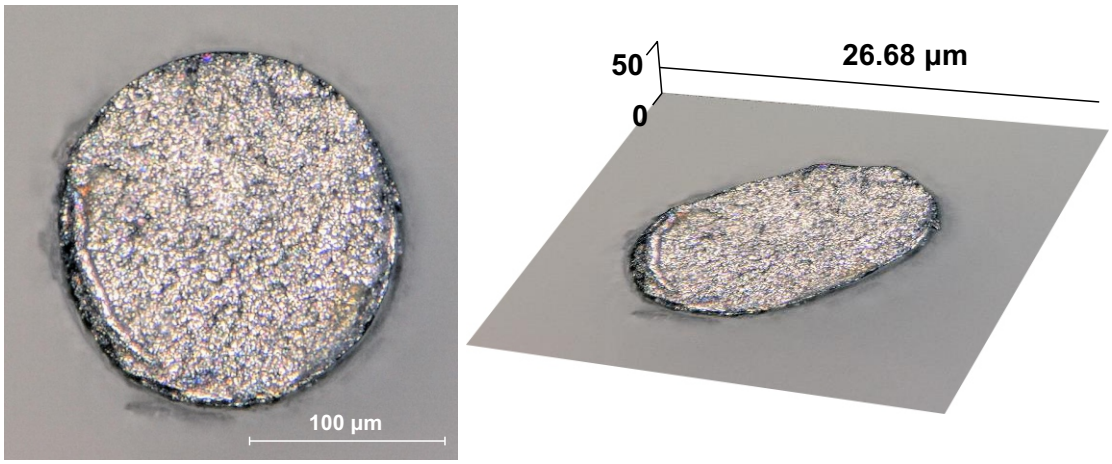

Figure A.3: Fracture surface of NiTi wire cycled in pseudoelastic regime; $T = 37°\mathrm{C}$; $\sigma_{max} = 700\,\mathrm{MPa}$

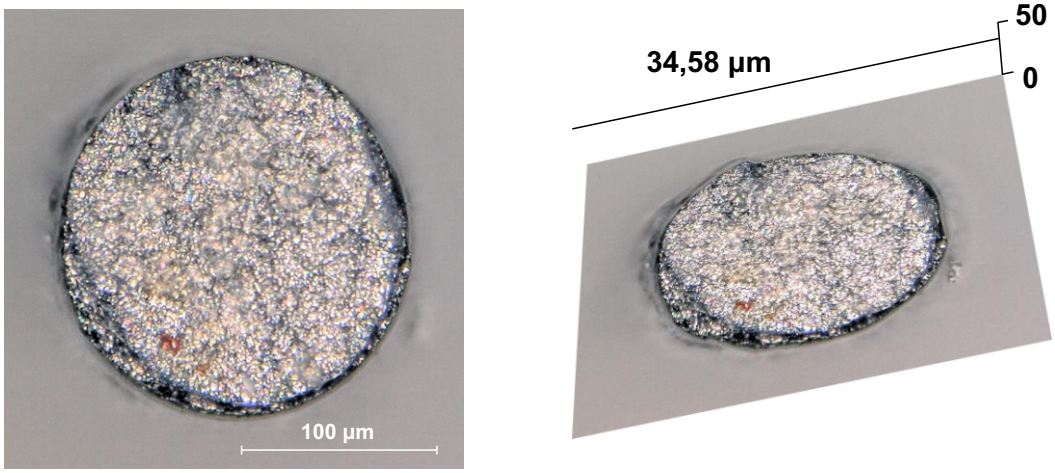

Figure A.4: Fracture surface of NiTi wire cycled in pseudoelastic regime; $T = 37°\mathrm{C}$; $\sigma_{max} = 630\,\mathrm{MPa}$

Appendix B

Fatigue tests data

Table B.1: Fatigue tests data for annealed NiTi wire specimens; $T = 20°C$; $R = 0.2$

Test nr.	Frequency f [Hz]	Maximal Force F_{max} [N]	Minimal Force F_{min} [N]	Maximal Stress σ_{max} [MPa]	Cycles until failure N [cycles]	Area of rupture
1	5	35	7	1380	1,162	in the middle
2					1,281	in the middle
3					1,369	lower jaw
4					1,520	in the middle
5					1,435	lower jaw
6					1,535	upper jaw
1	5	25	5	980	3,430	in the middle
2					3,071	in the middle
3					3,930	in the middle
4					2,576	upper jaw
5					3,802	in the middle
1	5	18	3.6	710	6,326	lower jaw
2					5,750	in the middle
3					6,346	in the middle
4					8,369	in the middle
5					8,296	in the middle
1	5	15	3	590	14,549	in the middle
2					2,515	in the middle
3					2,251	in the middle
4					2,781	upper jaw

Table B.1 – Continued from previous page

Test nr.	Frequency f [Hz]	Maximal Force F_{max} [N]	Minimal Force F_{min} [N]	Maximal Stress σ_{max} [MPa]	Cycles until failure N [cycles]	Area of rupture
1	5	14	2.8	550	3,976	upper jaw
2					4,053	upper jaw
3					4,720	lower jaw
1	5	13	2.6	510	8,432	lower jaw
2					5,536	upper jaw
3					4,679	lower jaw
4					4,397	upper jaw
5					3,216	lower jaw
1	5	12	2.4	470	6,940	lower jaw
2					15,043	upper jaw
3					13,809	lower jaw
1	5	11.5	2.3	450	10,000,000	runout
2					10,000,000	runout
3					10,000,000	runout
1	5	11	2.2	430	10,000,000	runout
2					10,000,000	runout
3					10,000,000	runout

Table B.2: Fatigue tests data for annealed NiTi wire specimens; $T = 37°C$; $R = 0.2$

Test nr.	Frequency f [Hz]	Maximal Force F_{max} [N]	Minimal Force F_{min} [N]	Maximal Stress σ_{max} [MPa]	Cycles until failure N [cycles]	Area of rupture
1	1	35	7	1380	1,765	upper jaw
2	3				1,800	upper jaw
3	3				1,466	in the middle
4	5				1,872	in the middle
1	5	25	5	980	3,814	in the middle
2					3,181	in the middle
3					2,386	in the middle
4					2,677	lower jaw
1	5	21	4.2	830	8,633	in the middle
2					7,118	in the middle
3					4,580	upper jaw
4					6,023	in the middle
1	5	18	3.6	710	2,152	lower jaw
2					1,980	lower jaw
3					2,562	lower jaw
4					3,332	upper jaw

Table B.2 – Continued from previous page

Test nr.	Frequency f [Hz]	Maximal Force F_{max} [N]	Minimal Force F_{min} [N]	Maximal Stress σ_{max} [MPa]	Cycles until failure N [cycles]	Area of rupture
1	5	17	3.4	670	3,915	in the middle
2					2,958	lower jaw
3					4,661	in the middle
4					3,629	in the middle
1	5	16	3.2	630	4,422	upper jaw
2					3,459	lower jaw
3					4,389	upper jaw
4					3,721	lower jaw
1	5	15	3	590	4,909	lower jaw
2					4,051	upper jaw
3					2,906	upper jaw
4					4,781	in the middle
1	5	14	2.8	550	10,000,000	runout
2	20				10,000,000	runout
3	20				10,000,000	runout

Appendix C

Results of tensile tests

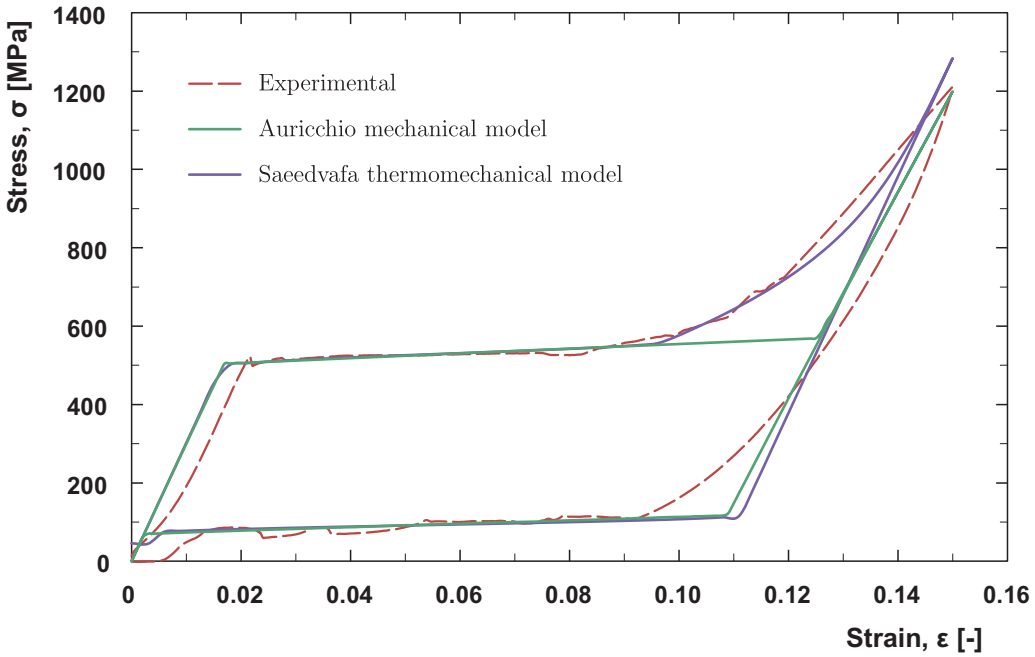

Figure C.1: Experimental and numerical tensile test data; $T = 20°C$

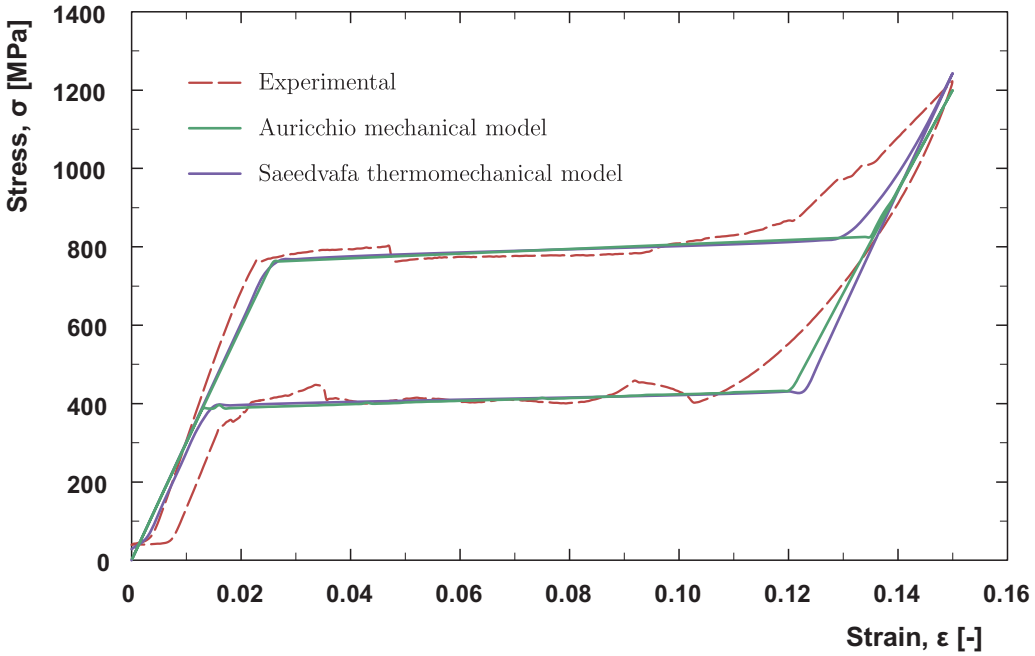

Figure C.2: Experimental and numerical tensile test data; $T = 60°C$

Appendix D

Program for derivation of cam profile

```
> restart;
```

```
> time_p:=Vector([0,0.055,0.076,0.18,0.2,0.25,0.315,0.34,0.36,0.5,0.7,0.849,
  0.85]): # aortic pressure data
  pressure:=Vector([75,90,99,118,119.5,120,111.4,112,110,94,80,75,75]):
```

```
> spline_pulse:=t->CurveFitting[Spline] (time_p,pressure,t,degree=3,endpoints=
  periodic): # fitting the data with use of cubic spline
```

```
> plots[display](plot(spline_pulse(t),t=0..0.86),plots[pointplot]([time_p,
  pressure]),gridlines=true,title=`blood pressure in aorta`,labels=[`t[s]`,`p
  [mmHg]`]);
```

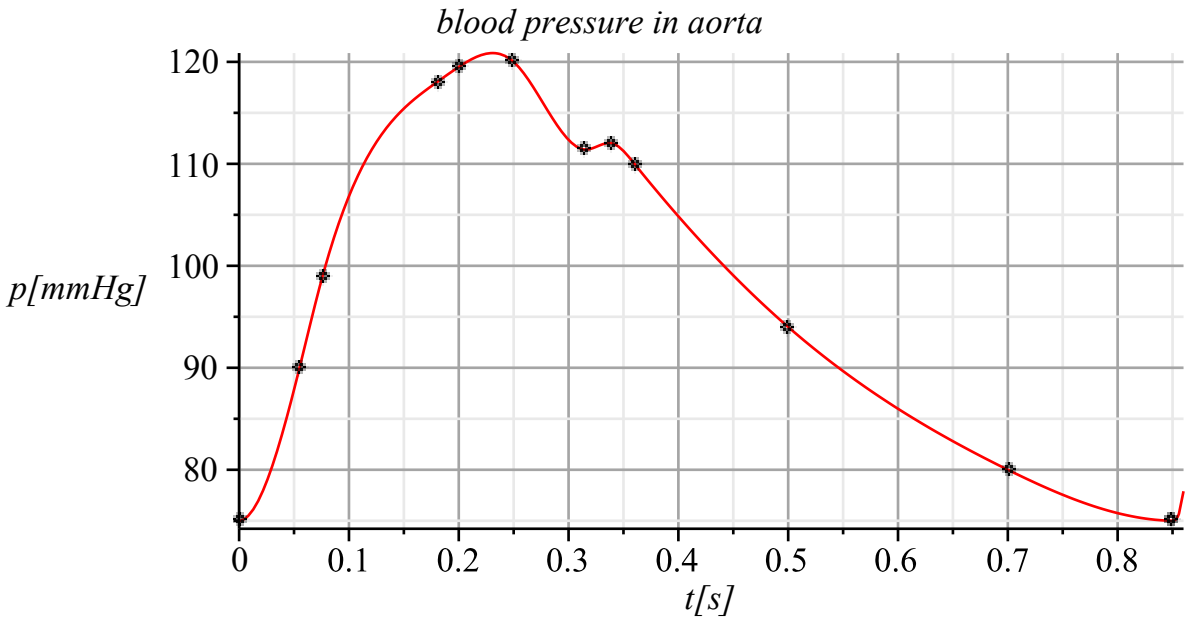


```
> b:=120: #[mm] distance between center of follower rotation and cam's touching point
```

```
> p_max:=maximize(spline_pulse(t),t=0..0.85);
  p_min:=minimize(spline_pulse(t),t=0..0.85);
```

$$p\_max := 120.8621449$$

$$p\_min := 74.999096 \quad \textbf{(1)}$$

```
> travel:=evalf((8*4454)/(Pi/3*(150^2/4+150*85/4+85^2/4))); #[mm] desired travel of the
  center of membrane according to volume change in form of the conical frustum
```

$$travel := 3.204337006 \quad \textbf{(2)}$$

```
> y:=unapply((spline_pulse(t)-p_min)/((p_max-p_min)*1e3)*travel,t): #[mm] function
  which describes linear motion of center of the membrane
```

```
> dy:=unapply(diff(y(t),t,t),t):
```

```
> k:=10:
  pole_y:=Array([
  [plot(y(t*k),t=0..0.85/k,gridlines=true,title=`membrane travel`,labels=[`t
  [s]`,`y[m]`])],
  [plot(diff(y(t*k),t),t=0..0.85/k,gridlines=true,title=`membrane velocity`,
  labels=[`t[s]`,`v_y[m.s-1]`])],
  [plot(diff(y(t*k),t,t),t=0..0.85/k,gridlines=true,title=`membrane
  acceleration`,labels=[`t[s]`,`a_y[m.s-2]`])]]):
  plots[display](pole_y,aligncolumns=[1],gridlines=true);
```

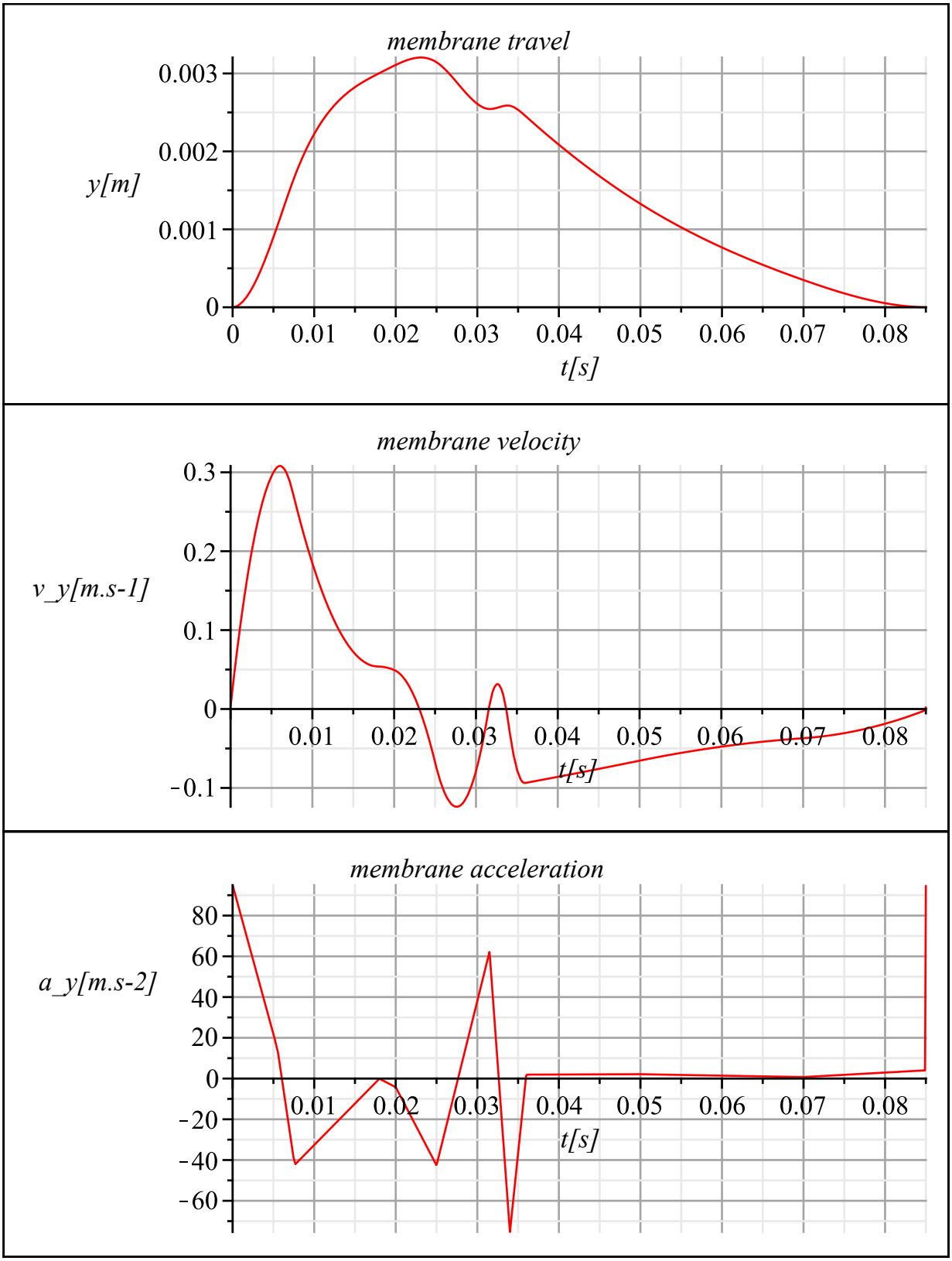


```
> v:=unapply(arctan(1000*y(t)/b),t): #[rad] function which describes follower angle

> pole_v:=Array([[plot(v(t*10),t=0..0.085,gridlines=true,title=`follower
angle`,labels=[`t[s]`,`v[rad]`])],
[plot(diff(v(t*10),t),t=0..0.085,gridlines=true,title=`angular velocity`,
labels=[`t[s]`,`omega_v[s-1]`])],
[plot(diff(v(t*10),t,t),t=0..0.085,gridlines=true,title=`angular
acceleration`,labels=[`t[s]`,`alpha_v[s-2]`])]]): plots[display](pole_v,
aligncolumns=[1]);
```

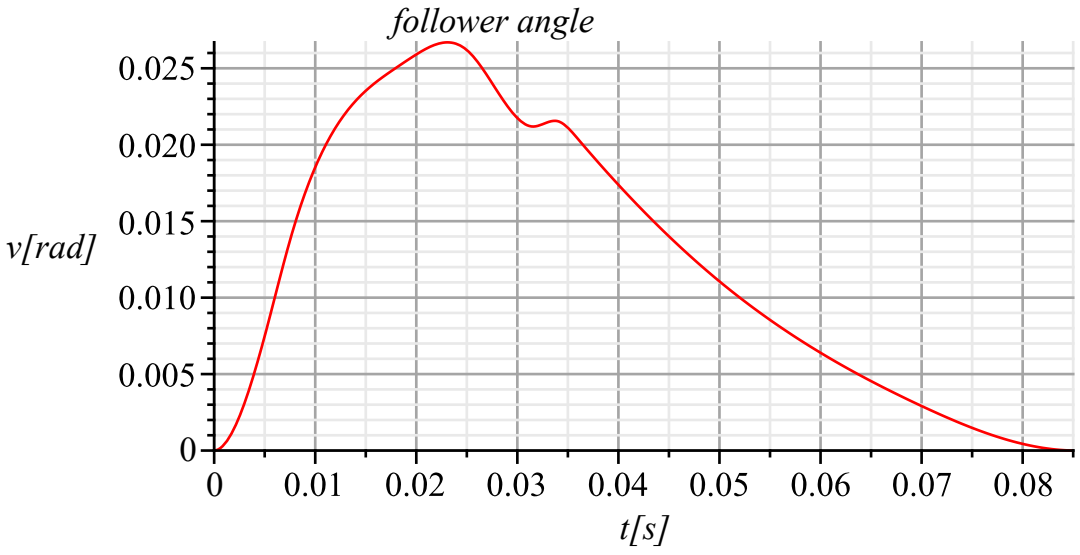

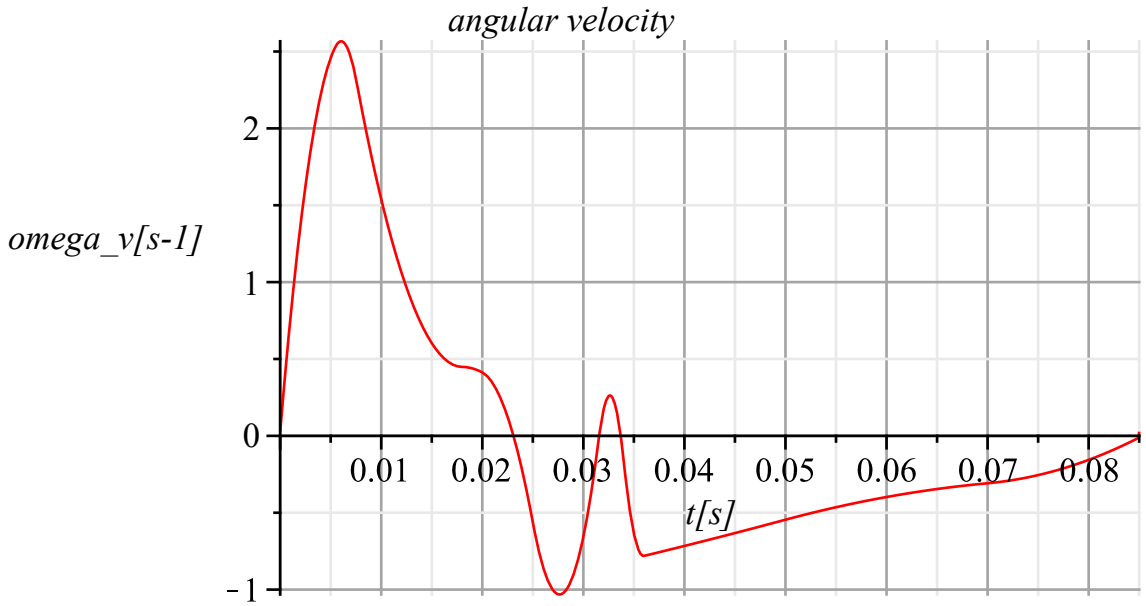

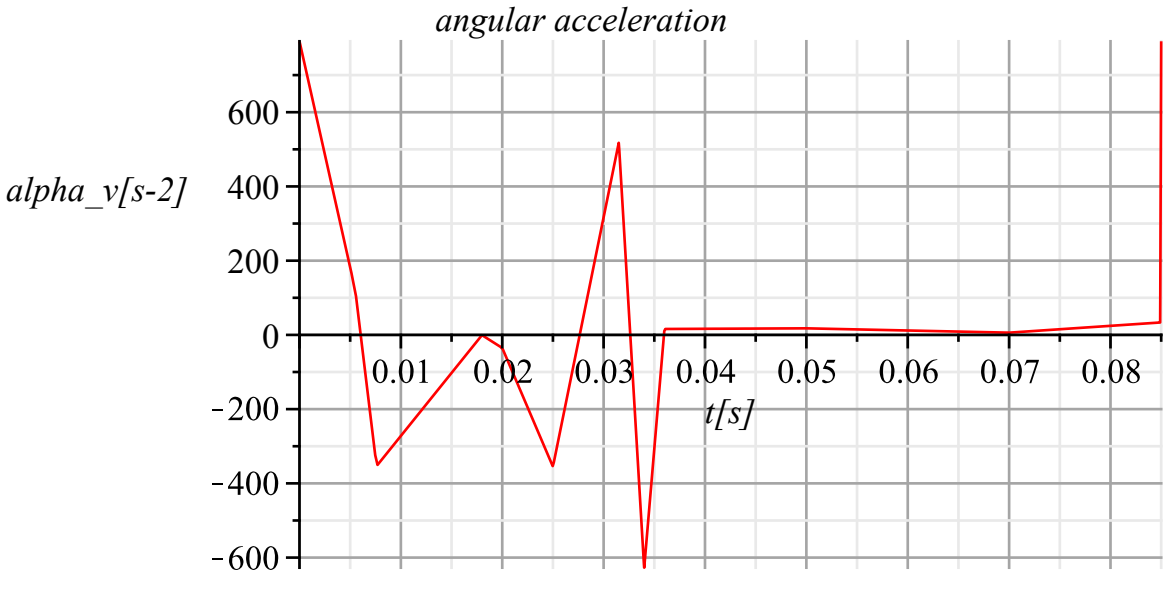


```
> save v,y, "follower_angle.txt"; #export of the data
```

```
> restart;

> read "follower_angle.txt":

> vv:=unapply(v(t),t):

> d0:=40: # [mm] base diameter of the cam
  l_v:=200: # [mm] follower length

> a:=sqrt(d0^2/4+l_v^2): # [mm] distance between cam's and follower's center of rototaion

> alpha:=arctan(d0/(2*l_v)): # initial angle of the follower

> v:=unapply(vv(t)+alpha):

> psi:=t->omega*t: # angular speed of the cam

> S:=1: omega:=2*Pi*1/0.85: # evaluation of cam's profile
> q:=S*(diff(psi(t),t)*a*cos(v(t)))/(diff(psi(t),t)-diff(v(t),t)):
> u:=sqrt(a^2 + q^2 - S*2*a*q*cos(v(t))):
> phi:=psi(t) + S * arccos((a - S*q*cos(v(t)))/u):
> rho:=S*a/(diff(psi(t),t)-diff(v(t),t))^3 * (diff(psi(t),t)*(diff(psi(t),t)-
  diff(v(t),t))*(diff(psi(t),t)-2*diff(v(t),t))*sin(v(t))+(diff(psi(t),t)*diff
  (v(t),t,t)-diff(psi(t),t,t)*diff(v(t),t))*cos(v(t))):

> plot([[u,phi,t=0..0.85],[d0/2/0.85*t,Pi/2-alpha,t=0..0.85]],color=[red,
  blue], axiscoordinates = polar, coords = polar,numpoints=2000); #,
  axiscoordinates = polar
```

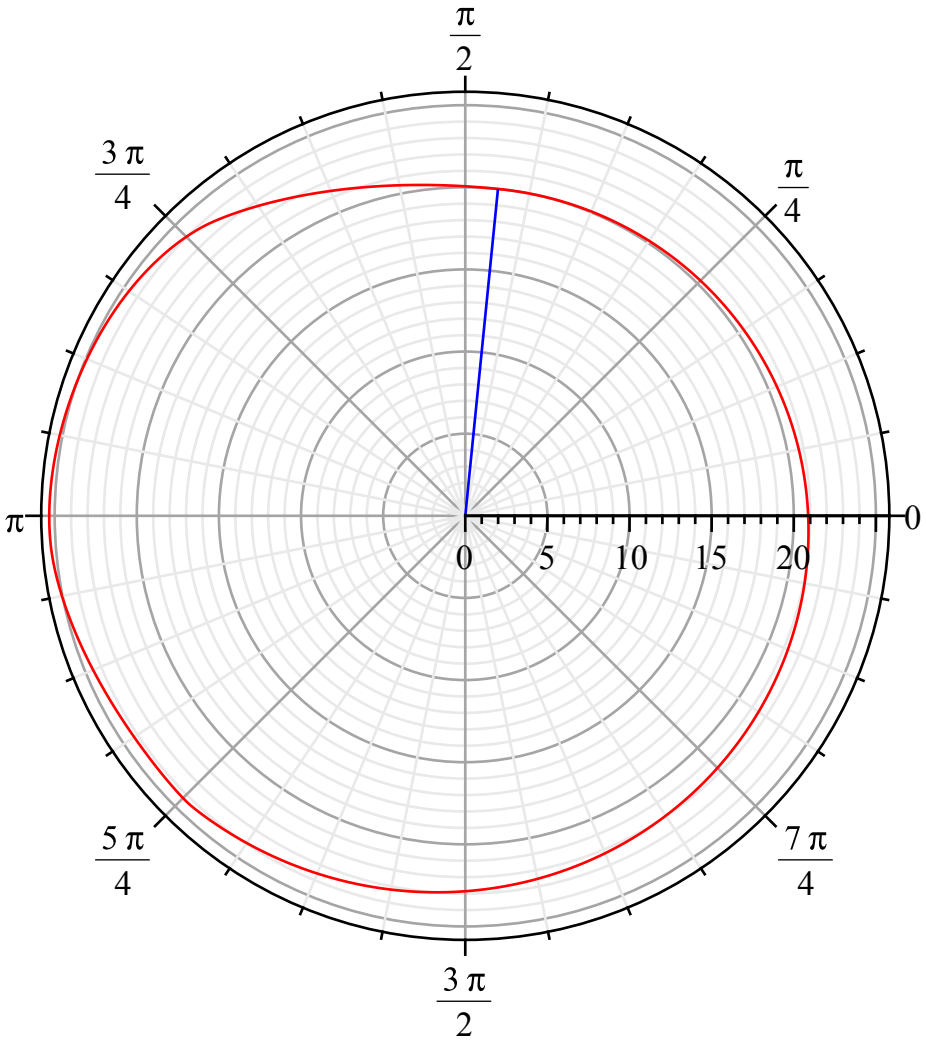

```
> plot([phi,rho,t=0..0.85],title=`radius of curvature`,labels=[`phi[rad]`,`rho
  [mm]`]);
```

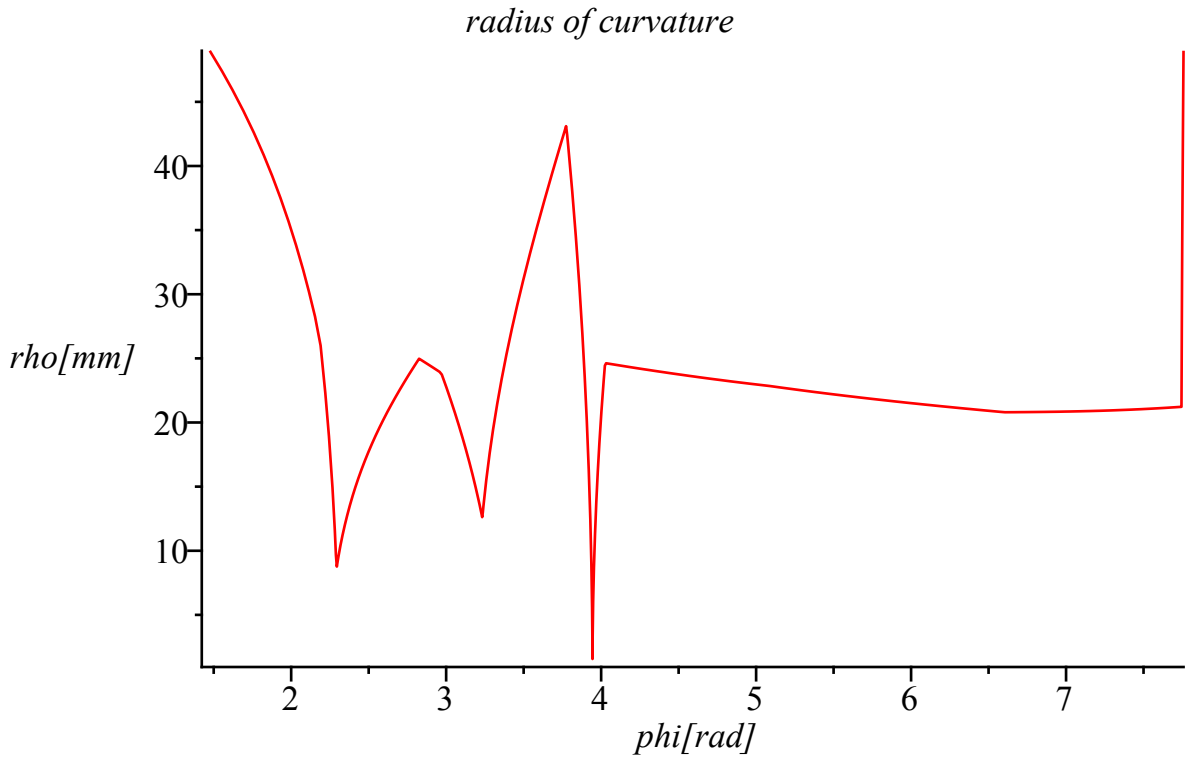


```
> nu:=-arctan(diff(v(t),t)/((diff(psi(t),t)-diff(v(t),t))*tan(v(t)))):
```

```
> kd:=0.5: # angle increment in degrees
  souradnice_polar:=Matrix(round(360*1/kd)+1,2):
  souradnice_kart:=Matrix(round(360*1/kd)+1,2):
```

```
> dt:=0.85/round(360*1/kd):
```

```
> for i from 1 to round(360*1/kd)+1 do # transfer of the cam's profile from polar to
  cartesian coordinate system
   tt:=(i-1)*dt:
   souradnice_polar[i,1]:=evalf(subs(t=tt,phi))/Pi*180:
   souradnice_polar[i,2]:=evalf(subs(t=tt,u)):
   souradnice_kart[i,1]:=souradnice_polar[i,2]*cos(souradnice_polar[i,1]*
  Pi/180):
   souradnice_kart[i,2]:=souradnice_polar[i,2]*sin(souradnice_polar[i,1]*
  Pi/180):
   if (i mod 100)=0 then
    print(i/100):
   end if:
  end do:
```

```
> ExcelTools[Export](souradnice_kart,"souradnice.xls"); # export of the profile
  coordinates data for further use
```

Appendix E

Clamps for cyclic testing of fine wires

Documentation

Appendix F

Stent-graft durability testing device

Documentation